united nations
educational, scientific
and cultural
organization

international atomic
energy agency

the
abdus salam
international centre for theoretical physics

School on "Exploring the Atmosphere by
Remote Sensing Techniques"
18 October - 5 November 1999

1151-12

"Ground-Based Remote Sensing of Cloud Properties Using Millimeter-Wave Radar"

E. Clothiaux
Pennsylvania State University
University Park
USA

Ground-Based Remote Sensing of Cloud Properties Using Millimeter-Wave Radar

EUGENE E. CLOTHIAUX
Research Associate in Meteorology
The Pennsylvania State University

THOMAS P. ACKERMAN
Professor of Meteorology
The Pennsylvania State University

ROGER T. MARCHAND
Research Associate in Meteorology
The Pennsylvania State University

JOHANNES VERLINDE
Assistant Professor of Meteorology
The Pennsylvania State University

DAVID M. BABB
Research Associate in Meteorology
The Pennsylvania State University

CHRISTOPHER S. RUF
Associate Professor of Electrical Engineering
The Pennsylvania State University

Acknowledgements

We are indebted to many colleagues for their help as we have delved into radar signal processing and interpretation. We are especially indebted to Bruce Albrecht, whose efforts were instrumental in the development of a millimeter-wave cloud radar here in the Department of Meteorology at the Pennsylvania State University. Robert Peters engineered the radar system, with supporting help from J. Thomas Treaster, and he has patiently answered all of our questions about its operation. Gerald Mace has worked unceasingly to collect important data sets with the radar and, as we begin to apply cloud retrievals of the sort described in this document to these data sets, his contributions will become increasingly apparent. The core of this paper originated with a number of discussions with our colleague Hans Verlinde as he designed and taught a Radar Meteorology course for the first time here in the Department of Meteorology. The number of references to various scientists in the National Atmospheric and Oceanic Administration attests to their significant contributions to this field of research. This work would not have been possible without early support from the National Aeronautics and Space Administration (NAG-1-999) and sustained support from the Department of Energy Atmospheric Radiation Measurements Program (DE-FG02-90ER61071).

Contents

PART 1 - BASIC THEORY

Chapter 1
Introduction

The importance of clouds to the present climate of the Earth is unquestioned. As the Earth system undergoes change, both natural and human-induced, the physical properties of clouds can be expected to change. To understand the current role of clouds in the climate system, as well as possible roles in future climate systems, observation of the current cloud fields of the Earth and their evolution in time is necessary. Unfortunately, even some of the most basic features of clouds, such as their frequency of occurrence or geometrical thickness, are difficult to determine. Recent satellite observational studies, such as the International Satellite Cloud Climatology Project, are leading to a significant improvement in understanding the horizontal distribution of clouds; however, these kinds of satellite analyses are only beginning to address the issue of the vertical distribution of the observed cloud fields. With the technologies currently available, the most useful instruments for studying the vertical distribution of clouds are active remote sensors, such as radar and lidar. Radar is the only device that can map out the vertical distribution of most clouds under all weather conditions, whereas lidar is sensitive to tenuous upper level clouds in otherwise clear sky conditions. In this article we will discuss the role of radar in the remote sensing of clouds and their properties.

Radar remote sensing of cloud properties can be viewed as a two step process. First, the actual power levels that are eventually recorded in one form or another within the radar unit must be interpreted; that is, they must be related to physical quantities that are of interest and use in inferring the properties of clouds. Second, the methods by which the radar-derived quantities are used to infer actual cloud properties must be developed. The first step is, in many ways, a solved problem. There are standard, accurate signal processing techniques for calculating the reflectivity, mean Doppler velocity and mean Doppler width from the receiver signal voltages that result when a meteorological target scatters transmitted electromagnetic radiation back to the radar receiver. The second step is by no means a solved problem and much current research is being devoted to the development of cloud property retrieval algorithms using radar-derived quantities as input. The discussion that follows is organized around these two

steps. We first discuss the issues of radar signal processing and then we describe the results of some of the research that attempts to infer various cloud properties using the radar-derived quantities as inputs.

Fortunately, the signal processing techniques applied to cloud-sensing millimeter-wave radars are identical to the techniques developed since the late 1940s for the radar remote sensing of rain and other interesting weather conditions (Atlas, 1990). There are several published books that describe to various levels of detail the methods of radar-signal processing when observing meteorological targets. As an introduction to radar-remote sensing, Battan (1973) and Sauvageot (1992) are good starting points. Doviak and Zrnic (1984, 1993) and Ulaby et al. (1982) provide a much more thorough description about each aspect of a radar and its use in observing meteorological targets; however, the increased levels of rigor make the discussions more difficult to understand without a prior knowledge of the subject. The work of Doviak and Zrnic (1993) is especially relevant to the information that we are presenting here. Therefore, we have adopted the approach of trying to tie our discussion as closely as possible to their work, while attempting to provide enough discussion and figures to clarify issues that we initially found difficult to understand.

Retrieval of cloud properties using radar and related observations is a relatively new subject. Our treatment here summarizes several recently published methods by outlining the basic physics and essential mathematical relationships of each. Because this field is still in its infancy, the methods have not been extensively compared or verified. Thus we are unable to present an evaluation of the relative accuracy of the methods.

Chapter 2
The Radar Signal

To keep the following discussion of radar-signal processing steps as concrete as possible, we will describe each step in the context of the 94-GHz cloud radar developed at the Pennsylvania State University (Figure 1 and 2). Our examples are largely drawn from this system because we are intimately familiar with its operation (Clothiaux et al, 1995). As Figure 2 illustrates, there are essentially two distinct components to the radar hardware: the transmitter and the receiver. Therefore, our discussion is divided into two parts. First, we describe the transmission of the electromagnetic wave from the extended interactive oscillator out to the meteorological target and finally back to the receiver antenna. Since most descriptions of radar remote sensing are couched in terms of power densities, we then describe this same transmission process using power densities as the physical quantity of interest. The second part of the discussion follows the return signal from the output port of the receiver antenna through the receiver chain. We describe the

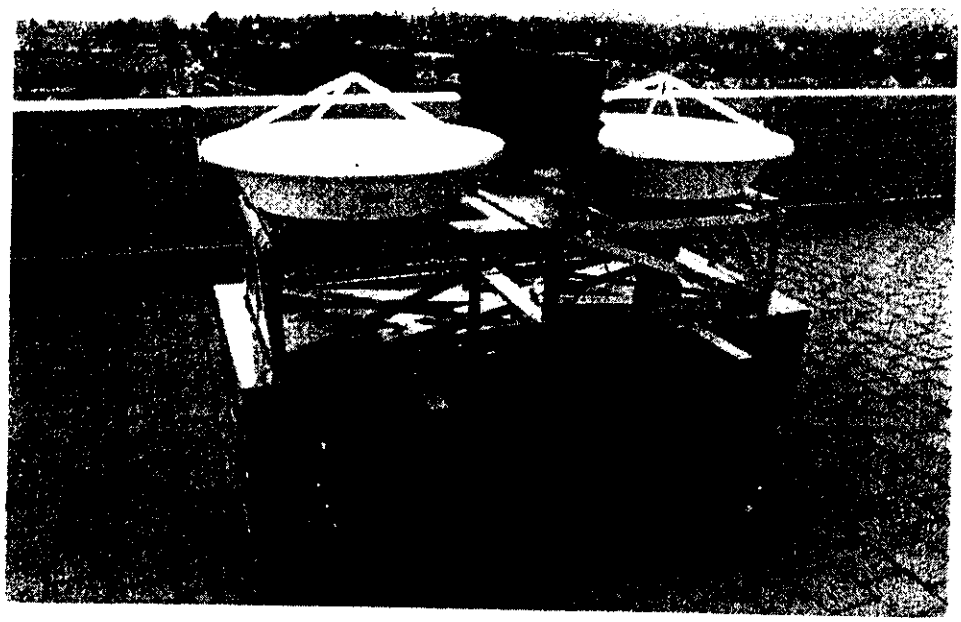

Figure 1. The Pennsylvania State University 94-GHz cloud radar.

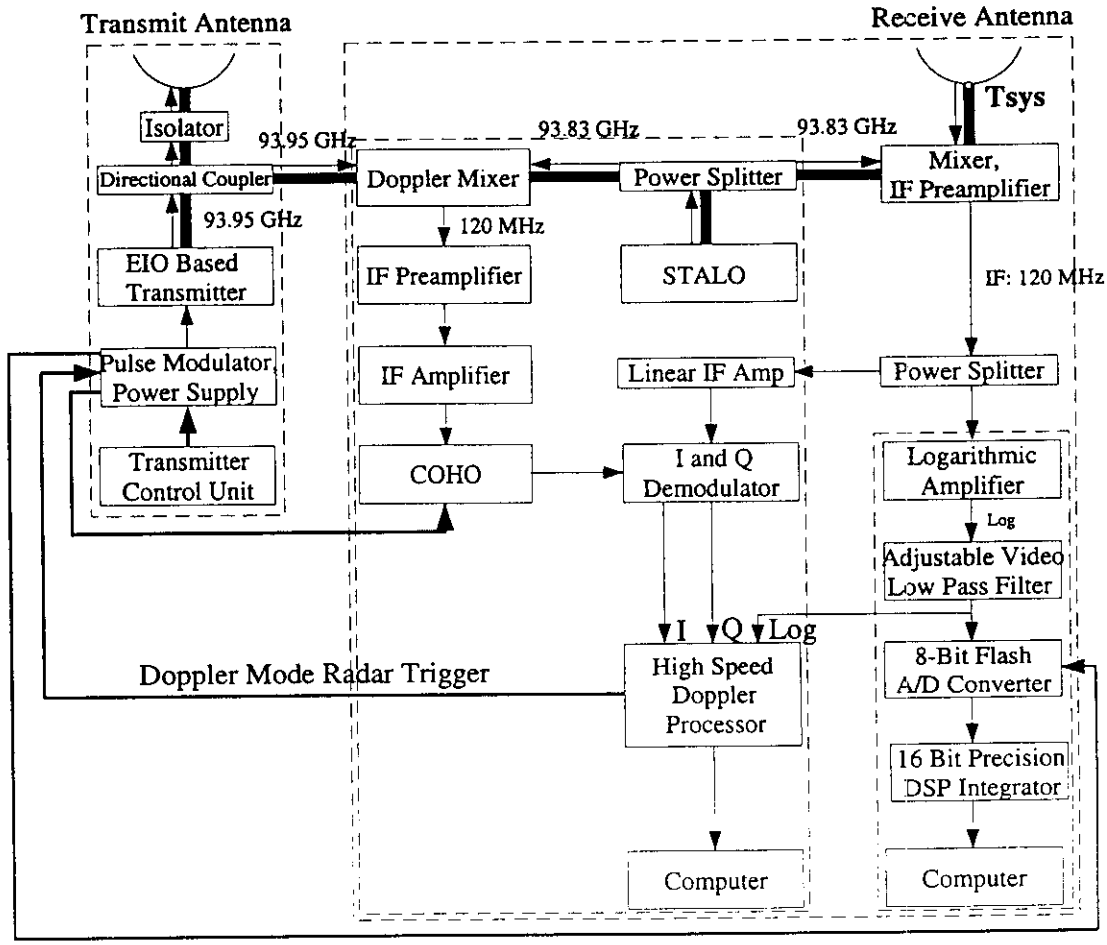

Figure 2. Block diagram of the radar hardware. The two outer dashed blocks enclose the transmitter and receiver components of the radar. Within the receiver box, there are two more dashed blocks: one encloses the incoherent path processing hardware and the other the coherent, or Doppler, processing hardware.

effects of the meteorological target motions on the return signal in terms of the voltages that eventually emerge from the I and Q demodulators (Figure 2). Before launching into a description of the transmission process we first mention one property of complex numbers that we use in our discussion of electromagnetic fields. Let

$$\mathcal{A} = A_o e^{i\phi} \tag{2.1}$$

represent an arbitrary complex number. The operator $\mathcal{R}$ means take the real part of $\mathcal{A}$; that is,

$$A_{\text{part}}^{\text{real}} = \mathcal{R}(\mathcal{A}) = \mathcal{R}(A_o e^{i\phi}) = \mathcal{R}(A_o \cos\phi + iA_o \sin\phi) = A_o \cos\phi. \tag{2.2}$$

Even though electromagnetic waves are physical entities, they are often efficiently represented by complex value expressions during mathematical manipulation (Bohren and Huffman, 1983, Section 2.2; hereafter BH, 2.2). For example, the plane, monochromatic electric field

$$\vec{E}(r,t) = E_o \cos(kr - \omega t)\hat{e} \tag{2.3}$$

can be represented by

$$\vec{\mathcal{E}}(r,t) = E_o e^{i(kr-\omega t)}\hat{e} \tag{2.4}$$

with the understanding that the true field is described by the real part of $\vec{\mathcal{E}}$.

2.1 Electromagnetic Field Description of the Transmitted Signal

2.1.1 Electromagnetic Field in the Transmitter Waveguide

For pulsed radars such as the one illustrated in Figure 1, the primary function of the transmitter is to send up into the atmosphere a pulsed beam of electromagnetic radiation. To generate pulses of electromagnetic radiation at the carrier frequency (93.95 GHz, or 3.19 mm, for the Pennsylvania State University radar), an extended interactive oscillator, or EIO, that generates electromagnetic radiation at the carrier frequency is gated by a pulse modulator. A sketch of the resultant, pulsed electromagnetic wave that travels from the oscillator out to the transmitter antenna is illustrated in Figure 3.

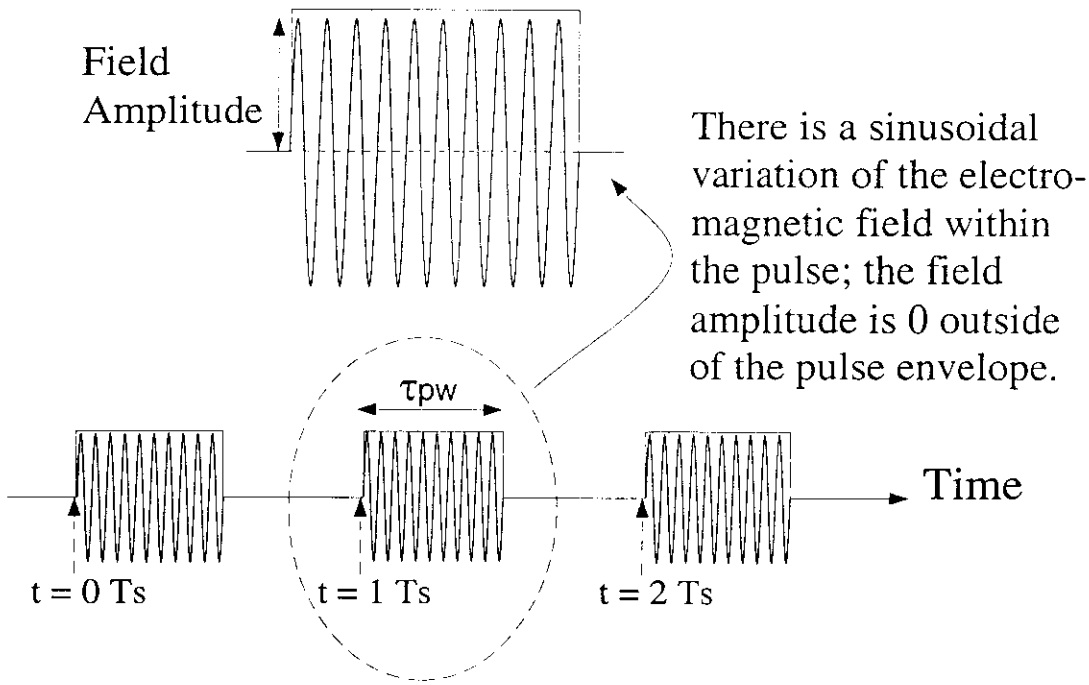

Figure 3. Cartoon illustration of the electromagnetic wave leaving the transmitter oscillator. The pulse modulator generates the rectangular waveform which allows the oscillator output to be pulsed.

The theory of propagating waves in rectangular shaped waveguides is well documented (e.g., Reitz et al., 1979); the result for the electric field components of a transverse wave propagating parallel to the interior space of the waveguide in the z direction is

$$\vec{E}_{\mathrm{x}}(x,y,z,t) = E_{\mathrm{ox}} \cos\left(\frac{m\pi x}{a}\right) \sin\left(\frac{n\pi y}{b}\right) \sin\left(\frac{2\pi z}{\lambda_g} - \omega t\right) \hat{e}_{\mathrm{x}}, \tag{2.5}$$

$$\vec{E}_{\mathrm{y}}(x,y,z,t) = E_{oy} \sin\left(\frac{m\pi x}{a}\right) \cos\left(\frac{n\pi y}{b}\right) \sin\left(\frac{2\pi z}{\lambda_g} - \omega t\right) \hat{e}_{\mathrm{y}} \tag{2.6}$$

and $\vec{E}_{\mathrm{z}}(x,y,z,t) = 0\,\hat{e}_{\mathrm{z}}$. The wavelength λ_{g} of the radiation within the waveguide and along the direction of propagation is given by

$$\left(\frac{2\pi}{\lambda_{\mathrm{g}}}\right)^2 = \left(\frac{2\pi}{\lambda_{\mathrm{c}}}\right)^2 - \left(\frac{m\pi}{a}\right)^2 - \left(\frac{n\pi}{b}\right)^2, \tag{2.7}$$

where a and b are waveguide dimensions, $\lambda_{\mathrm{c}} = 2\pi/\omega_{\mathrm{c}}$ and ω_{c} is the carrier frequency (Figure 4a). For the Pennsylvania State University radar, the waveguide dimensions are $a = 2.5\,\mathrm{mm}$ and $b = 1.3\,\mathrm{mm}$. Since $\lambda_{\mathrm{c}} = 3.19\,\mathrm{mm}$ and λ_{g} must be larger than zero for a physically meaningful solution, the only viable choices of m and n are one and zero, respectively. Therefore, $\vec{E}_{\mathrm{x}}(x,y,z,t) = 0\,\hat{e}_{\mathrm{x}}$ and $\vec{E}_{\mathrm{y}}(x,z,t)$ reduces to

$$\vec{E}_{\mathrm{y}}(x,z,t) = E_{\mathrm{oy}} \sin\left(\frac{\pi x}{a}\right) \sin\left(\frac{2\pi z}{\lambda_{\mathrm{g}}} - \omega t\right) \hat{e}_{\mathrm{y}}. \tag{2.8}$$

The electromagnetic wave within the waveguide is transverse, sinusoidal in time and polarized with the plane of polarization being defined by the direction of propagation of the wave and the direction of the electric field (Figure 4b).

2.1.2 Transmitted Electromagnetic Field Far from the Radar

After suffering losses in power on its journey to the transmitter antenna, the electromagnetic wave emerging from the waveguide is sent up into the atmosphere by the transmitter antenna (Figure 5). At a large distance r from the antenna with diameter D_{ant}, i.e., in the far field of the antenna ($4D_{\mathrm{ant}}^2/\lambda_{\mathrm{c}} >> 1$), the electromagnetic wave is polarized with both its electric and magnetic field components perpendicular to its direction of propagation, which is radially away from the radar. The electric field component of the wave is parallel to the plane of polarization illustrated in Figure 4b. The mathematical description of the electric field at a point far away from the antenna is (BH, 3.2)

$$\vec{E}_{\mathrm{i}}(r,\theta,\phi,t) = \frac{A_{\mathrm{i}}(\theta,\phi)}{r} \cos(k_{\mathrm{c}} r - \omega_{\mathrm{c}} t + \phi_{\mathrm{t}})\,\hat{e}_{\mathrm{i}}, \tag{2.9}$$

where ω_{c} is the carrier frequency, t is the time, r is the distance from the antenna, c is the speed of light and ϕ_{t} sets the initial phase of the transmitted wave. The amplitude

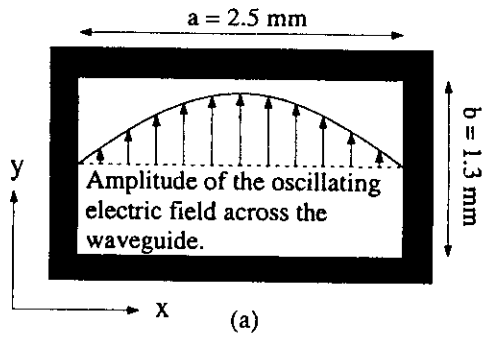

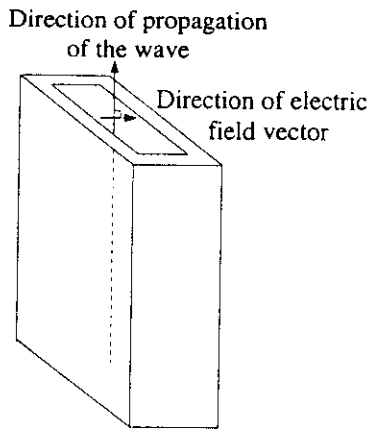

Figure 4. a.) Cross section of the waveguide connecting the oscillator to the transmitter antenna. The electromagnetic field that propagates through the waveguide is parallel to the y-axis. b.) The plane of polarization of the transmitted wave is defined by the direction of propagation of the wave and the direction of the electric field.

$A_{\rm i}(\theta,\phi)$ depends upon the power delivered to the transmitter antenna and the shape of the transmitter antenna (Figure 6). In complex language notation

$$\vec{\mathcal{E}}_{\rm i}(r,\theta,\phi,t) = \frac{A_{\rm i}(\theta,\phi)e^{i\phi_t}}{r} e^{i(k_{\rm c}r-\omega_{\rm c}t)}\,\hat{e}_{\rm i}. \tag{2.10}$$

2.1.3 Scattered Electromagnetic Field at the Receiver Antenna

Now suppose that at r the pulse encounters an object of some sort which we label as m. The electric field scattered by the object back to the radar is

$$\vec{\mathcal{E}}_{\rm rant,m}(r_{\rm m},\theta_{\rm m},\phi_{\rm m},t) = \frac{S_{2,\rm m}(180°)e^{-i(\omega_{\rm d,m}t-\phi_{\rm s,m})}}{k_{\rm c}r_{\rm m}} e^{ik_{\rm c}r_{\rm m}} \frac{A_{\rm i}(\theta_{\rm m},\phi_{\rm m})e^{i\phi_t}}{r_{\rm m}} e^{i(k_{\rm c}r_{\rm m}-\omega_{\rm c}t)}\hat{e}_{\rm i}$$
$$+\frac{S_{4,\rm m}(180°)e^{-i(\omega_{\rm d,m}t-\phi_{\rm s,m})}}{k_{\rm c}r_{\rm m}} e^{ik_{\rm c}r_{\rm m}} \frac{A_{\rm i}(\theta_{\rm m},\phi_{\rm m})e^{i\phi_t}}{r_{\rm m}} e^{i(k_{\rm c}r_{\rm m}-\omega_{\rm c}t)}\hat{e}_{\rm cross}, \tag{2.11}$$

where $S_{2,\rm m}(180°)$ and $S_{4,\rm m}(180°)$ are the real magnitudes of the complex amplitude scattering matrix elements (BH, 3.2)

$$S_{2,\rm m} = S_{2,\rm m}(180°)e^{-i(\omega_{\rm d,m}t-\phi_{\rm s,m})} \tag{2.12}$$

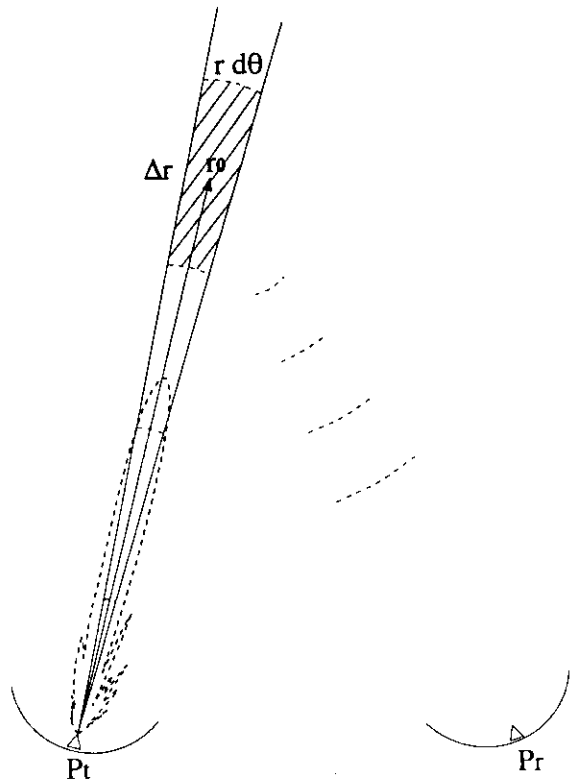

Figure 5. Cartoon illustration of the propagation of the electromagnetic field from the transmitter antenna, to the atmosphere and then back to the receiver antenna.

and

$$S_{4,\mathrm{m}} = S_{4,\mathrm{m}}(180°)e^{-i(\omega_{\mathrm{d,m}}t-\phi_{\mathrm{s,m}})}. \tag{2.13}$$

The phases associated with these two matrix elements have two parts: one part $\phi_{\mathrm{s,m}}$ that represents phase changes upon scattering and a second part $\omega_{\mathrm{d,m}}t$ due to the motion of the particle toward or away from the radar. Although the magnitude of the cross polarization matrix element $S_{4,\mathrm{m}}(180°)$ is generally small, it may contain useful information about the properties of the scatterer. (Note that the Pennsylvania State University radar is insensitive to the cross polarization electric field component in its present configuration because this component of the field does not propagate through the circular-to-rectangular waveguide hardware that connects the receiver antenna to the mixer and preamplifier assembly.) Because of the generally small amplitude of $S_{4,\mathrm{m}}(180°)$ and the fact that polarization studies are beyond the scope of this article, we neglect the cross polarization component at this point and write the scattered electric field at the radar receiver antenna as

$$\vec{\mathcal{E}}_{\mathrm{rant,m}}(r_{\mathrm{m}},\theta_{\mathrm{m}},\phi_{\mathrm{m}},t) = \frac{S_{2,\mathrm{m}}(180°)e^{-i(\omega_{\mathrm{d,m}}t-\phi_{\mathrm{s,m}})}}{k_{\mathrm{c}}r_{\mathrm{m}}}e^{ik_{\mathrm{c}}r_{\mathrm{m}}}\frac{A_{\mathrm{i}}(\theta_{\mathrm{m}},\phi_{\mathrm{m}})e^{i\phi_{\mathrm{t}}}}{r_{\mathrm{m}}}e^{i(k_{\mathrm{c}}r_{\mathrm{m}}-\omega_{\mathrm{c}}t)}\,\hat{e}_{\mathrm{i}}. \tag{2.14}$$

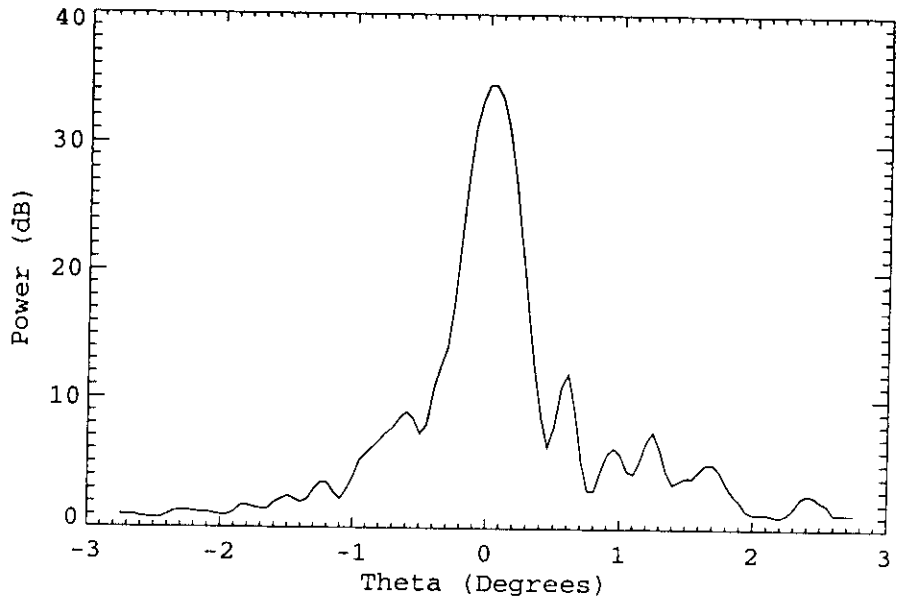

Figure 6. Beam pattern of the Pennsylvania State University 94-GHz cloud radar transmitter antenna.

The scattered electric field is now linearly polarized and we drop the vector notation to emphasize that there is only one remaining component. Rearranging (2.14) leads to

$$\mathcal{E}_{\mathrm{rant,m}}(r_{\mathrm{m}},\theta_{\mathrm{m}},\phi_{\mathrm{m}},t) = A_{\mathrm{r,m}}(r_{\mathrm{m}},\theta_{\mathrm{m}},\phi_{\mathrm{m}})e^{i[2k_{\mathrm{c}}r_{\mathrm{m}}-(\omega_{\mathrm{c}}+\omega_{\mathrm{d,m}})t+\phi_{\mathrm{s,m}}+\phi_{\mathrm{t}}]}, \tag{2.15}$$

where

$$A_{\mathrm{r,m}}(r_{\mathrm{m}},\theta_{\mathrm{m}},\phi_{\mathrm{m}}) = \frac{S_{2,\mathrm{m}}(180^{\circ})A_{\mathrm{i}}(\theta_{\mathrm{m}},\phi_{\mathrm{m}})}{k_{\mathrm{c}}r_{\mathrm{m}}^{2}}. \tag{2.16}$$

At this point we assume that both the transmitter phase ϕ_{t} and the phase shift $\phi_{\mathrm{s,m}}$ upon scattering are constants, even though $\phi_{\mathrm{s,m}}$ may be a function of time for such meteorological targets as vibrating water drops or tumbling ice particles (Doviak and Zrnic, 1993, Section 3.4.3; hereafter DZ, 3.4.3). The term $\omega_{\mathrm{d,m}}t$ represents the shift in phase of the scattered wave in the direction of the radar due to the relative radial velocity of the target with respect to the radar and $2k_{\mathrm{c}}r_{\mathrm{m}} = 2\pi(2r/\lambda_{\mathrm{c}})$ is the number of wavelengths along the round trip path between the radar and the target in units of radians.

2.1.4 From Fields to Power Densities

In the radar literature the electromagnetic wave propagating through the atmosphere is usually described in terms of the time-averaged power density over one cycle of the carrier wave. The instantaneous power density of the field incident on the scatterer is

$$P_{\mathrm{i}}(r_{\mathrm{m}},\theta_{\mathrm{m}},\phi_{\mathrm{m}},t) \propto E_{\mathrm{i}}^2(r_{\mathrm{m}},\theta_{\mathrm{m}},\phi_{\mathrm{m}},t). \tag{2.17}$$

The proportionality factor η_{o} takes into account the electric and magnetic nature of the radiation:

$$P_{\mathrm{i}}(r_{\mathrm{m}},\theta_{\mathrm{m}},\phi_{\mathrm{m}},t) = \frac{1}{\eta_{\mathrm{o}}} E_{\mathrm{i}}^2(r_{\mathrm{m}},\theta_{\mathrm{m}},\phi_{\mathrm{m}},t). \tag{2.18}$$

Averaging $P_{\mathrm{i}}(r_{\mathrm{m}},\theta_{\mathrm{m}},\phi_{\mathrm{m}},t)$ over one cycle of the wave yields

$$P_{\mathrm{i}}(r_{\mathrm{m}},\theta_{\mathrm{m}},\phi_{\mathrm{m}}) = \frac{1}{\eta_{\mathrm{o}}}\left(\frac{A_{\mathrm{i}}(\theta_{\mathrm{m}},\phi_{\mathrm{m}})}{r_{\mathrm{m}}}\right)^2 \left[\frac{1}{2\pi/\omega_{\mathrm{c}}}\int_0^{2\pi/\omega_{\mathrm{c}}} \cos^2(k_{\mathrm{c}} r_{\mathrm{m}} - \omega_{\mathrm{c}} t + \phi_{\mathrm{t}})dt\right]. \tag{2.19}$$

The factor in brackets equals 1/2 so that the power density at the scatterer becomes (DZ, 2.1)

$$P_{\mathrm{i}}(r_{\mathrm{m}},\theta_{\mathrm{m}},\phi_{\mathrm{m}}) = \frac{1}{2\eta_{\mathrm{o}}}\left(\frac{A_{\mathrm{i}}(\theta_{\mathrm{m}},\phi_{\mathrm{m}})}{r_{\mathrm{m}}}\right)^2. \tag{2.20}$$

In a similar fashion one can demonstrate that the average return power density at the receiver antenna is

$$P_{\mathrm{rant,m}}(r_{\mathrm{m}},\theta_{\mathrm{m}},\phi_{\mathrm{m}}) = \frac{[A_{\mathrm{r,m}}(r_{\mathrm{m}},\theta_{\mathrm{m}},\phi_{\mathrm{m}})]^2}{2\eta_{\mathrm{o}}} = \frac{1}{2\eta_{\mathrm{o}}}\left(\frac{S_{2,\mathrm{m}}(180°)}{k_{\mathrm{c}} r_{\mathrm{m}}}\right)^2 \left(\frac{A_{\mathrm{i}}(\theta_{\mathrm{m}},\phi_{\mathrm{m}})}{r_{\mathrm{m}}}\right)^2. \tag{2.21}$$

The backscatter cross section $\sigma_{\mathrm{b,m}}$ is defined by (BH, 4.6)

$$\sigma_{\mathrm{b,m}} = 4\pi\left(\frac{S_{2,\mathrm{m}}(180°)}{k_{\mathrm{c}}}\right)^2, \tag{2.22}$$

so that the power density at the receiver antenna becomes

$$P_{\mathrm{rant,m}}(r_{\mathrm{m}},\theta_{\mathrm{m}},\phi_{\mathrm{m}}) = \frac{1}{8\pi\eta_{\mathrm{o}}}\frac{\sigma_{\mathrm{b,m}}}{r_{\mathrm{m}}^2}\left(\frac{A_{\mathrm{i}}(\theta_{\mathrm{m}},\phi_{\mathrm{m}})}{r_{\mathrm{m}}}\right)^2. \tag{2.23}$$

We are now in a position to compare the electromagnetic field description of the transmission process with the more widely used description based on power densities.

2.2 Power Description of the Transmitted Signal

2.2.1 Scattering from a Single Isolated Particle

In terms of the properties of the radar, let P_t represent the average power density over a single cycle of the electromagnetic radiation that is delivered to the transmitter antenna input port. If the wave is stable over the duration of the pulse (i.e., the amplitude and frequency of the sinusoid in Figure 3 do not change over the pulse.), P_t also represents the average power over the entire pulse. If the antenna were to radiate isotropically, the power density a distance r away would be $P_t/4\pi r^2$; however, the transmitter antenna provides a gain G_t along the main beam axis with a falloff in power away from the axis given by the beam pattern $f_t^2(\theta,\phi)$. Therefore, the power density a distance r from the antenna in the direction (θ,ϕ) is (DZ, 3.1)

$$\left(\frac{P_t}{4\pi r^2}\right)\left(f_t^2(\theta,\phi)\right)\left(G_t\right). \tag{2.24}$$

As the beam travels a distance r, it is attenuated by atmospheric constituents, such as oxygen, water vapor and hydrometeors. Letting $k_e(r)$ represent the extinction coefficient of the atmosphere along the beam path (units of m^{-1}), the attenuation is (DZ, 3.3)

$$l_t^{-1} = e^{-\int_0^r k_e(r)dr}, \tag{2.25}$$

where, in keeping with Doviak and Zrnic (DZ, 3.3), we have written the loss as a quantity greater than one. Therefore, (2.24) becomes

$$P_i(r,\theta,\phi) = \left(\frac{P_t}{4\pi r^2}\right)\left(f_t^2(\theta,\phi)\right)\left(G_t\right)\left(l_t^{-1}\right). \tag{2.26}$$

Comparing (2.20) and (2.26), the electric field amplitude $A_i(\theta,\phi)$ in terms of the radar parameters is

$$A_i(\theta,\phi) = \sqrt{\frac{P_t G_t \eta_o}{2\pi l_t}} f_t(\theta,\phi). \tag{2.27}$$

Now suppose that at r the pulse encounters an object (labelled m) of some sort. The amount of energy scattered by the object in any direction is characterized by the scattering cross section $\sigma_m(\theta',\phi')$ of the object. The cross section is defined so that the power density at the radar receiver antenna is (DZ, 3.2)

$$P_{rant,m}(r''_m,\theta''_m,\phi''_m) = \left(\frac{P_t}{4\pi r_m^2}\right)\left(f_t^2(\theta_m,\phi_m)\right)\left(G_t\right)\left(l_t^{-1}\right)\left(\frac{\sigma_m(\theta',\phi')}{4\pi (r''_m)^2}\right)\left(l_r^{-1}\right), \tag{2.28}$$

where we have incorporated attenuation from the object to the radar receiver. The primes in the definition of σ_m and the double primes in $P_{rant,m}$ result from the receiver antenna not being collocated with the transmitter antenna. However, for most radar applications the transmitter and receiver antennas are collocated. In this case we are

interested only in the backscatter cross section and we set $\sigma_{\rm m}(\theta',\phi') = \sigma_{\rm b,m}$ and $(\theta''_{\rm m},\phi''_{\rm m}) = (\theta_{\rm m},\phi_{\rm m})$, and $r''_{\rm m} = r_{\rm m}$. Note that if we set (2.21) equal to (2.28), we have

$$A_{\rm r,m}(r_{\rm m},\theta_{\rm m},\phi_{\rm m}) = \sqrt{\frac{P_{\rm t}G_{\rm t}\eta_{\rm o}\sigma_{\rm b,m}}{8\pi^2 l_{\rm t}l_{\rm r}}}\,\frac{f_{\rm t}(\theta_{\rm m},\phi_{\rm m})}{r_{\rm m}^2} \tag{2.29}$$

for the scattered field amplitude at the receiver antenna.

The receiver antenna has an effective aperture $A_{\rm e}(\theta_{\rm m},\phi_{\rm m})$, so the power delivered by the antenna to the receiver is

$$P_{\rm r,m}(r_{\rm m},\theta_{\rm m},\phi_{\rm m}) = \Big(\frac{P_{\rm t}}{4\pi r_{\rm m}^2}\Big)\Big(f_{\rm t}^2(\theta_{\rm m},\phi_{\rm m})\Big)\Big(G_{\rm t}\Big)\Big(l_{\rm t}^{-1}\Big)\Big(\frac{\sigma_{\rm b,m}}{4\pi r_{\rm m}^2}\Big)\Big(l_{\rm r}^{-1}\Big)\Big(A_{\rm e}(\theta_{\rm m},\phi_{\rm m})\Big). \tag{2.30}$$

Doviak and Zrnic (DZ, 3.4) demonstrate that

$$A_{\rm e}(\theta_{\rm m},\phi_{\rm m}) = \Big(\frac{G_{\rm r}\lambda_{\rm c}^2}{4\pi}\Big)f_{\rm r}^2(\theta_{\rm m},\phi_{\rm m}), \tag{2.31}$$

so the average return power at the receiver antenna output port becomes

$$P_{\rm r,m}(r_{\rm m},\theta_{\rm m},\phi_{\rm m}) = \Big(\frac{P_{\rm t}}{4\pi r_{\rm m}^2}\Big)\Big(f_{\rm t}^2(\theta_{\rm m},\phi_{\rm m})\Big)\Big(G_{\rm t}\Big)\Big(l_{\rm t}^{-1}\Big)\Big(\frac{\sigma_{\rm b,m}}{4\pi r_{\rm m}^2}\Big)\Big(l_{\rm r}^{-1}\Big)\Big(\frac{G_{\rm r}\lambda_{\rm c}^2}{4\pi}f_{\rm r}^2(\theta_{\rm m},\phi_{\rm m})\Big), \tag{2.32}$$

which is known as the radar equation for a single point target. For most radars, including the Pennsylvania State University radar system, $G_{\rm t} = G_{\rm r} = G$, $f_{\rm t} = f_{\rm r} = f$, and $l_{\rm t} = l_{\rm r} = l$. Therefore, we write the radar equation for scattering by an isolated target as (DZ, 3.4)

$$P_{\rm r,m}(r_{\rm m},\theta_{\rm m},\phi_{\rm m}) = \frac{P_{\rm t}f^4(\theta_{\rm m},\phi_{\rm m})G^2\sigma_{\rm b,m}\lambda_{\rm c}^2}{(4\pi)^3 r^4 l^2}. \tag{2.33}$$

2.2.2 Scattering from Many Particles

Meteorological targets, unfortunately, are not point targets. They are usually collections of particles described by a distribution function $N(\mathbf{D},\mathbf{r})$, where N represents the number of particles per unit volume with characteristic size $\mathbf{D}$ at location $\mathbf{r}$. For most applications in the literature, the targets are generally treated as spheres with $\mathbf{D}$ simply representing the diameter D of the particles. If $\sigma(\mathbf{D})$ describes the backscattering cross section of particles with characteristic size $\mathbf{D}$, then the total backscattering cross section per unit volume is (DZ, 4.4)

$$\eta(\mathbf{r}) = \int_{\mathbf{D}} \sigma(\mathbf{D})N(\mathbf{D},\mathbf{r})d\mathbf{D}. \tag{2.34}$$

Substituting $\eta(\mathbf{r})\,dV$ for $\sigma_{\rm b,m}$ in (2.33), where dV is the volume element in spherical coordinates, i.e., $dV = r^2\sin\theta d\theta d\phi dr$, the return power from the resolution volume,

or spherical shell of particles, becomes (DZ, 4.4)

$$P_r(r,\theta,\phi) = \int_{r_b}^{r_t}\int_0^{\pi}\int_0^{2\pi} \frac{P_t f^4(\theta,\phi) G^2 [\eta(\mathbf{r})\, dV]\lambda_c^2}{(4\pi)^3 r^4 l^2}. \tag{2.35}$$

There are two important points about this equation: 1) we have neglected multiple scattering effects because these effects are extremely small; and 2) we have implicity assumed that coherence effects between the particles are negligible. The limits r_b and r_t are set by the pulse width and the distance to the target (Figures 7 and 8). Even though the integration over θ is from 0 to π, most of the contribution to the integral comes from the primary forward lobe of the antenna pattern. For the Pennsylvania State University cloud radar the beamwidth at the half-maximum of the primary lobe is 0.24°. If the resolution volume is sufficiently small, $\eta(r,\theta,\phi) \approx \eta(\mathbf{r}_o)$ and (2.35) becomes

$$P_r(\mathbf{r}_o) = \int_{r_b}^{r_t}\int_0^{\pi}\int_0^{2\pi} \frac{P_t G^2 \lambda^2 \eta(\mathbf{r}_o)}{(4\pi)^3 r_o^2 l^2(\mathbf{r}_o)} f^4(\theta,\phi)\sin\theta d\theta d\phi dr. \tag{2.36}$$

For a circularly symmetric, Gaussian-shaped beam pattern (DZ, 4.13)

$$\int_0^{\pi}\int_0^{2\pi} f^4(\theta,\phi)\sin\theta d\theta d\phi = \frac{\pi\theta_1^2}{8\ln 2}, \tag{2.37}$$

and the received power becomes (DZ, 4.4)

$$P_r(\mathbf{r}_o) = \frac{P_t G^2 \lambda^2 \eta(\mathbf{r}_o) c\tau_{pw}\pi\theta_1^2}{(4\pi)^3 r_o^2 l^2(\mathbf{r}_o) 16\ln 2}, \tag{2.38}$$

where we have replaced the radial increment, or radar resolution length, dr with $c\tau_{pw}/2$ for reasons which we will explain shortly. At first glance the derivation of $P_r(\mathbf{r}_o)$ seems innocuous enough, but there are some implicit assumptions in the derivation that hide a fair bit of the complexity that is at the heart of weather-radar signal processing. We will discuss these issues in the context of the signals that emerge from the I and Q demodulators (Figure 2), but before doing so we want to discuss the limits on the integral in (2.35) in a bit more detail.

Chapter 3
The Radar Resolution Volume

3.1 Radar Resolution Volume along the Beam Direction

At this point we want to emphasize the difference between a resolution volume containing a single target and one containing many targets. Consider a single pulse travelling through space along a given direction (Figure 7). Now suppose a single scatterer is located at a distance $r_o = ct_o$ from the radar. The leading edge of the pulse encounters the object at time t_o. Since there are no other scatterers involved in this example, the back edge of the pulse undergoes no scattering until it, too, encounters the object at r_o. Scatter from the leading edge of the pulse reaches the radar at time $2t_o$, whereas scatter from the back edge of the pulse does not reach the receiver antenna until time $2t_o + \tau_{pw}$, where τ_{pw} is the transmitted pulse width in units of time. At any time t such that $2t_o \leq t \leq 2t_o + \tau_{pw}$, the receiver antenna is illuminated only from radiation originating from the target located at $r_o = ct_o$. Therefore, analysis of the radar signal over any time interval during this time period leads to information on the scatterer at r_o.

The scenario is quite different when many scatterers are located in and around the scatterer at r_o (Figure 8). As before, consider the case when the leading edge of the pulse encounters the object at r_o at time $t = t_o$ (Figure 8b). The backscatter from this encounter reaches position $r_o - c\tau_{pw}/2$ at time $t_o + \tau_{pw}/2$. At this time, however, the back edge of the pulse is also at location $r_o - c\tau_{pw}/2$ (Figure 8c). If the back edge of the pulse undergoes scattering at this point, then the scatter from the leading edge of the pulse at position r_o reaches the receiver antenna at exactly the same time as the scatter from the trailing edge of the pulse at $r_o - c\tau_{pw}/2$ (Figure 8d). In fact, at time $2t_o$ the radar receives scattered waves from all points located between $r_o - c\tau_{pw}/2$ and r_o; this region of space is the resolution volume of the radar at the time $2t_o$ (Figure 8d).

As in the single scatterer case, the radar receives a scattered field from position r_o for all times t such that $2t_o \leq t \leq 2t_o + \tau_{pw}$; however, at the time $2t_o$ the radar also receives energy from the region between $r_o - c\tau_{pw}/2$ and r_o, whereas at time $2t_o + \tau_{pw}$ it receives

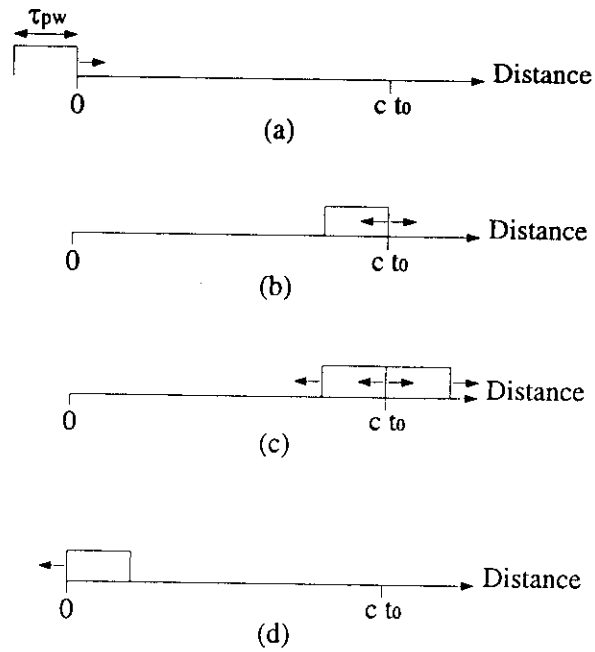

Figure 7. Cartoon illustration of a transmitted pulse scattering off a single, isolated scatterer. The pulse width is τ_{pw} and the distance from the radar to the target is ct_0.

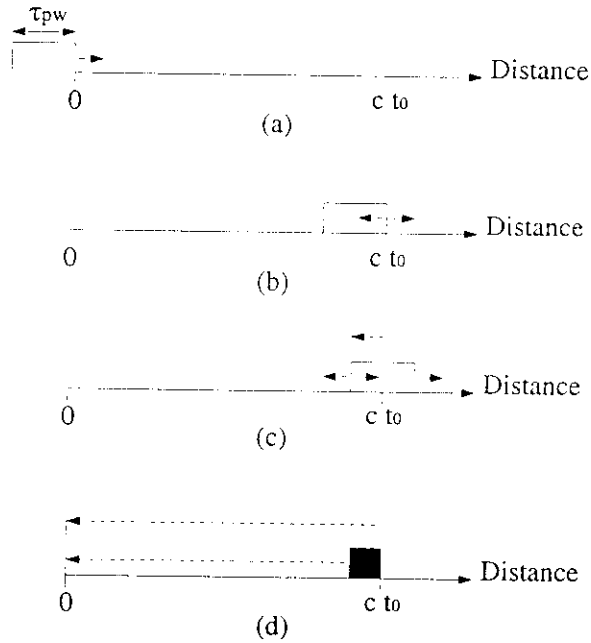

Figure 8. Cartoon illustration of a transmitted pulse scattering off a collection of particles indicated by the filled square in (d). The pulse width is τ_{pw} and the distance from the radar to the center of the target is $ct_0 - c\tau_{pw}/4$.

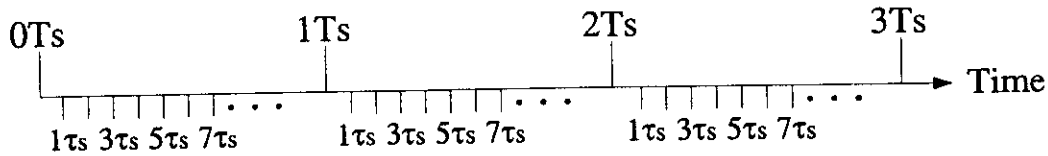

Figure 9. The time between radar pulses is T_s and the time between receiver power samples is τ_s.

energy from all points between r_o and $r_o + c\tau_{pw}/2$. It no longer makes sense to analyze the properties of the pulse from $2t_o \leq t \leq 2t_o + \tau_{pw}$ to infer properties about the scatterer located at position r_o since the radar is receiving energy from different points in space during this interval. To study the properties of scatterers in a fixed region of space, say from $r_o - c\tau_{pw}/2$ to r_o, only the radiation that reaches the receiver antenna at the precise time of $2t_o$ is of value.

Let T_s represent the time between radar pulses and let τ_s represent the time between power samples that are collected by the radar receiver (Figure 9). (Do not confuse the time between consecutive samples, i.e., τ_s, with the pulse width of the radar, i.e., τ_{pw}!) In this setup the first pulse is sent out at time $0T_s$ and samples are collected at times $0T_s + \tau_s$, $0T_s + 2\tau_s$, etc... The second pulse leaves the transmitter antenna at time $1T_s$ and samples are then collected at times $1T_s + \tau_s$, $1T_s + 2\tau_s$, etc... The number of distinct resolution volumes in space from which the radar collects information is equal to the number of samples N_g that are collected by the radar between any two radar pulses. The samples collected at the times $0T_s + j\tau_s$, $1T_s + j\tau_s$, etc... are from the same resolution volume whose center is located at

$$r_j = c\frac{j\tau_s}{2} - \frac{c\tau_{pw}}{4} = \frac{c}{2}\left(j\tau_s - \frac{\tau_{pw}}{2}\right). \tag{3.1}$$

Therefore, the radar receiver generates series of snap shots of the return signals that correspond to specific regions in space. The region in space is easily indentified from the delay $t = j\tau_s$ between the initiation of the pulse and the time the signal is sampled, as well as the pulse width τ_{pw} itself. The time interval between each sample is simply T_s. With this notation in hand we write the limits r_b and r_t in (2.35) as $(c/2)(j\tau_s - \tau_{pw})$ and $(c/2)(j\tau_s)$, respectively. In (2.38) we approximated dr by the difference of these two limits, i.e., $c\tau_{pw}/2$.

3.2 Radar Resolution Volume Perpendicular to the Beam Direction

The electromagnetic wave propagating from the transmitter antenna to the atmosphere is not contained within a single, well-defined direction. Rather, the field leaving the antenna (actually scattered by the antenna) to the atmosphere sets up interference patterns so that the strength of the field is significantly different from 0 in a number of different directions (Figure 6). Fortunately, the power in the forward lobe is 177.8 times, or 22.5 dB above, the power in the next most significant side lobe. For all practical purposes, therefore, the side lobes can be neglected in power calculations without introducing significant error. For example, the derivation of (2.37) is based on a single, Gaussian-shaped antenna beam in the forward direction. The side lobes can lead to returned power from objects that are located to the side of the radar, which can be problematic; however, these ground clutter issues are insignificant for the Pennsylvania State University radar since the beam is narrow. The nonzero width of the beam within the main lobe leads to a resolution volume that increases in size with distance from the radar.

Chapter 4
The Radar Receiver

4.1 Signal Transformations in the Radar Receiver

From the receiver antenna output port the electromagnetic radiation propagates along a short stretch of waveguide to the mixer and preamplifier assembly. In the mixer and preamplifier unit the physical nature of the signal is transformed from a time-dependent, transverse electromagnetic wave at the input to a time-dependent voltage at the output which is subsequently passed through the rest of the signal processing chain by coaxial cable. Furthermore, the high carrier frequency ω_c is transformed to a much lower intermediate frequency ω_i. We write the signal voltage at the ouput of the mixer and preamplifier unit due to a single point target as

$$V_{mix,m}(t) = V_{mix,m} e^{i[2k_c r - (\omega_i + \omega_{d,m})t + \phi_{s,m} + \phi_t]}, \tag{4.1}$$

where the amplitude $V_{mix,m}$ depends upon gains and losses in the mixer and preamplifier assembly, as well as the electromagnetic field strength $A_{r,m}(r, \theta, \phi)$. At this point the signal is split into two branches: one branch is input to the incoherent receiver path and the other branch passes to the coherent, or Doppler, receiver unit. We describe the coherent receiver here and refer the reader to the article of Clothiaux et al. (1995) for a description of the incoherent path power estimates produced by the Pennsylvania State University radar.

The signal passes to the I and Q demodulators with only power gains and losses affecting it. In the I and Q demodulators an important transformation of the signal occurs. To remove ω_i from the signal, the physical voltage, i.e., the real part of (4.1) after amplification,

$$V_{iq,m}(t) = V_{iq,m} \cos\Big[\alpha(t)\Big], \tag{4.2}$$

where

$$\alpha(t) = 2k_c r - (\omega_i + \omega_{d,m})t + \phi_{s,m} + \phi_t, \tag{4.3}$$

is mulitplied by the two reference voltages

$$V_{ref}^{I}(t) = V_{ref,o}\cos\Big[\beta(t)\Big] \tag{4.4}$$

and

$$V_{ref}^{Q}(t) = V_{ref,o}\cos\Big[\beta(t) - \frac{\pi}{2}\Big], \tag{4.5}$$

where $\beta(t) = -\omega_i t + \phi_t$. The reference voltages have their origin in a sample of the transmitted signal that is eventually input to the I and Q demodulators through the coherent oscillator, or COHO (Figure 2). The multiplication process in the demodulators performs a transformation of the signal that is comparable to the trigonometric identity

$$\cos(\alpha)\cos(\beta) = \frac{1}{2}\Big[\cos(\alpha+\beta) + \cos(\alpha-\beta)\Big]. \tag{4.6}$$

A low-pass filter at the output of the demodulators removes the high frequency term containing $\cos(\alpha+\beta)$, together with any other frequecies much greater than $\alpha - \beta$ due to nonlinearities in the mixer, with the result that

$$I(t) = \text{Low Frequency Part}[V_{iq,m}(t)V_{ref}^{I}(t)] = V_{o,m}\cos[2k_c r - \omega_{d,m}t + \phi_{s,m}], \tag{4.7}$$

and

$$Q(t) = \text{Low Frequency Part}[V_{iq,m}V_{ref}^{Q}(t)] = V_{o,m}\sin[2k_c r - \omega_{d,m}t + \phi_{s,m}]. \tag{4.8}$$

We emphasize that no matter what the nature of the electomagnetic field is at the receiver antenna output port, the result of the coherent path signal processing is to strip off the carrier frequency and create the $I(t)$ and $Q(t)$ signal voltages. The voltage amplitudes of $I(t)$ and $Q(t)$ are always a faithful representation of the electromagnetic field strength at the receiver antenna output port. If the gains G_{sys} and losses L_{sys} from the receiver antenna to the output of the demodulators are known, then the amplitudes of $I(t)$ and $Q(t)$ can be used to produce estimates of the electromagnetic field strength at the receiver antenna. Furthermore, the variations in time of the $I(t)$ and $Q(t)$ signals enable one to produce power density spectra of the signal from which estimates of the velocities of the scattterers relative to the radar are derived.

4.2 Estimating Received Power from an Isolated Scatterer

The average power in the electromagnetic field at the receiver antenna due to scattering from a single, isolated particle is proportional to the real part of the electric field squared averaged over a period $T_{ant} = 2\pi/(\omega_c + \omega_{d,m})$ of the Doppler shifted wave:

$$P_{rant,m}(r,\theta,\phi) = \frac{[A_{r,m}(r,\theta,\phi)]^2}{\eta_o}\Big[\frac{1}{T_{ant}}\int_0^{T_{ant}}\cos^2[2k_c r - (\omega_c+\omega_{d,m})t + \phi_{s,m} + \phi_t]dt\Big]. \tag{4.9}$$

As before, the factor in brackets is 1/2 so that

$$P_{rant,m}(r,\theta,\phi) = \frac{[A_{r,m}(r,\theta,\phi)]^2}{2\eta_o}. \tag{4.10}$$

Therefore, apart from a constant of proportionality, the power averaged over a cycle of the wave is simply the wave amplitude squared and divided by two.

This same power can be estimated from either the $I(t)$ or $Q(t)$ signal voltages. Consider $I(t)$ from (4.7). The instantaneous power in $I(t)$ is

$$P_{iq,m}(t) = \frac{I^2(t)}{R_{ref}}, \tag{4.11}$$

where R_{ref} is the appropriate impedance. Therefore, the power averaged over the period $T_{iq} = 2\pi/\omega_{d,m}$ is

$$P_{iq,m}(t) = \frac{V_{o,m}^2}{R_{ref}} \frac{1}{T_{iq}} \int_0^{T_{iq}} \cos^2[2k_c r - \omega_{d,m} t + \phi_{s,m}] dt = \frac{V_{o,m}^2}{2R_{ref}}. \tag{4.12}$$

Assuming that we know G_{sys} and L_{sys}, as well as the receiver antenna aperture $A_e(\theta,\phi)$, we have

$$P_{rant,m}(t) = \frac{P_{iq}(t)}{A_e(\theta,\phi) G_{sys} L_{sys}^{-1}}. \tag{4.13}$$

Since $I(t)$ and $Q(t)$ are sinusoidal in time, there is a much simpler way to determine $P_{iq,m}(t)$; however, we must use a complex value representation for the voltage:

$$P_{iq,m}(t) = \frac{[\mathcal{I}(t)][\mathcal{I}^*(t)]}{2R_{ref}}$$

or

$$P_{iq,m}(t) = \frac{1}{2R_{ref}} [V_{o,m} e^{i(2k_c r - \omega_{d,m} t + \phi_{s,m})}][V_{o,m} e^{-i(2k_c r - \omega_{d,m} t + \phi_{s,m})}] = \frac{V_{o,m}^2}{2R_{ref}}, \tag{4.14}$$

where $\mathcal{I}^*(t)$ is the complex conjugate of $\mathcal{I}(t)$. At this point it is instructive to expand the exponentials in (4.14) using Euler's equation to get

$$P_{iq,m}(t) = \frac{V_{o,m}^2}{2R_{ref}} \Big(\cos^2[2k_c r - \omega_{d,m} t + \phi_{s,m}] + \sin^2[2k_c r - \omega_{d,m} t + \phi_{s,m}] \Big). \tag{4.15}$$

Comparing (4.7) and (4.8) to (4.15), we can write

$$P_{iq,m}(t) = \frac{1}{R_{ref}} \Big(\frac{I^2(t)}{2} + \frac{Q^2(t)}{2} \Big). \tag{4.16}$$

Therefore, given instantaneous measurements of $I(t)$ and $Q(t)$, (4.16) can be used as a simple recipe to calculate the power over a cycle of the wave. This method of obtaining the average power in the $I(t)$ and $Q(t)$ signals is true only if they vary approximately as sinusoids in time.

4.3 Estimating Received Power from Many Scatterers

Now that we have calculated the backscattered power due to a single point target, let us see what happens when we introduce a second target in the resolution volume. The electromagnetic field scattered to the radar becomes

$$\mathcal{E}_{rant}(t) = A_{r,m}e^{i[2k_c r_m - (\omega_c+\omega_{d,m})t+\phi_{s,m}+\phi_t]} + A_{r,n}e^{i[2k_c r_n - (\omega_c+\omega_{d,n})t+\phi_{s,n}+\phi_t]}. \tag{4.17}$$

The power averaged over a time interval large compared to $2\pi/\omega_c$ but small compared to the time intervals $2\pi/\omega_{d,m}$ and $2\pi/\omega_{d,n}$ is

$$P_{rant}(t) = \frac{\mathcal{E}_{rant}(t)\mathcal{E}^*_{rant}(t)}{2\eta_o} \tag{4.18}$$

or

$$P_{rant}(t) = \frac{1}{2\eta_o}\Big((A_{r,m})^2 + (A_{r,n})^2 + A_{r,m}A_{r,n}e^{i[2k_c(r_m-r_n)-(\omega_{d,m}-\omega_{d,n})t+(\phi_{s,m}-\phi_{s,n})]} \tag{4.19}$$

$$+A_{r,n}A_{r,m}e^{-i[2k_c(r_m-r_n)-(\omega_{d,m}-\omega_{d,n})t+(\phi_{s,m}-\phi_{s,n})]}\Big).$$

Expanding the exponentials yields

$$P_{rant}(t) = \frac{1}{2\eta_o}\Big((A_{r,m})^2 + (A_{r,n})^2 \tag{4.20}$$

$$+2A_{r,m}A_{r,n}\cos[2k_c(r_m - r_n) - (\omega_{d,m} - \omega_{d,n})t + (\phi_{s,m} - \phi_{s,n})]\Big).$$

If one considers all of the scatterers N_s per unit volume, the power becomes

$$P_{rant}(t) = \frac{1}{2\eta_o}\sum_{m=1}^{N_s}(A_{r,m})^2 + \frac{1}{2\eta_o}\sum_{m\neq n}^{N_s} A_{r,m}A_{r,n}e^{i[2k_c(r_m-r_n)-(\omega_{d,m}-\omega_{d,n})t+(\phi_{s,m}-\phi_{s,n})]}. \tag{4.21}$$

The information dependent on the total cross section of the scatterers is contained in the first sum. Therefore, if we can adopt a processing strategy that drives the contribution of the second term to zero, we can recover the total cross section in the resolution volume. Fortunately, if P_{rant} is measured repeatedly over a time interval long compared with the time intervals $2\pi/(\omega_{d,m} - \omega_{d,n}), m \neq n$, and averaged, the second sum does indeed go to zero. Therefore, we can write

$$P_{rant} = \lim_{N_n\to\infty}\Big[\frac{1}{N_n}\sum_{j=1}^{N_n} P_{rant,j}\Big] = \frac{1}{2\eta_o}\sum_{m=1}^{N_s}(A_{r,m})^2, \tag{4.22}$$

where N_n is the number of samples in the average. Therefore, (2.38) for $P_r(\mathbf{r}_o)$ holds true as long as many power samples are collected over a sufficiently long period of time and then averaged.

Extending the above argument, when many scatterers are in the resolution volume, the scattered electric field at the receiver antenna is

$$\mathcal{E}_{rant}(t) = \sum_{m=1}^{N_s} A_{r,m} e^{i[2k_c r_m - (\omega_c - \omega_{d,m})t + \phi_{s,m} + \phi_t]}. \tag{4.23}$$

In terms of $I(t)$ and $Q(t)$ we have (DZ, 4.3)

$$I(t) = \mathcal{R}\Big(\sum_{m=1}^{N_s} V_{o,m} e^{i[2k_c r_m - \omega_{d,m} t + \phi_{s,m}]} \Big) \tag{4.24}$$

and

$$Q(t) = \mathcal{I}\Big(\sum_{m=1}^{N_s} V_{o,m} e^{i[2k_c r_m - \omega_{d,m} t + \phi_{s,m}]} \Big), \tag{4.25}$$

or

$$I(t) = \sum_{m=1}^{N_s} V_{o,m} \cos[2k_c r_m - \omega_{d,m} t + \phi_{s,m}] \tag{4.26}$$

and

$$Q(t) = \sum_{m=1}^{N_s} V_{o,m} \sin[2k_c r_m - \omega_{d,m} t + \phi_{s,m}]. \tag{4.27}$$

Using (2.16), (4.10), (4.13) and (4.14), we can write the voltage amplitudes $V_{o,m}$ as

$$V_{o,m} = \sqrt{2 R_{ref} G_{sys} L_{sys}^{-1} A_e(\theta, \phi) P_{rant,m}(r, \theta, \phi)} \tag{4.28}$$

or

$$V_{o,m} = \sqrt{\frac{R_{ref} G_{sys} L_{sys}^{-1} A_e(\theta, \phi)}{\eta_o l}} \frac{S_{2,m}(180°) A_i(\theta, \phi)}{k_c r^2}, \tag{4.29}$$

where we have included the loss l that we neglected in (2.16).

Note that we can write the sums for $I(t)$ and $Q(t)$ as

$$I(\tau_s, T_s) = |V_o(\tau_s, T_s)| \cos[\theta(\tau_s, T_s)] \tag{4.30}$$

and

$$Q(\tau_s, T_s) = |V_o(\tau_s, T_s)| \sin[\theta(\tau_s, T_s)], \tag{4.31}$$

where τ_s indicates the time interval between the radar sending out a pulse and receiving the backscatter from the pulse (i.e., τ_s represents range) and T_s is the time interval between pulses (DZ, 4.3). Since the summed $I(\tau_s, T_s)$ and $Q(\tau_s, T_s)$ voltages can be represented as sinusoids, we can estimate the power over a cycle using (4.16).

Chapter 5
An Example

Before discussing the properties of the $I(t)$ and $Q(t)$ voltages, as well as the Doppler moments, we thought that it would be instructive to illustrate all of the previous discussion with a realistic, but computer simulated, "meteorological target." To this end we illustrate the results of a forward computer simulation in which we explicity calculate the $I(t)$ and $Q(t)$ voltages for a specified drop size distribution located within a specified resolution volume. *In situ* measurements by particle counting probes on the University of Wyoming King Air aircraft during a field experiment in the Central Pennsylvania area produced the drop size distribution illustrated in Figure 10, which we use as input to the simulation. Multiplying the number densities measured in each bin by the radar resolution volume yields the total number of drops $N_{inbin}^{orig}[i]$ in each bin i that we must take into account in the simulation. Unfortunately, as Figure 10 illustrates, the number of drops in the radar resolution volume (3.08×10^{11} in this example) is to large to

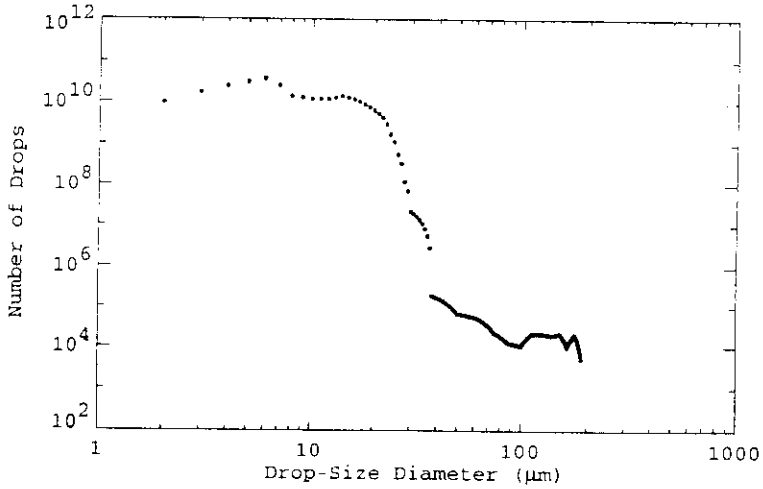

Figure 10. Drop size distribution measured by FSSP, 2D-C and 2D-P probes on board the University of Wyoming King Air aircraft during an experiment at Rock Springs, Pennsylvania, in the Spring of 1995, that are scaled to the radar resolution volume. The measurements were obtained in a stratus deck when the aircraft altitude was approximately 1 km above the surface.

simulate on modern day computers, so we devised the following scheme to make the computer memory requirements manageable. The exact expression for $I(t)$, with a similar expression for $Q(t)$, is

$$I(t) = \sum_{m=1}^{3.08\times10^{11}} V_{o,m} \cos[2k_c r_m - \omega_{d,m} t + \phi_{s,m}]. \tag{5.1}$$

Instead of using (5.1) in the simulations, we replace it with

$$I(t) = \sum_{i=1}^{N_{bins}} \sum_{j=1}^{N_{inbin}[i]} S_{(i,j)} V_{(i,j)} \cos[2k_c r_{(i,j)} - \omega_{d,(i,j)} t + \phi_{s,i}], \tag{5.2}$$

where

$$N_{inbin}[i] = \begin{cases} N_{binmax}, & \text{if } N_{binmax} \le N^{orig}_{inbin}[i], \\ N^{orig}_{inbin}[i], & \text{if } N^{orig}_{inbin}[i] < N_{binmax}, \end{cases} \tag{5.3}$$

$$S_{(i,j)} = \begin{cases} \sqrt{N^{orig}_{inbin}[i] \text{ DIV } N_{binmax} + 1}, & \text{if } j < (N^{orig}_{inbin}[i] \text{ MOD } N_{binmax}), \\ \sqrt{N^{orig}_{inbin}[i] \text{ DIV } N_{binmax}}, & \text{if } j \ge (N^{orig}_{inbin}[i] \text{ MOD } N_{binmax}), \end{cases} \tag{5.4}$$

$V_{(i,j)}$, $r_{(i,j)}$ and $\omega_{d,(i,j)}$ are properties attributed to the j^{th} particle in the i^{th} bin, and $\phi_{s,i}$ is the phase shift upon scattering from particle sizes corresponding to the i^{th} bin. The operation DIV implies integer division with no remainder and MOD stands for the modulo operation. For the results we present here $N_{binmax} = 1000$. The equation in (5.2) attempts to produce the same fluctuations and magnitudes in the $I(t)$ voltages as the exact expression (5.1). The motivation for this scheme is the observation that nearly identical distributions of voltages over many samples, say 100 000, can be produced by expressions such as

$$I_a = \sum_{i=1}^{5000} \cos(2\pi r_i) \tag{5.5}$$

and

$$I_b = \sum_{i=1}^{1000} \sqrt{5} \cos(2\pi r_i), \tag{5.6}$$

where r_i is a pseudorandom number between 0 and 1 and the factor $\sqrt{5}$ in (5.6) scales the amplitude of I_b to match that of I_a in (5.5) (Figure 11). The square root factor in (5.6) corresponds to the scale factor $S_{(i,j)}$ in (5.2) and $V_{(i,j)}$ is implicitly set to one both in (5.5) and (5.6).

In the simulation we use a pseudorandom number generator to randomly distribute the particles within the simulated radar resolution volume. Since the distribution in Figure 10 contained only liquid water, we assume that the drops are liquid water spheres. Therefore, the theory for scattering from spherical particles, i.e., "Mie" theory, is an appropriate tool to calculate the scattering amplitude matrix element $S_{2,m}(180°)$

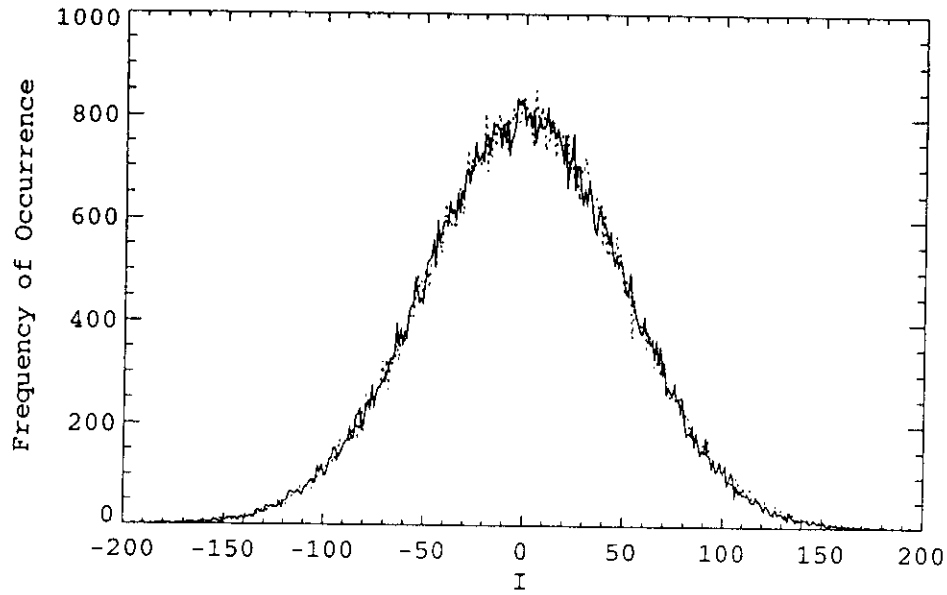

Figure 11. Frequency of occurrence of I_a (solid line) and I_b (dashed line) defined in (5.5) and (5.6), respectively. We used 100 000 samples to generate the histograms.

of the drops as a function of size. The equations for computing $S_{2,m}(180°)$ come from Bohren and Huffman (1983); in fact, Bohren and Huffman (BH, 4.6) provide the equation for $S_{2,m}(180°)$ and they also provide code that computes $S_{2,m}(180°)$ (BH, Appendix A). Once the location $r_{(i,j)}$ and scattering matrix element $S_{2,m}(180°)$ are computed for each particle, we compute the resulting voltage amplitude $V_{(i,j)}$ using (4.29). We then calculate the $I(t)$ and $Q(t)$ voltages using (5.2) with time $t = 0$. To simulate the particles falling within the resolution volume, we simply must advance the time t in (5.2). Since we must take snapshots of the $I(t)$ and $Q(t)$ voltages at the pulse repetition frequency f_{prf} of the radar, we advance the time in increments of $T_s = 1/f_{prf}$. The Doppler shifts in (5.2) are related to the particle fall velocities by

$$\omega_m = -\left(\frac{4\pi v_m}{\lambda_c}\right). \tag{5.7}$$

In the simulation we assume that the particle fall speeds are related to the particle drop diameter by

$$v(D) = \begin{cases} 4D(1 - e^{-12D}), & \text{if D} \leq .75\,\text{mm}; \\ 9.65 - 10.43e^{-0.6D}, & \text{if } .75\,\text{mm} \leq \text{D}, \end{cases} \tag{5.8}$$

where D is the diameter of the particle in mm and the velocity v has units of m/s (Rogers et al., 1993). The resulting series of $I(t)$ and $Q(t)$ voltages are illustrated in Figure 12.

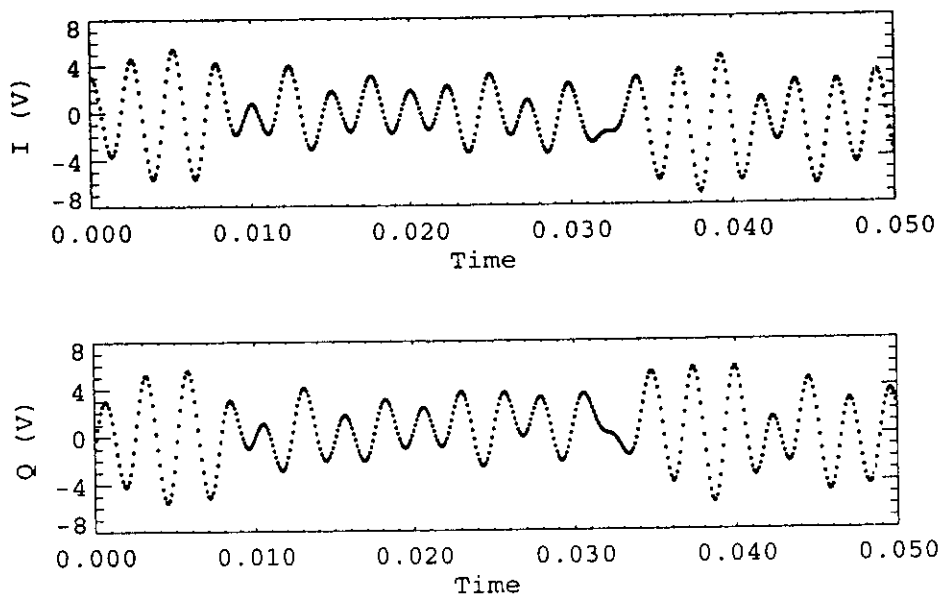

Figure 12. The first 50 I and Q signal voltages generated by the forward simulation of the Pennsylvania State University 94-GHz cloud radar using the particle drop size distribution in Figure 10 as input.

Chapter 6
Radar Return Signal Statistics

6.1 I and Q Voltage Statistics

Now that we have the $I(t)$ and $Q(t)$ voltages, and hence the received power $P_{rant}(t)$, in hand, we can now obtain estimates of some of their statistical properties. Recall that both the $I(t)$ and $Q(t)$ voltages contain sums of sines and cosines with arguments that contain the terms

$$2k_c r_m - \omega_{d,m} t + \phi_{s,m}. \tag{6.1}$$

We cannot emphasize the next two points strongly enough. The first point is that the remainder of $2k_c r_m$ MOD 2π is a random variable with a uniform distribution over the interval from 0 to 2π. That is, since the exact locations of the scatterers are random across the resolution volume, there is no fixed relation between $2k_c r$ from one particle to the next and the phases $2k_c r_m$ MOD 2π end up uniformly distributed over 0 to 2π. Therefore, the sums of the cosines and sines in $I(t)$ and $Q(t)$ are random variables distributed between -1 and 1. The second point, which is based on the Central Limit Theorem, is that a variable that is the sum of random variables of equal magnitudes tends to be Gaussian-distributed when a large number of terms are involved. Since the $I(t)$ and $Q(t)$ voltage amplitudes $V_{o,m}$ are due to a "well-behaved" particle size distribution where no one magnitude is significantly larger than all of the other magnitudes, a series of measurements of either $I(t)$ or $Q(t)$, if long enough, produces values that are Gaussian-distributed (Figure 13).

The $I(t)$ and $Q(t)$ voltages have a number of other interesting properties. At a single, "isolated" instant in time one cannot predict the exact value of $I(t)$ because one cannot know ahead of time the exact location of each of the particles in the resolution volume. This is not to say that one cannot predict the value of $I(t)$ an instant after a measurement of $I(t)$; if two samples of $I(t)$ are obtained in a vanishingly short period of time, their values converge. (In Figure 12 neighboring $I(t)$ voltages in time are always

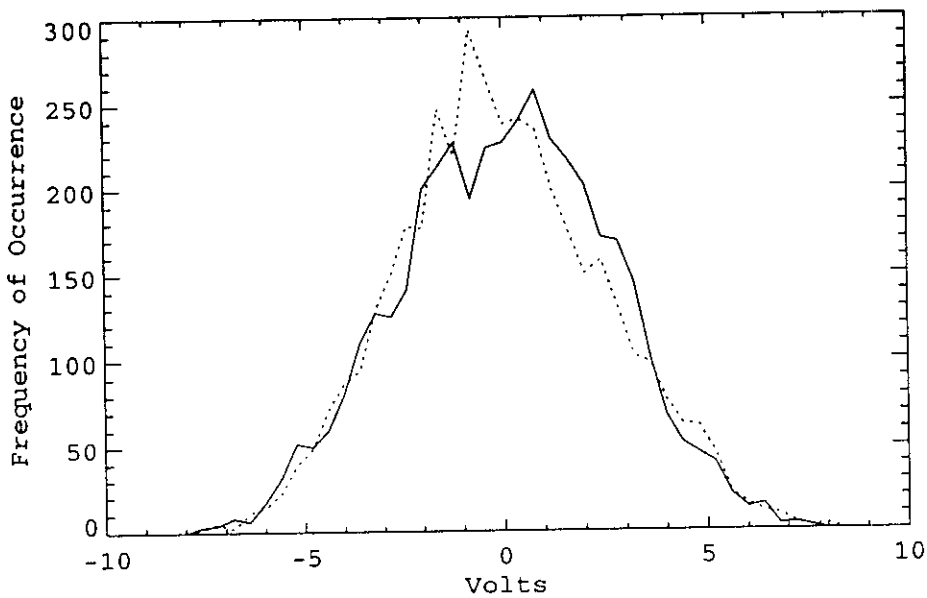

Figure 13. Frequency of occurrence of I (solid line) and Q (dashed line) for the 4096 samples of the forward simulation.

similar in magnitude.) Knowing $I(t)$ at one instant does provide some useful information in figuring out the values of $I(t)$ at later "not too far in the distant future" times. The autocorrelation function defined by

$$R(L) = \frac{\sum_{m=1}^{N_n-L}(I_m - \overline{I})(I_{m+L} - \overline{I})}{\sqrt{\sum_{m=1}^{N_n-L}(I_m - \overline{I})^2}\sqrt{\sum_{m=1}^{N_n-L}(I_{m+L} - \overline{I})}} \tag{6.2}$$

provides a quantitative assessment of how the $I(t)$ voltages are correlated when offset by a lag of L. As Figure 14 illustrates, the simulated $I(t)$ voltages are strongly correlated for small lag times and the correlation decreases as the lag time increases from zero. These same statements hold true for $Q(t)$ as well.

$I(t)$ and $Q(t)$, however, are not correlated; that is, knowing the value of $I(t)$ at some time does not provide any useful information in figuring out the value of $Q(t)$ at the same time and vice versa. In this case the correlation coefficient defined by

$$R(L) = \frac{\sum_{m=1}^{N_n-L}(I_m - \overline{I})(Q_{m+L} - \overline{Q})}{\sqrt{\sum_{m=1}^{N_n-L}(I_m - \overline{I})^2}\sqrt{\sum_{m=1}^{N_n-L}(Q_{m+L} - \overline{Q})}} \tag{6.3}$$

with the lag $L = 0$ should be close to 0. For the time series in Figure 12, the correlation coefficient for lag $L = 0$ is indeed close to 0. Since the same random processes are controlling the evolution of $I(t)$ and $Q(t)$, knowing $I(t)$ at one instant does provide some useful information in figuring out the values of $Q(t)$ at later "not too far in the distant

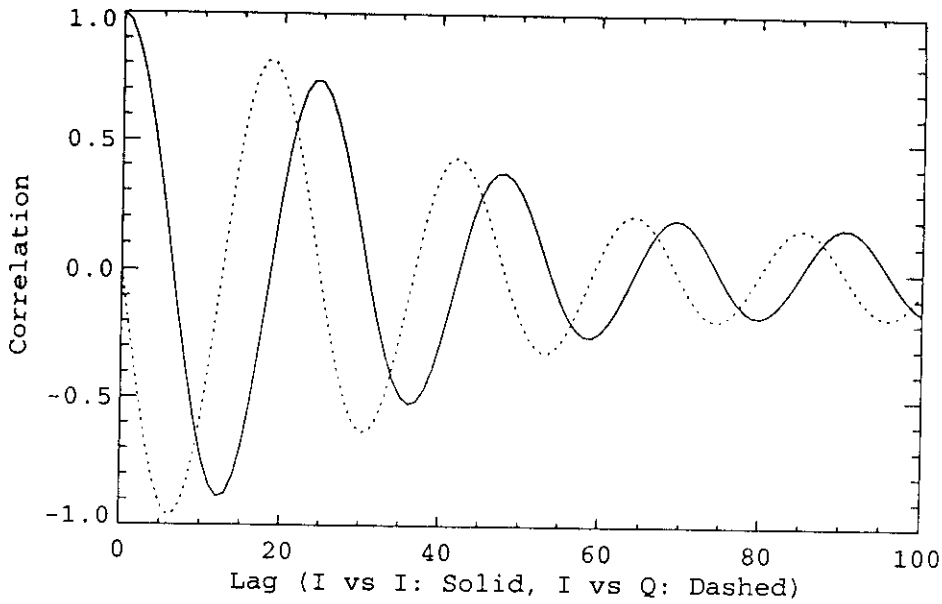

Figure 14. Correlation of I with itself (solid line) and with Q (dashed line) for lag times from 0 to 30 T_s, where $T_s = 0.0001$ is the simulated pulse repetition period for the forward simulation.

future" times and vice versa. Consequently, the magnitude of the correlation between $I(t)$ and $Q(t)$ as defined by (6.3) increases as the lag L increases from zero (Figure 14).

6.2 Signal Power Statistics

Since $I(t)$ and $Q(t)$ are Gaussian-distributed independent processes, we have (DZ, 4.4)

$$p[I(t)] = \frac{1}{\sqrt{2\pi}\sigma} e^{-I^2(t)/2\sigma^2}, \tag{6.4}$$

$$p[Q(t)] = \frac{1}{\sqrt{2\pi}\sigma} e^{-Q^2(t)/2\sigma^2}, \tag{6.5}$$

and

$$p[I(t) \cap Q(t)] = p[I(t)]\, p[Q(t)] = \frac{1}{2\pi\sigma^2} e^{[-I^2(t)-Q^2(t)]/2\sigma^2}. \tag{6.6}$$

For the present discussion we simply note that the power $P_{rant}(t)$ goes as $I^2(t) + Q^2(t)$. Therefore, it should come as no surprize that we can write (DZ, 4.4)

$$p[P_{rant}(t)] = \frac{1}{2\sigma^2} e^{-P_{rant}(t)/2\sigma^2} \tag{6.7}$$

as the power probability density function for a large number of power returns from rain or perhaps a cloud. This distribution is an exponential distribution with a peak probability of zero and a mean value of $P_o = 2\sigma^2$.

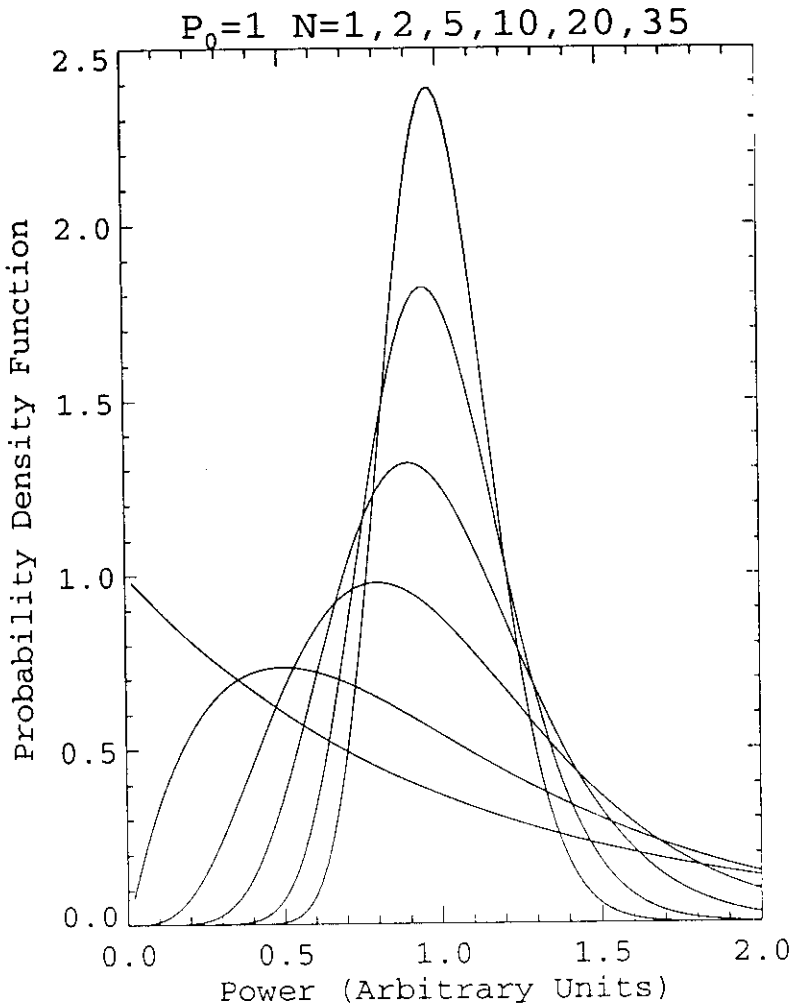

Figure 15. Probability density function defined by (6.8) using a mean power of $P_0 = 1$ and averaging 1, 2, 5, 10, 20 and 35 samples.

Since we already know that a single power measurement is, for all practical purposes, useless, knowing that individual power measurements are exponentially distributed is not really that helpful. What we really want to know is the probability density function for an average of N power samples $P_{rant}(t)$, or P_N. After some mathematical manipulations, that include application of the residue theorem from the theory of complex numbers, the problem is solved. The resulting probability density function is (Marshall and Hitschfeld, 1953)

$$p(P_N) = \frac{N^N (P_N)^{N-1}}{(P_o)^N (N-1)} e^{-NP_N/P_o}, \tag{6.8}$$

which we graph in Figure 15 for a range of values of N and a given, fixed value of σ.

6.3 Mixer Noise and the Minimum Detectable Received Signal

Now that we have characterized the scattered signal that comes back to the radar, we must now sort it out from the noise introduced by the detection process. Radars, unlike lidars, have one principle source of noise, namely, the mixer. The mixer noise process is governed by Johnson shot noise. The noise voltage is assumed to be a Gaussian-distributed random process with a mean voltage of zero and a standard deviation of

$$\sigma_v = \sqrt{P_n}, \tag{6.9}$$

where P_n is the average mixer noise power. ($P_n = 1.12 \times 10^{-9}$ mW for the Pennsylvania State University radar receiver.) That is, the probability of a noise voltage is

$$p[V_n(t)] = \frac{1}{\sqrt{2\pi}\sigma_v} e^{-V_n^2(t)/2\sigma_v^2}. \tag{6.10}$$

Comparing (6.4) and (6.5) to (6.10), we find that both the mixer noise and the $I(t)$ and $Q(t)$ voltages are Gaussian-distributed. An important difference between these time series, however, is that the mixer noise process is not correlated in time. No matter how fast noise voltage samples are collected from the mixer, there is no guarantee that the resulting voltages will be close in magnitude. For a time series of noise power samples the autocorrelation function is essentially zero for all lag times L. Another difference is the probability density function that describes the distribution of averaged noise voltages. The probability density function of an average of N noise power samples is Gaussian-distributed with a standard deviation of $\sigma_v/\sqrt{N}$, as opposed to the more complicated (6.8) which describes the corresponding probability density function for averages of N signal power samples.

The goal now becomes finding the signal power P_{rant} in the noise power P_n. As an illustration, we have produced sets of simulated voltages that are representative of atmospheric return signals (i.e., exponentially distributed) and the mixer noise process and the question becomes can the former be found in the later when they are summed together. The series of illustrations that follow in Figure 16 address just this issue. The voltages illustrated in Figure 16 represent an extreme situation that allows us to demonstrate the power of averaging samples in order to recover a weak atmospheric return signal.

Using a pseudorandom number generator, we generated 100 voltage samples with the correct statistical properties of noise. We squared each voltage sample to obtain the noise power and we then plotted the resulting points as the first 100 samples in Figure 16A1. We then generated another 100 noise power samples as before. This time, however, we also generated 100 "atmospheric" return, or signal, power samples with

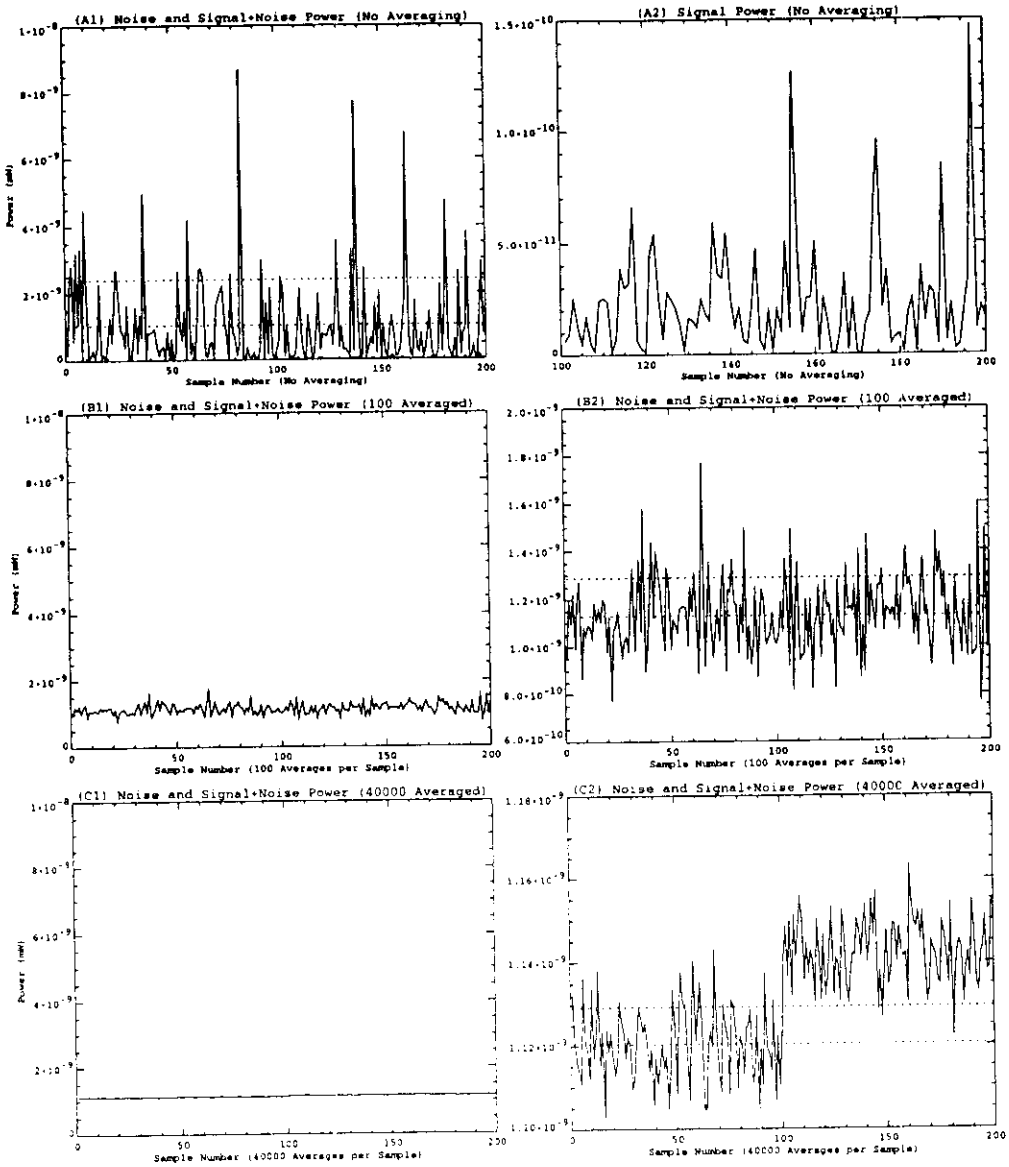

Figure 16. An example of the average power at the output of a radar receiver when 1, 100 and 40 000 instantaneous noise and signal plus noise power samples are averaged. In (A1), (B2) and (C1), the first 100 averaged power samples contain only noise power, whereas the last 100 averaged power samples contain both noise and signal power contributes to the signal. (A2) is a magnification of the signal power samples that we added to the noise power in the last 100 samples of (A1). We plotted these same samples on (A1), but their values were so much lower than the noise power that they are hardly noticeable in (A1). (B2) and (C2) are identical to (B1) and (C1), respectively, except for the scale of the y-axis. The lower dashed line in (A1), (B2) and (C2) is at the level of the mean value of the first 100 points, i.e, at the level of the mean noise, for each figure. The upper dashed line equals the mean of the first 100 samples plus one standard deviation of these same samples.

the correct statistical properties, again using a pseudorandom generator. We added one signal power sample to each noise power sample and plotted the results as samples 101 to 200 in Figure 16A1. Since the signal power levels are small compared to the noise power levels, i.e., look for the second solid line in Figure 16A1, it looks as though nothing has changed from the first 100 samples. The top dashed line in the figure has a power level of 2.4×10^{-9} mW, which we obtained by adding the standard deviation of the first 100 noise power samples to the mean obtained from these same samples. We use this power level to differentiate signal plus noise from noise: everything above the dashed line is considered as signal plus noise, whereas everything below the dashed line is classified as pure noise. Applying this criterion to the series in Figure 16A1 leads to poor results since many of the first 100 power samples are classified as signal plus noise and almost all of the last 100 power samples are identified as noise. To detect the power associated with the signal we must reduce the standard deviation of both the noise and signal plus noise samples; to accomplish this we must average samples.

To this end we generated 10 000 noise power samples as before. We averaged the noise samples in blocks of 100 before plotting them in Figure 16B1. We then generated 10 000 noise power samples, 10 000 signal power samples, added a distinct signal power sample to each noise sample and averaged the summed samples in blocks of 100 to produce samples 101 to 200 in Figure 16B1. In Figure 16B2 we magnify the y-axis to show that we still get poor separation of the signal plus noise from the noise if we use the same criterion as in Figure 16A1.

Finally, we averaged blocks of 40 000 noise samples and signal plus noise samples to produce Figure 16C1. Notice that the standard deviations of both the noise and signal plus noise samples are much reduced compared either to Figure 16A1 or Figure 16B1. More importantly, the magnified plot in Figure 16C2 demonstrates that the criterion for separating noise from signal plus noise performs much better on this data; the number of signal plus noise samples that are identified as noise are greatly reduced from before. Therefore, by averaging more samples the average of the noise samples converges to the actual mean radar noise power and the standard deviation goes to zero. Furthermore, the signal plus noise samples converge on the mean noise power plus the mean signal power also with a vanishing standard deviation. If enough averaging is performed on the samples, the standard deviations become sufficiently small that the "atmospheric" return process is unmasked. We use this standard technique to separate signal plus noise from pure noise when processing the Pennsylvania State University radar data and we use a simple filter on the results in an attempt to remove the type of misclassifications that are illustrated in Figure 16C2 (Clothiaux et al., 1995). Once we have obtained an

estimate of the signal power by subtracting the noise power from the signal plus noise power, we can use the radar equation (2.38) to solve for the reflectivity $\eta(\mathbf{r}_o)$, which is one of the radar observables.

Chapter 7
Doppler Moments

From the $I(t)$ and $Q(t)$ voltages we obtained an estimate of the quantity $\eta(\mathbf{r}_o)$ which provides information about cloud drop locations. $\eta(\mathbf{r}_o)$ also provides information about the particle size distribution, but only through the integral of the backscatter cross section across all particles in the radar resolution volume. We are now at the point where we take the $I(t)$ and $Q(t)$ voltages and manipulate them in order to retrieve information about the motion of the scatterers in the resolution volume. As we illustrate, the power density spectra enables us to better estimate the particles sizes in the resolution volume.

The two techniques that we use are the fast fourier transform (FFT) and the pulse pair autocovariance algorithm. We apply these algorithms to the simulated $I(t)$ and $Q(t)$ time series from Chapter 5 and we then interpret the results in the context of the particle size distribution (Figure 10) and particle fall velocities in (5.8) that we used to generate them in the first place. This discussion is intended to be illustrative and by no means describes which technique works best and under what conditions. For a discussion of these issues, Doviak and Zrnic (DZ, 6.4-6.5) is an excellent starting point.

7.1 Power Density Spectra

Extraction of the power density spectra from the $I(t)$ and $Q(t)$ voltages time series is relatively straightforward (DZ, 5.1). Both the $I(t)$ and $Q(t)$ time series from Section 5 have exactly 4096, or 2^{12}, samples. Since the number of samples is a power of 2, we can use any one of the standard complex FFT algorithms to generate the power density spectra from the time series (e.g., Press et al., 1988, Section 12.2). Using the $I(t)$ and $Q(t)$ time series in Figure 12 as the real and complex array inputs, respectively, to the FFT leads to the power density spectrum S illustrated in Figure 17, where we have transformed the abscissa from frequency to velocity using (5.7). The maximum and minimum velocities in the spectrum are set by the pulse repitition frequency $f_{prf} = 10000\,\mathrm{s}^{-1}$ of the radar. Substituting $\pm f_{prf}$ into (5.7) leads to the range of velocities over which the spectrum is valid. The velocity interval between power density spectral

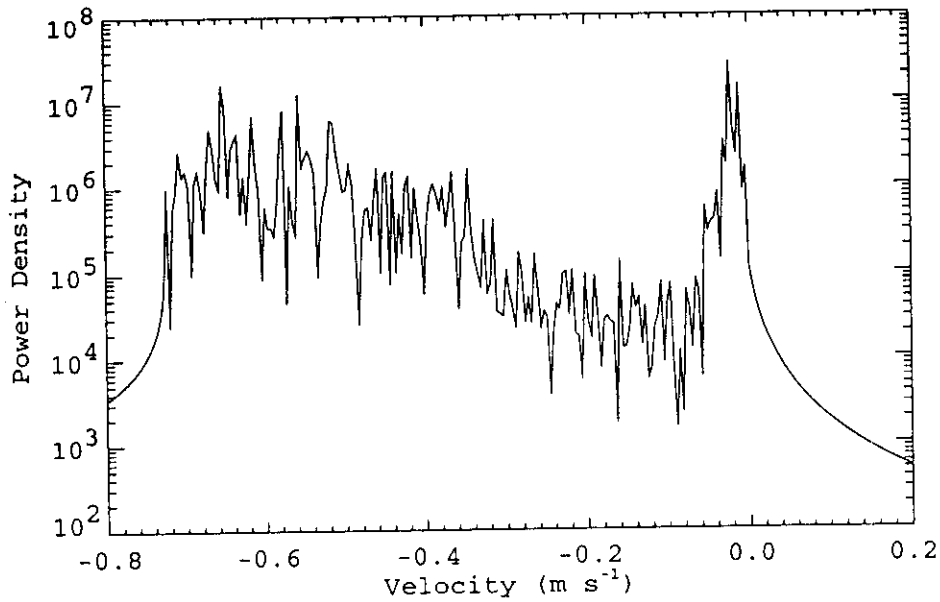

Figure 17. Power density spectrum produced by applying a fast fourier transform, or FFT, to the 4096 I and Q voltages generated in the forward simulation. Negative velocities are downward.

points is set by the number of samples input to the FFT. Since the Pennsylvania State University radar performs a FFT on 512 samples at a time, we broke the $I(t)$ and $Q(t)$ time series into 8 segments of 512, or 2^9, points each. We then performed a FFT on each 512 segment and averaged the resulting 8 power density spectra to produce Figure 18.

The power density $S(m)$ at each velocity $v(m)$ in Figures 17 and 18 is directly related to the total backscattering cross section of all the particles moving with a radial velocity $v(m)$ with respect to the radar. To further illustrate this point, in Figure 19 we plot

$$\sigma(\mathbf{D})\, N(\mathbf{D}, \mathbf{r})\, d\mathbf{D}\, V_{res}, \tag{7.1}$$

where V_{res} is the resolution volume for the drop size distribution illustrated in Figure 10, as a function of the velocity that we obtained from the empirical relation in (5.8). Note that the power density spectra in Figure 18 is a faithful representation of Figure 19. In fact, for this highly idealized simulation, given an accurate radar calibration and the radar equation in (2.38), we can use the power density at each velocity $v(m)$ to directly infer the number density of the drops in the resolution volume whose sizes correspond to the velocity $v(m)$. This kind of argument is often used in current research aimed at retrieving particle size distributions from Doppler radar.

In many cases storing the power density spectra generated by the radar signal processors is beyond the capability of the computers that are running the radar. In these instances the power density spectra are used to calculate estimates of the first

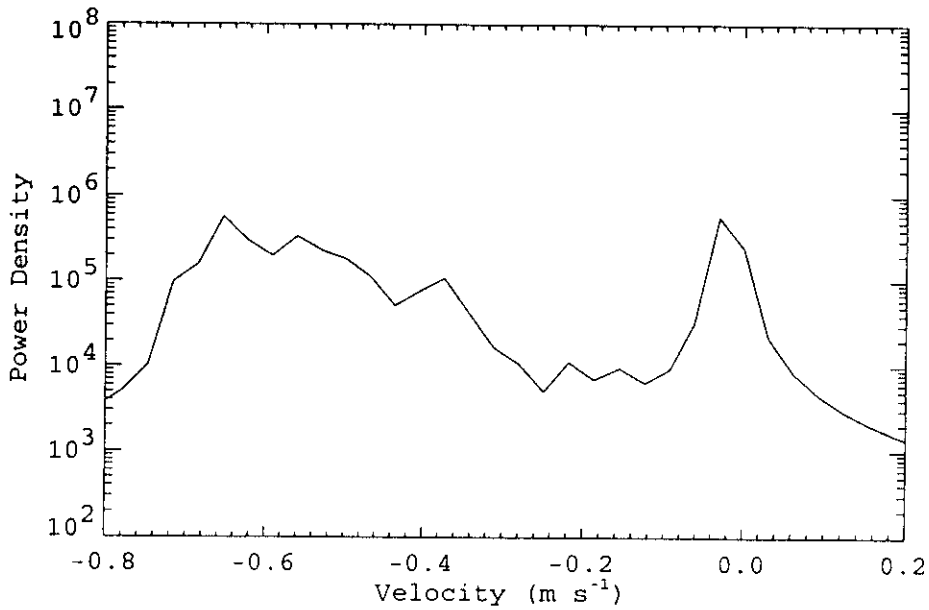

Figure 18. Power density spectrum produced by applying a fast fourier transform, or FFT, to the eight 512 sample blocks of the forward simulation and then averaging the resulting spectra. Negative velocities are downward.

and second moments of the spectra, namely, the mean power-weighted velocity and the spectral width, i.e., the standard deviation of the power-weighted velocities about the mean. The mean power-weighted radial velocity within the resolution volume is defined by (DZ, 5.2)

$$\overline{v} = \sum_{m=-N_n/2}^{N_n/2} v(m) S_n(m) \tag{7.2}$$

and the spectral width σ_v is defined by (DZ, 5.2)

$$\sigma_v^2 = \sum_{m=-N_n/2}^{N_n/2} [v(m) - \overline{v}]^2 S_n(m), \tag{7.3}$$

where $S_n(m)$ is the normalized power density spectra at velocity $v(m)$ (DZ, 5.2), i.e.,

$$S_n(m) = \frac{S(m)}{\sum_{m=-N_n/2}^{N_n/2} S(m)}, \tag{7.4}$$

and the velocity $v(m)$ is given by (DZ, 3.4.3 and 5.1)

$$v(m) = \left(\frac{m}{N_n/2}\right)\left(\frac{\lambda}{4T_s}\right). \tag{7.5}$$

Applying these equations to the spectrum in Figure 17, we obtain a velocity of $-0.419\,\mathrm{ms}^{-1}$ and a spectral width of $0.261\,\mathrm{ms}^{-1}$. These two quantities, together with

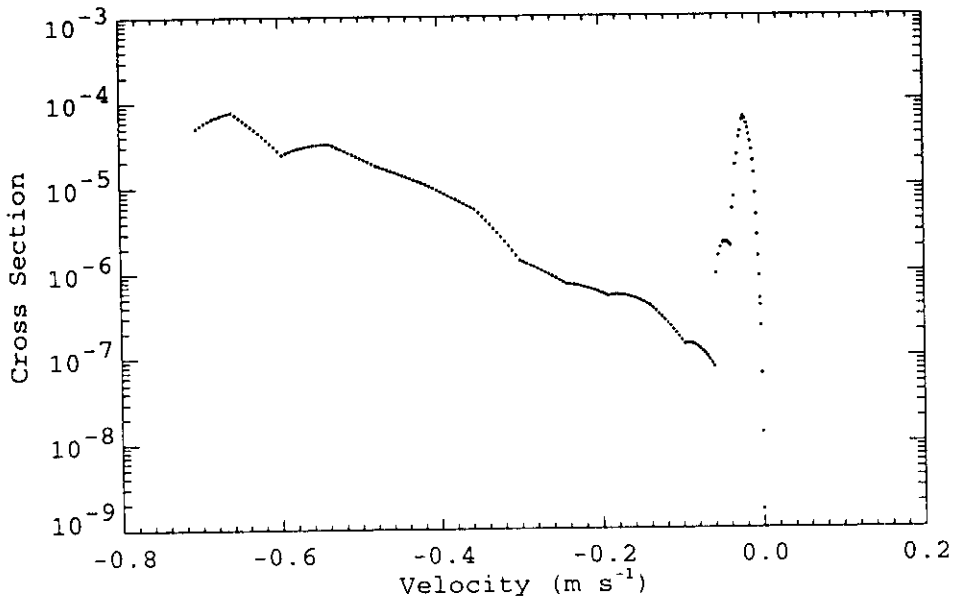

Figure 19. The total backscattering cross section for all of the particles in the radar resolution volume of the forward simulation as a function of particle size plotted against the particle size fall velocity. Negative velocities are downward.

the received power, or zero moment, are the radar observables generally reported at most Doppler radar weather sites.

7.2 Pulse Pair

Performing a FFT on the $I(t)$ and $Q(t)$ time series in an operational setting requires a fast digital signal processing chip with sufficient memory to store and process the data, as well as a fast analog-to-digital convertor that can cover the dynamic range of the radar without introducing any nonlinearities. Since this kind of technology has become available only recently, early investigators in the field of weather-radar research developed methods of producing estimates of the three Doppler moments directly from the $I(t)$ and $Q(t)$ time series. One popular technique that is still in use today is the pulse pair autocovariance technique. A description of the pulse pair algorithm is provided by Doviak and Zrnic (DZ, 6.4-6.5). We simply apply their results to the $I(t)$ and $Q(t)$ time series illustrated in Figure 12 and compare the resulting moments with values derived from the power density spectra. If the complex voltage is

$$V(m) = I(m) + iQ(m) \ (1 \leq m \leq N_n, N_n = 4096), \tag{7.6}$$

then the autocovariance of V at a lag corresponding to the interpulse period $T_s = 1/f_{prf}$ is (DZ, 6.4)

$$\mathcal{R} = \frac{1}{N_n - 1} \sum_{m=1}^{N_s-1} V^*(m)V(m+1). \tag{7.7}$$

$\mathcal{R}$ is a complex number with a real part R_r given by

$$R_r = \frac{1}{N_n - 1} \sum_{m=1}^{N_n-1} [I(m)I(m+1) + Q(m)Q(m+1)] \tag{7.8}$$

and a complex part given by

$$R_c = \frac{1}{N_n - 1} \sum_{m=1}^{N_n-1} [I(m)Q(m+1) - Q(m)I(m+1)]. \tag{7.9}$$

The amplitude of $\mathcal{R}$ is

$$|\mathcal{R}| = \sqrt{R_r^2 + R_c^2} \tag{7.10}$$

and the phase is

$$\phi_{\mathcal{R}} = \tan^{-1}\left(\frac{R_c}{R_r}\right). \tag{7.11}$$

The pulse pair estimate of the mean power-weighted radial velocity of the particles in the resolution volume is (DZ, 6.4)

$$v = -\left(\frac{\lambda}{4\pi T_s}\right)\phi_{\mathcal{R}}, \tag{7.12}$$

where $\phi_{\mathcal{R}}$ is given in radians, and an estimate of the spectral width is (DZ, 6.5)

$$\sigma_v = \left(\frac{\lambda}{2\pi T_s\sqrt{2}}\right)\left|\ln\left(\frac{S}{R}\right)\right|^{1/2} \quad (S > R), \tag{7.13}$$

where (DZ, 6.5)

$$S = \frac{1}{N_n} \sum_{m=1}^{N_n} |V(m)|^2 - P_n \tag{7.14}$$

and P_n is an estimate of the mean radar noise power. Applying (7.12), (7.13) and (7.14) to the simulated $I(t)$ and $Q(t)$ time series produces an estimate of $-0.423\,\mathrm{ms}^{-1}$ for the mean radial velocity and $0.255\,\mathrm{ms}^{-1}$ for the spectral width.

PART 2 - RETRIEVING CLOUD PROPERTIES

Chapter 8
Cloud Properties from Ground-Based Remote Sensing

8.1 A Climate Model Perspective

The preceding sections have described radar wave propagation and signal processing and shown how the measured power return can be related to the properties of the scatterers in the sample volume. In our previous articles (Clothiaux et al., 1995; Syrett et al., 1995) we have shown how millimeter-wave radar can be used to provide a unique and detailed look at clouds, including both their three-dimensional structure and microphysical structure. Quite recently, we and others interested in millimeter-wave radar technology have begun investigating how to translate the radar observations into quantitative data on cloud properties. To some extent, this can be done using the radar alone. However, much more powerful results can be achieved by using the radar observations in combination with observations from other instruments. In this section, we provide an overview of the various techniques being employed. Before discussing these in detail, however, it is useful to consider the data needs from the perspective of the climate community.

As we have demonstrated above, millimeter-wave radar can provide a detailed and unique look at cloud structure, including some aspects of cloud microphysics. It is important, however, that we take the next step of translating this information into quantitative data on cloud properties. Before discussing this process in detail, it is useful to consider from the perspective of the climate community what the data needs are.

One of the major uncertainties in current climate models is the treatment of clouds as embodied in the model parameterizations, and the impact of those clouds on the model radiation fields. Cloud parameterizations vary in their input requirements and output variables but, as a general rule, the output must specify cloud location (height and thickness) and amount of condensed phase (liquid or ice). The latter is then converted in some fashion to an optical depth that can be used as an input to the model radiative codes. More detailed parameterizations also produce information about cloud particle size and the vertical distribution of the condensed phase as outputs. Therefore, for

a given set of parameterization inputs, verification of a parameterization relies on validating the following basic predicted quantities: number of cloud layers, base and top height of each layer, and either the amount of condensed phase or the particle drop size distributions within each layer. Note that if the particle drop size distribution within a layer is known, then the amount of condensed phase can be inferred. Because climate models at best simulate the statistical distribution of these quantities, it is important that we also look at our ability to provide a temporal distribution of these observed properties.

8.2 Models of Cloud Drop Size Distributions

Before describing several techniques proposed in the literature for retrieving water vapor path W_{vp}, liquid water content L_{wc} and path L_{wp} and ice water content I_{wc} and path I_{wp}, as well as the cloud particle number density distribution, it is useful to set forth the notation that is commonly employed in descriptions of the retrievals. For cloud particles let $n(D)\,dD$ represent the number of particles per unit volume with a size between D and $D + dD$, where dD is a small increment in the pertinent dimension of the particles. For spheres D represents the particle diameter, whereas for nonspherical particles D may perhaps represent the maximum dimension or the diameter of a spherical particle that has the same volume as the particle in question. The total number of particles per unit volume becomes

$$N_t = \int_{D_{min}}^{D_{max}} n(D)dD, \tag{8.1}$$

where we have adopted the notation of Flatau et al. (1989). For analytic convenience D_{min} and D_{max} are generally set to 0 and ∞, respectively; the error this appoximation introduces is generally small.

The particle size density function $n(D)$ is usually modelled either by a lognormal distribution or the general modified gamma distribution. These two distributions are useful because they fit the observed distributions of cloud particles and the moments of the distributions can be defined in terms of known functions. The lognormal distribution is defined by

$$n_{log}(D) = \frac{N_t}{\sqrt{2\pi}\sigma D} \exp\Big[-\Big(\frac{\ln(D/D_n)}{\sqrt{2}\sigma}\Big)^2\Big], \tag{8.2}$$

where σ and D_n are parameters. The moments $I_{log}(p)$ of n_{log} are defined by

$$I_{log}(p) = \frac{1}{N_t}\int_0^\infty D^p n_{log}(D)dD = D_n^p F_{log}(p), \tag{8.3}$$

where

$$F_{log}(p) = \exp\Big(\frac{\sigma^2 p^2}{2}\Big). \tag{8.4}$$

The general modified gamma distribution is defined by

$$n_{mg}(D) = \frac{N_t c}{\Gamma(\nu)} \left(\frac{D}{D_n}\right)^{c\nu-1} \frac{1}{D_n} \exp\left[-\left(\frac{D}{D_n}\right)^c\right], \tag{8.5}$$

where $\Gamma(\nu)$ is the complete gamma function and c, ν and D_n are parameters. The moments $I_{mg}(p)$ of the distribution are

$$I_{mg}(p) = \frac{1}{N_t} \int_0^\infty D^p n_{mg}(D) dD = D_n^p F_{mg}(p), \tag{8.6}$$

where

$$F_{mg}(p) = \frac{\Gamma(\nu + p/c)}{\Gamma(\nu)}. \tag{8.7}$$

For a given choice of model, the goal of the retrievals is to determine the model free parameters, together with N_t, as a function of height. The liquid water content L_{wc} and ice water content I_{wc} follow from

$$L(I)_{wc}(z) = \int_0^\infty \rho(D) V(D) n(D) dD, \tag{8.8}$$

where $\rho(D)$ is the density of the particles under consideration and $V(D)$ is the volume of the particles with dimension D. The liquid water path L_{wp} and ice water path I_{wp} follow from integrating the L_{wc} and I_{wc} in a vertical column:

$$L(I)_{wp} = \int_0^\infty L(I)_{wc}(z)\, dz. \tag{8.9}$$

8.3 Cloud Boundaries from Radar Reflectivity

Although detection of cloud location and thickness, hereafter simply referred to as cloud boundaries, from radar seems relatively straightforward, construction of an accurate, reliable algorithm to process large quantities of data is challenging. Since a fairly detailed description of our algorithm is given by Clothiaux et al. (1995), only the principal features are outlined here.

The starting point for any cloud boundary algorithm is a definition of the minimum detectable signal for the radar. This quantity is related to the physical characteristics of the radar, the number of pulses that are being averaged, and the noise power of the signal processing chain. Our current algorithm begins by defining all signals more than one standard deviation above the radar receiver noise as representing a possible significant cloud detection. This threshold includes, however, a significant number of noise events (Figure 20a). We then produce a cloud mask (i.e., a binary two-dimensional image of cloud occurrence in time and height) by smoothing this basic image using a box-car filter in time and space. The presence or absence of a possible significant detection at the 24 "nearest-neighbors" surrounding a particular pixel are used to estimate whether or not that particular pixel is a significant cloud detection. As

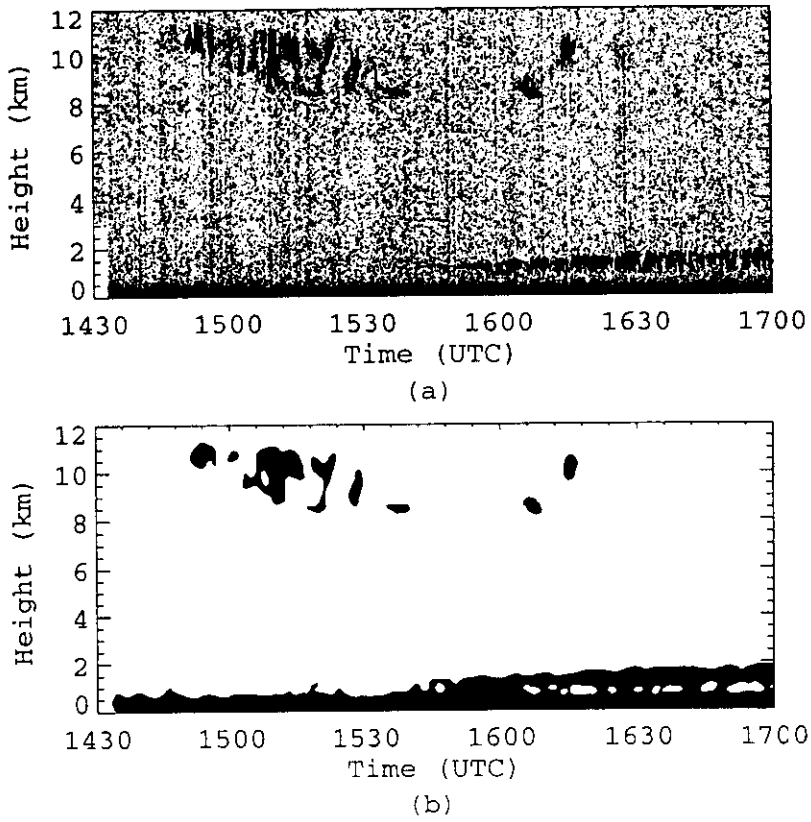

Figure 20. (a) Receiver power output returns greater than one standard deviation above the noise are indicated by the black dots and all other power returns are indicated by white dots. (b) The binary cloud mask image produced by applying a two-dimensional boxcar filter to the image in (a).

Figure 20b demonstrates, our processing removes the noise and produces a contiguous cloud mask which can then be used to identify cloud boundaries in an automated fashion.

An example of cloud statistics generated in this fashion is shown in Figure 21. These data were acquired by the Pennsylvania State University 94-GHz cloud radar during the First ISCCP Regional Experiment, Phase II, (FIRE II) held in Coffeyville, KS, in late 1991 (Uttal et al, 1995). The cloud base histogram (Figure 21a) shows distinct maxima in the upper troposphere around 8 km and in the lower troposphere around 3 km, with a pronounced minima in between. The former are, of course, cirrus clouds, while the latter is a combination of boundary layer and deep convective clouds. Due to the extreme sensitivity of millimeter-wave radar to small particles, they often obtain significant return from boundary layer aerosol, particularly under humid conditions. These radars are even more sensitive to the larger precipitation drops, making it difficult to devise an algorithm that can automatically differentiate between the visual

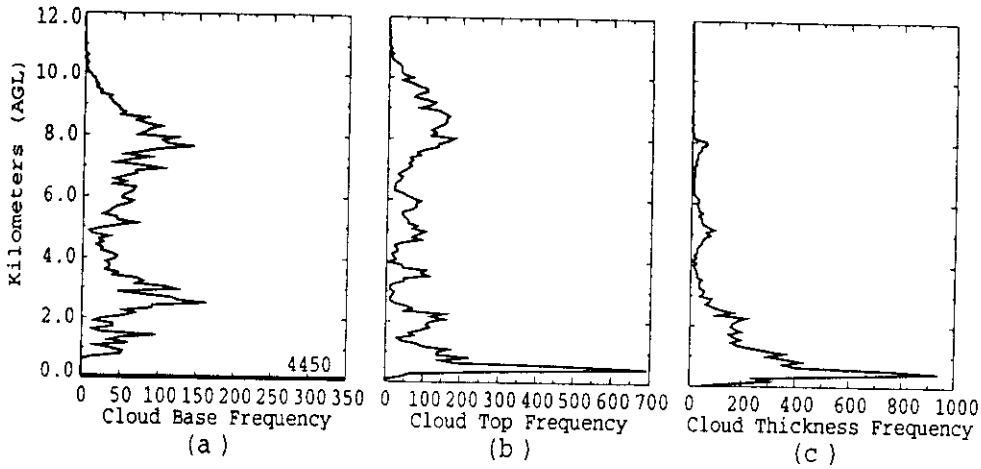

Figure 21. Frequency of occurrence of (a) cloud base height, (b) cloud top height and (c) cloud thickness as recorded by the Pennsylvania State University 94-GHz cloud radar during the FIRE II experiment in Coffeyville, Kansas.

cloud base and the constituents below cloud base. For radiative and microphysical purposes, we generally want to know the visual cloud base, i.e., the base of the cloud droplet distribution, rather than the precipitation base. In our ongoing research we are exploring the use of concurrent ceilometer or lidar cloud base data to identify periods of precipitation, thereby allowing us to correct the radar cloud base statistics so that they contain only information about clouds and not the precipitation emanating from them. Another possibility for inferring the cloud base height in the presence of drizzle is bimodality in the radar Doppler spectra, where one mode corresponds to the cloud particle returns and the other to the drizzle drop signals.

Cloud top heights are generally much easier to infer from radar reflectivity time-height cross sections. The cloud top distribution from FIRE II (Figure 21b) shows a distinct maximum around 9 km with a secondary maxima below about 6 km. The upper maximum is largely cirrus but includes a few occurrences of deep convective clouds.

The cloud base and top data can be differenced to produce frequency distributions of cloud thickness (Figure 21c). These distributions are dominated by cloud thicknesses on the order of 0.5 to 3 km. While we expect this result to be robust, there is some exaggeration of the effect in these histograms because the radar was not operated during periods of the most severe convection. There are cloud thicknesses that span the complete troposphere (9 to 12 km), indicating that some deep convective clouds were sampled.

A unique aspect of cloud radar is its ability to detect multiple cloud layers. Using the cloud mask as a starting point, we can count the number of cloud boundary bottoms

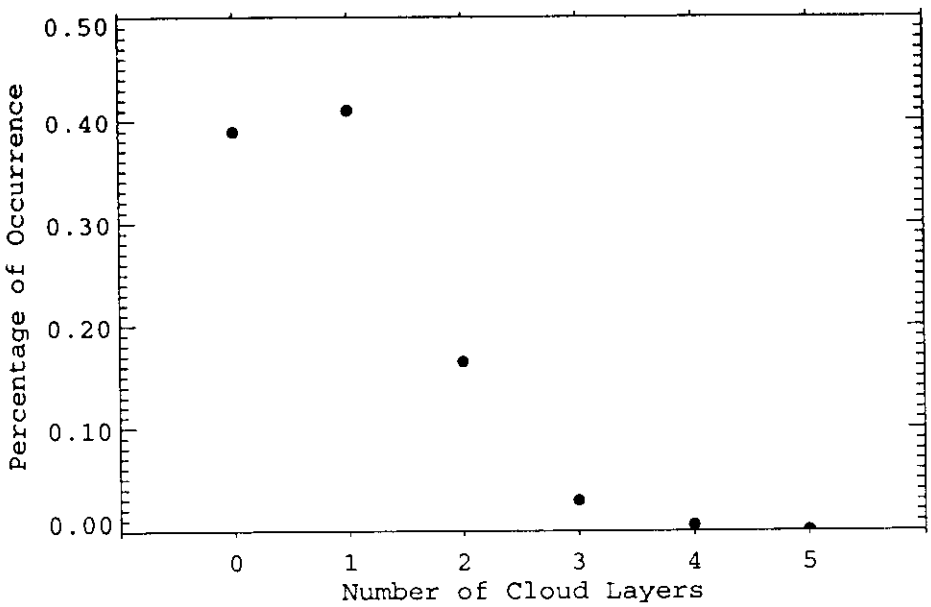

Figure 22. Percentage of occurrence of multiple cloud layers as recorded by the Pennsylvania State University 94-GHz cloud radar during the FIRE II experiment in Coffeyville, Kansas.

and tops profile-by-profile to estimate the frequency of occurrence of multiple cloud layer systems. During the FIRE II experiment, clouds occurred approximately 60 % of the time (Figure 22). (For these statistics, we did not include layers with cloud tops below 800 m in order to avoid confusion with aerosol layers, insects, etc...) When clouds did occur over the radar, they were multilayered 33 % of the time. Using data from two radars, as well as a lidar, Uttal et al. (1995) concluded that during the FIRE II observational period when clouds occurred they had a better than 50 % chance of being multilayered. We conclude that multiplelayered cloud systems are not rare and to accurately estimate their vertical distribution cloud radar is essential.

8.4 Cloud Properties in a Vertical Atmospheric Column

8.4.1 Cloud Liquid Water Path from Passive Radiometry

Given that cloud boundaries can be determined, the most important cloud bulk property that we would like to obtain from our observations is the column amount of condensed water, either the liquid water path L_{wp} or ice water path I_{wp}. Measurement of the condensed liquid water column amount is perhaps most easily inferred from a determination of the atmospheric optical depth at some wavelength, where the optical

depth is defined as

$$\tau_\lambda = \int_0^\infty \sum_{i=1}^{N_a} k_{\lambda,i}(z)\rho_i(z)dz. \tag{8.10}$$

In the definition of τ_λ, N_a is the number of atmospheric constituents radiatively active at the wavelength λ, $k_{\lambda,i}(z)$ is the volume-averaged, wavelength-dependent mass extinction coefficient of the i^{th} species and $\rho_i(z)$ is the density of the i^{th} species. Defining $\overline{k_{\lambda,i}}$ as

$$\overline{k_{\lambda,i}} = \frac{\int_0^\infty k_{\lambda,i}(z)\rho_i(z)dz}{\int_0^\infty \rho_i(z)dz}, \tag{8.11}$$

we can write the equation for τ_λ as

$$\tau_\lambda = \sum_{i=1}^{N_a}\Big[\overline{k_{\lambda,i}}\int_0^\infty \rho_i(z)dz\Big]. \tag{8.12}$$

Now the integral

$$\int_0^\infty \rho_i(z)dz \tag{8.13}$$

is just the column amount of the i^{th} species and is the quantity that we want to infer from measurements of τ_λ. For example, near 24 and 32 GHz, water vapor, cloud liquid water and oxygen are the dominant radiatively active atmospheric constituents. Since the column amount of oxygen is relatively constant in time and space, we can assume its atmospheric optical depth to be the constant $\tau_{\lambda,oxy}$. Therefore, (8.12) becomes

$$\tau_\lambda = \tau_{\lambda,oxy} + \overline{k_{\lambda,v}}\int_0^\infty \rho_v(z)dz + \overline{k_{\lambda,l}}\int_0^\infty \rho_l(z)dz, \tag{8.14}$$

where $\rho_v(z)$ and $\rho_l(z)$ are the vertical density profiles of water vapor and cloud liquid water, respectively. The two integrals on the right hand side of the above equation are simply the water vapor path W_{vp} and the liquid water path L_{wp}, respectively. Since we have measurements at two frequencies, we have two optical depth equations in two unknowns, assuming that $\overline{k_{\lambda,v}}$ and $\overline{k_{\lambda,l}}$ are known, which can be inverted to yield W_{vp} and L_{wp}. Importantly, the inversion is well-behaved because the total optical depths at the two frequencies have different dependencies on the water vapor and cloud liquid water column amounts. Furthermore, the retrieved W_{vp} and L_{wp} are not seriously affected by the presence of ice particles in the atmosphere since ice water is not radiatively active at these two wavelengths.

8.4.2 Cloud Liquid and Ice Water Content from Radar Reflectivity

In an alternative approach using only radar reflectivities Liao and Sassen (1994) theoretically compute the radar reflectivity Z and liquid water content L_{wc} for liquid water drop distributions generated in an adiabatic cloud model. Performing a regression of the liquid water content versus the radar reflectivity for distributions generated with a number of different cloud model parameters, Liao and Sassen (1994) arrived at the relationship

$$L_{wc} = 0.49(N_t Z)^{0.55}, \tag{8.15}$$

where N_t is the total number of drops per unit volume and depends upon the initial number of cloud condensation nuclei in the cloud model simulation. Liao and Sassen (1994) performed a similar regression analysis of the ice water content versus radar reflectivity using a number of different *in situ* observations by aircraft with the result that

$$I_{wc} = 7.49 Z_e^{0.78}. \tag{8.16}$$

Liao and Sassen (1994) found their empirically derived relationships to be consistent with the results of a number of earlier investigations that adopted a similar approach.

8.4.3 Cloud Drop Size Distributions from Passive Radiometry and Radar Reflectivity

Matrosov et al. (1992) combine a measurement of brightness temperature between 10 and 12 μm and particle radar reflectivity at 9.3 GHz to infer the average particle concentration N_t and the average scaling diameter D_n across the depth of an ice cloud layer. (Actually, Matrosov et al. (1992) retrieve a diameter D_m that splits the cirrus cloud particle distribution into two equal volumes of cloud drops, as opposed to the scaling diameter D_n of a modified gamma distribution.) Their strategy consists of using the measured brightness temperature, or radiance, to infer the cloud optical depth. From the cloud optical depth they are in turn able to solve for the product $N_t D_n^2$. The reflectivity obtained from the radar then allows them to solve for N_t and D_n individually.

Consider the case of a vertically and horizontally homogeneous cirrus cloud layer with no underlying water clouds. Using a two-stream radiative transfer model in the cloud layer and ignoring any sources of radiation above the cloud layer, Matrosov et al. (1992) derive a simple parameterization for the nadir directed radiance $I_{cb}^{\downarrow}$ at the base of the cloud layer:

$$I_{cb}^{\downarrow} = B(T_{cb})\left[1 - \exp(-a_o \tau^0)\right], \tag{8.17}$$

where $B(T_{cb})$ is the blackbody radiance for a physical temperature T_{cb} at the base of the cloud layer, τ^0 is the optical depth of the cloud layer and a_o (= 0.7) is a free parameter used to achieve the best prediction of $I^{\downarrow}_{cb}$ from $B(T_{cb})$ and τ^0 for a number of forward two-stream model calculations using a range of values both for the cloud optical thickness and the particle size distribution parameters N_t and D_n. To infer $I^{\downarrow}_{cb}$ from measured radiances $I^{\downarrow}_{m}$ one must know the atmospheric transmittance $\mathcal{T}_a$ between cloud base and the surface:

$$I^{\downarrow}_{cb} = [I^{\downarrow}_{m} - B(T_{mr})(1 - \mathcal{T}_a)]/\mathcal{T}_a, \tag{8.18}$$

where $B(T_{mr})$ is the blackbody radiance of the subcloud atmosphere with a mean temperature T_{mr} and $I^{\downarrow}_{m}$ is the radiance measured by the instrument. Therefore, with knowledge of $\mathcal{T}_a$, T_{mr} and T_{cb}, which can be estimated from radiosonde profiles, the measured radiance $I^{\downarrow}_{m}$ can be inverted to optical thickness τ^0.

For a vertically and horizontally homogeneous cloud layer the optical depth of the cloud layer is

$$\tau_\lambda = \Big[\int_0^\infty Q_{ext}(D)\pi\Big(\frac{D}{2}\Big)^2 n_{mg}(D)dD\Big]H_c, \tag{8.19}$$

where $Q_{ext}(D)$ is the extinction efficiency of the cloud particles with size dimension D and H_c is the cloud layer thickness. Assuming that most cirrus ice particles are larger than 10 to 12 μm, $Q_{ext}(D) \approx 2$ and τ_λ becomes

$$\tau_\lambda = \Big[\frac{\pi}{2}\int_0^\infty D^2 n_{mg}(D)dD\Big]H_c. \tag{8.20}$$

Using the moments equation (8.6) with $c = 1$ and $\nu = 2$, which Matrosov et al. (1992) argue is adequate for most cirrus cloud particle distributions, τ_λ becomes

$$\tau_\lambda = 3\pi N_t D_n^2 H_c. \tag{8.21}$$

Therefore, with a zenith directed radiance measurement one can infer the value of the product $N_t D_n^2$. Now the radar reflectivity Z is defined by

$$Z = \int_0^\infty D^6 n_{mg}(D)dD, \tag{8.22}$$

or

$$Z = 2016 N_t D_n^6, \tag{8.23}$$

where we have used (8.6). Since there are now two equations, i.e., (8.21) and (8.23), we can solve for the two unknowns N_t and D_n. If the cloud layer is not vertically homogeneous, Matrosov et al. (1992) replace Z in (8.23) with the average value of Z from the top to the bottom of the cloud layer.

8.4.4 Cloud Drop Size Distributions from Passive Radiometry, Radar Reflectivity and Radar Velocity

In order retrieve N_t and D_n as a function of height within a cirrus cloud layer, and thereby allow the I_{wc} to vary with height within the cloud, Matrosov et al. (1994) developed a retrieval algorithm combining a measurement of the brightness temperature, or radiance, between 10 and 12 μm with radar measurements of the particle reflectivity and Doppler velocity as a function of height within the cloud layer. As before, Matrosov et al. (1994) assume that $c = 1$ and they demonstrate that the retrievals are not extremely sensitive to the value of ν so we set $\nu = 2$. For a vertically inhomogeneous cloud layer the optical depth defined in (8.19) becomes

$$\tau_\lambda = \sum_{j=1}^{N_g} \Big\{ \Big[\int_0^\infty Q_{ext}(D) \pi \Big(\frac{D}{2}\Big)^2 n_{mg}(D) dD \Big] H_{c,j} \Big\}, \tag{8.24}$$

where $H_{c,j}$ is now the radar resolution volume spacing and N_g is the number of radar resolution volumes in the cloud layer. Note that the number of range gates with cloud return can be obtained from the location of the cloud boundaries. Again assuming that $Q_{ext}(D) \approx 2$ for all D, the optical depth becomes

$$\tau_\lambda = \sum_{j=1}^{N_g} \Big\{ 2016 \pi N_{t,j} D_{n,j}^6 H_{c,j} \Big\}. \tag{8.25}$$

The measured optical depth $\tau_{m,ir}$ is inferred from the infrared window measurements of sky brightness temperature using (8.17).

As before, the radar reflectivity is defined by (8.23), where N_t and D_n are now a function of height, i.e., $N_{t,j}$ and $D_{n,j}$, respectively. The reflectivity-weighted mean Doppler velocity due to all of the particles in a radar resolution volume is

$$V_{f,j} = \frac{\int_0^\infty v_f(D) D^6 n_{mg}(D) dD}{\int_0^\infty D^6 n_{mg}(D) dD}. \tag{8.26}$$

Based on Pruppacher and Klett (1978), Matrosov et al. (1994) assume that the fall speed of the particles are related to the diameter by

$$v_f(D) = A D^B, \tag{8.27}$$

where A and B are constants that depend upon the crystal shape. Substituting (8.27) into (8.26) and using (8.6) yields

$$V_{f,j} = A \Big[\frac{\Gamma(\nu + B + 6)}{\Gamma(\nu + 6)} \Big] D_{n,j}^B, \tag{8.28}$$

where air density and viscosity effects have been neglected.

At this point $2N_g + 2$ unknowns have entered into the set of equations, i.e., $N_{t,j}$ and $D_{n,j}$, where $j = 1, .., N_g$, A and B. However, there are only $2N_g + 1$ measurements

consisting of Z_j and $V_{f,j}$, where $j = 1, .., N_g$, and $\tau_{m,ir}$. Since the variation of B is relatively small, i.e., 0.75 to 1.4, Matrosov et al. (1994) set $B = 1$. Picking an initial value of A_o for A, Matrosov et al. (1994) solve (8.23) and (8.28) for $N_{t,j}$ and $D_{n,j}$ at each range gate. Computing the infrared window optical depth τ_{ir} from (8.25) and comparing the result with the measured optical depth $\tau_{m,ir}$, they are able to derive a new value for A, i.e.,

$$A = A_o\Big(\frac{\tau_{m,ir}}{\tau_{ir}}\Big)^{B/4}, \tag{8.29}$$

such that when (8.25) is recomputed with the this value of A and the existing values of $N_{j,t}$ and $D_{j,t}$, the measured optical depth $\tau_{m,ir}$ results. Using A from (8.29) to solve (8.23) and (8.28) for $N_{t,j}$ and $D_{n,j}$, Matrosov et al. (1994) arrive at their final estimates of the particle concentration and scaling diameter as a function of height within the cloud layer. The ice water contents I_{wc} and the ice water path I_{wp} follow immediately from (8.8) and (8.9), respectively.

For the retrievals to work, the reflectivity-weighted mean Doppler velocity $V_{f,j}$ must represent the fall velocities of the particles in the air with no vertical motion. Since there are generally updrafts and downdrafts within a cloud, the raw radar derived value of $V_{f,j}$ cannot be used in (8.28). Based on work by Orr and Kropfli (1993), Matrosov et al. (1994) circumvent this problem by averaging over several hours all of the Doppler velocities $V_{f,j}$ at each resolution volume whose corresponding reflectivities fall within a narrow reflectivity bin. If the reflectivity value is indicative of a specific particle distribution within the radar resolution volume and if the average vertical motion of the air over the averaging interval is near zero, then the average velocity generated for each reflectivity bin of each resolution volume corresponds to the vertical fall speed of the particles in still air at the resolution volume location. Therefore, the reflectivity observed for each resolution volume is used as an index into the reflectivity bins from which an estimate of the average, still air particle fall speed is recovered.

8.4.5 Cloud Drop Size Distributions from the First Three Radar Doppler Moments

Frisch et al. (1995) utilize the first three spectral moments, i.e., reflectivity, Doppler velocity and Doppler width, to retrieve the particle size distributions in light drizzle and stratus clouds with no drizzle. For both of these conditions, Frisch et al. (1995) assume that a lognormal distribution is an adequate model. Therefore, their retrieval amounts to inferring the particle number density N_t, scaling diameter D_n and distribution width σ, of a lognormal distribution from the three Doppler moments.

For a lognormal distribution the reflectivity Z_j is defined by

$$Z_j = \int_0^\infty D^6 n_{\log,j}(D) dD = N_{t,j} D_{n,j}^6 e^{18\sigma_j^2}, \tag{8.30}$$

where j represents a particular resolution volume. Based on Gossard et al. (1990), Frisch et al. (1995) assume a linear relationship between the drizzle-particle fall speed v_f and the particle diameter D:

$$v_f(D) = \frac{D-b}{a}, \tag{8.31}$$

where $a = 2.4 \times 10^{-4}$s and $b = 2.0 \times 10^{-5}$m. Therefore, the first Doppler moment $V_{f,j}$ is

$$V_{f,j} = \frac{\int_0^\infty [(D-b)/a] D^6 n_{\log,j}(D) dD}{\int_0^\infty D^6 n_{\log,j}(D) dD} = \left(\frac{D_{n,j}}{a}\right) e^{13\sigma_j^2/2} - \frac{b}{a}, \tag{8.32}$$

while the second Doppler moment W_j is defined by

$$W_j = \frac{\int_0^\infty [(D-b)/a - V_{f,j}] D^6 n_{\log,j}(D) dD}{\int_0^\infty D^6 n_{\log,j}(D) dD} = \left(\frac{D_{n,j}}{a}\right)^2 e^{13\sigma_j^2} \left(e^{\sigma_j^2} - 1\right). \tag{8.33}$$

Solving for $\exp(13\sigma_j^2)$ in (8.32) and substituting the result into (8.33), one has

$$\sigma_j = \left\{\ln[1 + W_j/(V_{f,j} + b/a)]\right\}^{1/2}. \tag{8.34}$$

For drizzle either below cloud base or within a cloud of a negligible reflectivity, Z_j, $V_{f,j}$ and W_j are due to properties of the drizzle. Therefore, we have three unknowns, i.e., $N_{t,j}$, $D_{n,j}$ and σ_j, and three equations, i.e., (8.30), (8.32) and (8.33), with which to solve for them. From (8.34) one can solve for σ_j. Using the retrieved value of σ_j and (8.33), one can then solve for $D_{n,j}$. Finally, one can solve for $N_{t,j}$ by substituting the retrieved values of σ_j and $D_{n,j}$ into (8.30).

For stratus clouds that consist of small drops and no drizzle, only the measurement of Z_j produces useful information about the cloud drops. In this case, $V_{f,j}$ and W_j are due to the mean vertical air motion and turbulence, respectively, since the small drops are presumably moving with the air. Therefore, we now have N_g useful measurements, i.e., Z_j for $j = 1, .., N_g$, where N_g is the number of radar resolution volumes providing significant returns from the cloud drops. To reduce the number of unknowns, Frisch et al. (1995) assume that $\sigma_j = \sigma = 0.35$ for all j, $N_{t,j} = N_t$ for all j with N_t unknown, and $D_{n,j}$ is unknown and changes from one resolution volume to the next. All together we now have $N_g + 1$ unknowns. To have a well-constrained retrieval of $D_{n,j}$ and N_t one additional measurement is needed; therefore, Frisch et al. (1995) assume that the liquid water path L_{wp} is measured as well.

For this situation the reflectivity becomes

$$Z_j = N_t D_{n,j} e^{18\sigma^2}, \tag{8.35}$$

where N_t is a constant and $\sigma = 0.35$. To solve for $D_{n,j}$ in (8.35) one must know N_t, which can be estimated from the measured L_{wp}. The liquid water content $L_{wc,j}$ at the j^{th} resolution volume is

$$L_{wc,j} = \int_0^\infty \rho_w \Big[\frac{4}{3}\pi\Big(\frac{D}{2}\Big)^3\Big] n_{\log j}(D) dD = \Big(\frac{\pi \rho_w N_t}{6}\Big) D_{n,j}^3 e^{9\sigma^2/2}. \tag{8.36}$$

Solving for $D_{n,j}$ in (8.35) and substituting the result into (8.36) yields

$$L_{wc,j} = \Big(\frac{\pi \rho_w N_t}{6}\Big)\Big[Z_j^{1/2} N_t^{-1/2} e^{-18\sigma^2/2}\Big] e^{9\sigma^2/2}. \tag{8.37}$$

Integrating the liquid water content over the depth of the cloud layer, we have the liquid water path L_{wp}:

$$L_{wp} = \sum_{j=1}^{N_g} L_{wc,j} H_{c,j} = \Big(\frac{\pi \rho_w}{6}\Big) N_t^{1/2} e^{-9\sigma^2/2} \Big(\sum_{j=1}^{N_g} Z_j^{1/2}\Big) H_{c,j}. \tag{8.38}$$

Substituting the measured L_{wp} and radar reflectivities Z_j into (8.38), one can solve for N_t. Once N_t is in hand, $D_{n,j}$ can be obtained from (8.35) and the $L_{wc,j}$ from (8.36).

8.4.6 Cloud Drop Size Distributions from Radar Doppler Spectra

Gossard (1994) presents a technique that uses the entire Doppler spectrum in a retrieval of the cloud drop size distribution. The innovation in Gossard's retrieval is that the effects of turbulence and any mean vertical wind motion within the radar resolution volume on the Doppler spectrum are explicity accounted for in the retrieval. Assuming that the radar wavelength is much larger than the cloud drops, the density of the reflectivity Z as a function of diameter D, i.e., the integrand of (8.22), is

$$S_z^q(D) = n_{mg}(D) D^6, \tag{8.39}$$

where the superscript q indicates that turbulence is not included in the definition of $S_z^q(D)$. In Figure 23a we plot $n_{mg}(D)$ and $S_z^q(D)$ for gamma distribution parameters $N_t = 6.54 \times 10^6\,\mathrm{m}^{-3}$, $\nu = 1$, and $D_n = 0.0233\,\mathrm{mm}$. Since ν is one, the drop size distribution in Figure 23a is exponential. The choice of $D_n = 0.0233\,\mathrm{mm}$ forces the maximum value of $S_z^q(D)$ in Figure 23a to occur at $D_m = 0.14\,\mathrm{mm}$ since the modal value of $S_z^q(D)$ occurs at $D_m = D_n(6+\nu-1)$. Changing variables in (8.39) from the drop diameter D to the drop fall speed v, where we assume a known relationship $D = D(v)$, we have

$$S_z^q(v) = S_z^q(D(v)) \frac{dD}{dv}(v). \tag{8.40}$$

For the spectrum $S_z^q(D)$ in Figure 23a, the corresponding fall velocity spectrum $S_z^q(v)$ is illustrated in Figure 23b, where we use (Rogers et al., 1993)

$$v(D) = 4\Big(\frac{\rho}{\rho_o}\Big)^{-0.5} D\,(1 - e^{-12D}). \tag{8.41}$$

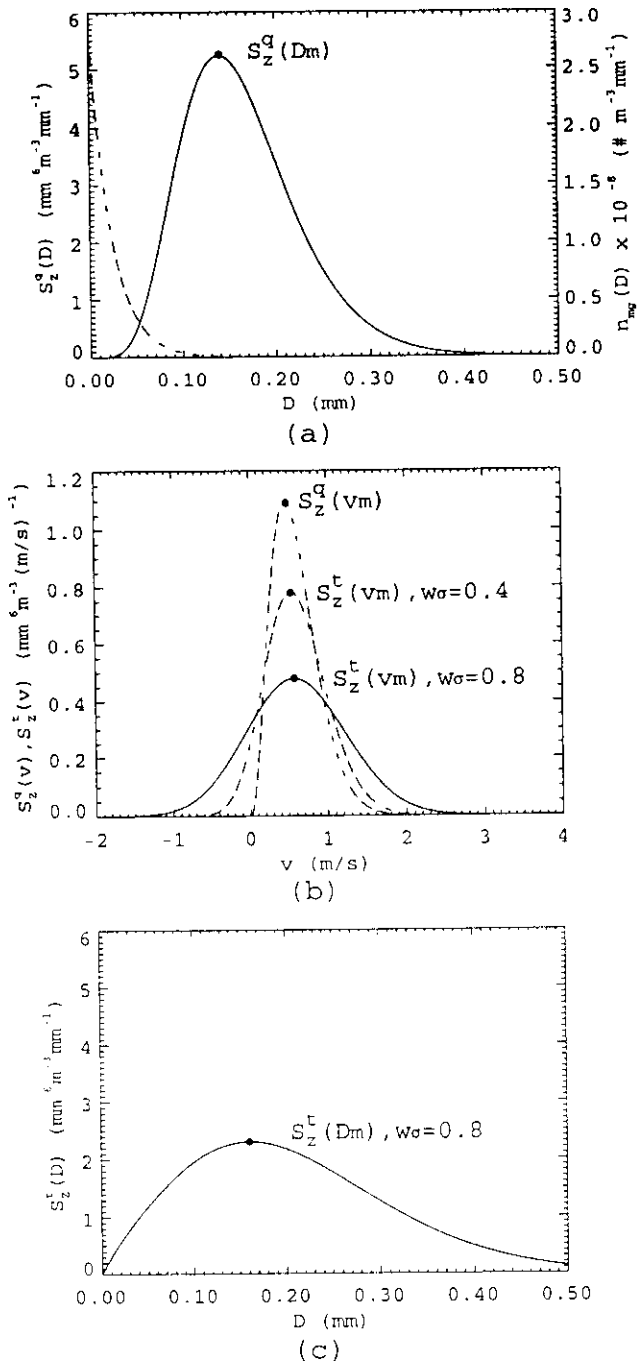

Figure 23. (a) Cloud drop number density $n_{mg}(D)$ (dashed line) and reflectivity density $S_z^q(D)$ (solid line) for gamma distribution parameters $N_t = 6.5 \times 10^6 \mathrm{m}^{-3}$, $D_n = 0.233\mathrm{mm}$ and $\nu = 1$. (b) Reflectivity density versus drop fall velocity for no turbulence (upper dashed line), turbulence with $v_\sigma = w_\sigma = 0.4$ (lower dashed line) and turbulence with $v_\sigma = w_\sigma = 0.8$ (solid line). Positive velocities are downward. (c) Reflectivity density $S_z^t(D)$ that results from changing variables in $S_z^t(v)$ from drop fall velocity v to drop diameter D.

Again, the superscript q in $S_z^q(v)$ indicates a quiet air spectrum with particle fall velocities that are not affected by turbulence. If turbulence is present, then the spectrum $S_z^q(v)$ must be convolved with the turbulence spectrum to produce the final spectrum $S_z^t(v)$:

$$S_z^t(v) = \int_0^\infty S_z^q(v') \frac{1}{\sqrt{\pi v_\sigma^2}} e^{-[(v'-v)/v_\sigma]^2} dv', \tag{8.42}$$

where, like Gossard (1994), we have assumed Gaussian turbulence. The results of such a convolution are illustrated in Figure 23b for v_σ equal to 0.4 and 0.8. Apart from mean vertical wind motions within the radar resolution volume, which shifts the spectra in Figure 23b either to the left or right, $S_z^t(v)$ corresponds to the observed radar Doppler spectrum and is one of the outputs of a cloud radar. Gossard's technique attempts to retrieve the parameters N_t and D_n given spectra $S_z^t(v)$ that are potentially influenced by turbulence and mean vertical air motion within the radar resolution volume.

If one simply changes variables in $S_z^t(v)$ from v to D, i.e.,

$$S_z^t(D) = S_z^t(v(D)) \frac{dv}{dD}(D), \tag{8.43}$$

the resulting spectrum may look nothing like the original spectrum (Figure 23c) because of the effects of turbulence and perhaps a mean vertical wind within the radar resolution volume. Obviously, any drop size retrievals based solely on the spectrum $S_z^t(D)$ will contain serious errors. Note, however, that the ratio of the peak of $S_z^q(D)$ (e.g., Figure 23a) to the peak of $S_z^t(D)$ (e.g., Figure 23c) is a function only of the turbulent width v_σ and the modal diameter D_m and can be calculated for all possible combinations of these two parameters, just as we have done to generate the three panels in Figure 23. This fact motivates Gossard (1994) to define the deconvolution factor DF as the ratio

$$DF = DF(D_m, v_\sigma) = S_z^q(D_m) \,/\, \Big[S_z^t(v_m) \frac{dv}{dD}(D_m)\Big], \tag{8.44}$$

where v_m is the modal value of the spectrum $S_z^t(v)$ (e.g., the peak of the solid line in Figure 23b) and the factor $S_Z^t(v_m)[dv/dD(D_m)]$ is an estimate for the mode of $S_z^t(D_m)$ (e.g., the peak of $S_z^t(D)$ in Figure 23c). We are now in a position to illustrate the basic equation that Gossard uses to retrieve the modal diameter D_m of $S_z^q(D)$.

The reflectivity factor defined in (8.22) can be integrated with the aid of (8.6) yielding

$$Z = N_t \Big(\frac{D_m}{6+\alpha}\Big)^6 \frac{(\alpha+6)!}{\alpha!}, \tag{8.45}$$

where we let $\alpha = \nu - 1$ in accordance with Gossard (1994). Rearranging factors, Gossard writes Z as

$$Z = S_z^q(D_m)\, f(\alpha)\, D_m, \tag{8.46}$$

where the modal value of $S_z^q(D)$ is

$$S_z^q(D_m) = \frac{N_t\,(\alpha+6)^{(1+\alpha)}\,e^{-(6+\alpha)}\,D_m^6}{\alpha!\,D_m} \tag{8.47}$$

and

$$f(\alpha) = \frac{(\alpha+6)!\,e^{(6+\alpha)}}{(\alpha+6)^{(7+\alpha)}}. \tag{8.48}$$

Solving for $S_z^q(D_m)$ in (8.44) and using (8.45), (8.46) and (8.47) gives

$$D_m - Z/\Big[f(\alpha)\,S_z^t(v_m)\,\frac{dv}{dD}(D_m)\,DF(D_m, v_\sigma)\Big] = 0. \tag{8.49}$$

The reflectivity Z and mode $S_z^t(v_m)$ of the Doppler spectra are radar observables. If we assume a value for α, e.g., zero, one or two, then the only two unknowns in (8.49) are D_m and v_σ. As Gossard demonstrates, the part of the peak in $S_z^t(v)$ with negative Doppler velocities, i.e., particles moving upwards and away from the radar, is a function of the turbulent width v_σ; hence, the width v_σ can be recovered by fitting a Gaussian function to this region of the spectrum. Once an estimate of v_σ is in hand, one can numerically solve (8.49) for D_m. Given D_m and Z, N_t follows from (8.45), (8.46), (8.47) and (8.49). Note that the value of v_m does not explicitly enter into the retrieval; consequently, updrafts and downdrafts within the radar resolution volume do not affect the outcome of the retrieval.

Chapter 9
Concluding Remarks

Millimeter-wave radar is proving to be a tremendously useful tool for the study of cloud properties. A number of papers have demonstrated the usefulness of radar reflectivity measurements for qualitative studies of cloud behavior, as well as quantitative determinations of cloud boundaries. However, the real power of radar lies in combining reflectivity and Doppler velocity measurements with lidar cloud base and passive radiometric measurements. Radiometric measurements typically provide integral measurements of total condensed phase. By using these as constraints on cloud particle retrievals from the active sensors, we can devise methods that allow us to define the vertical distribution of cloud particle size and condensed water content. This is a remarkable achievement. Further, the instruments currently being developed are much more robust than their earlier counterparts. Millimeter-wave radar and small lidar systems can be run continuously and unattended, as can passive radiometers. Various investigators have demonstrated this capability with individual instruments, and now the Atmospheric Radiation Measurement (ARM) program, sponsored by the United States Department of Energy, is putting instruments systems together for long term operations.

Given this progress, development of routine signal processing techniques for radars and retrieval algorithms for instrument systems must be viewed as high priority research. Much like satellites provide measurements of spatial variability, these suites of ground-based instruments can be used to continuously measure cloud statistics, provided that algorithms are available to process the raw data streams. These statistics will have many uses, including model verification and satellite retrieval validation. Most importantly, the unique perspective on cloud properties provided by these retrievals and statistics will improve our understanding of cloud physics and cloud processes.

References

Atlas, D., Ed., 1990: *Radar in Meteorology.* American Meteorological Society, Boston, Massachusetts.

Battan, L.J., 1973: *Radar Observation of the Atmosphere.* University of Chicago Press, Chicago, Illinois.

Bohren, C.F., and D.R. Huffman, 1983: *Absorption and Scattering of Light by Small Particles.* John Wiley and Sons, New York, New York.

Clothiaux, E.E., M.A. Miller, B.A. Albrecht, T.P. Ackerman, J. Verlinde, D.M. Babb, R.M. Peters and W.J. Syrett, 1995: An evaluation of a 94-GHz radar for remote sensing of cloud properties. *J. Atmos. Oceanic Technol.*, **12**, 201-229.

Doviak, R.J., and D.S. Zrnić, 1984: *Doppler Radar and Weather Observations.* Academic Press, San Diego, California.

Doviak, R.J., and D.S. Zrnić, 1993: *Doppler Radar and Weather Observations.* Second Edition. Academic Press, San Diego, California.

Flatau, P.J., G.J. Tripoli, J. Verlinde and W.R. Cotton, 1989: *The CSU-RAMS Cloud Microphysics Module: General Theory and Documentation.* Paper No. 451, Colorado State University, Department of Atmospheric Science, Fort Collins, Colorado.

Frisch, A.S., C.W. Fairall, and J.B. Snider, 1995: Measurement of stratus cloud and drizzle parameters in ASTEX with a Ka-band doppler radar and a microwave radiometer. *J. Atmos. Sci.*, **52**(16), 2788-2799.

Gossard, E.E., R.G. Strauch, and R.R. Rogers, 1990: Evolution of drop-size distributions in liquid precipitation observed by ground-based Doppler radar. *J. Atmos. Oceanic Technol.*, **7**, 815-828.

Gossard, E.E., 1994: Measurement of cloud droplet size spectra by doppler radar. *J. Atmos. Oceanic Technol.*, **11**, 712-726.

Liao, L., and K. Sassen, 1994: Investigation of relationships between Ka-band radar reflectivity and ice and liquid water contents. *Atmos. Res.*, **34**, 231-248.

Marshall, J.S., and W. Hitschfeld, 1953: Interpretation of the fluctuating echo from randomly distributed scatterers. *Can. J. Phys.*, **31**(1), 962-995.

Matrosov, S.Y., T. Uttal, J.B. Snider, and R.A. Kropfli, 1992: Estimation of ice cloud parameters from ground-based infrared radiometer and radar measurements. *J. Geophy. Res.*, **97**(D11), 11567-11574.

Matrosov, S.Y., B.W. Orr, R.A. Kropfli, and J.B. Snider, 1994: Retrieval of vertical profiles of cirrus cloud microphysical parameters from doppler radar and infrared radiometer measurements. *J. Appl. Meteor.*, **33**, 617-626.

Orr, B.W. and R.A. Kropfli, 1993: Estimation of cirrus particle fallspeeds from vertically pointing Doppler radar. Preprints, *26th Int. Conf. on Radar Meteorology*, Norman, OK, Amer. Meteor. Soc., 588-590.

Press, W.H., B.P. Flannery, S.A. Teukolsky and W.T. Vetterling, 1988: *Numerical Recipes in C.* Cambridge University Press, Cambridge, England.

Pruppacher, H.R., and J.D. Klett, 1978: *Microphysics of Clouds and Precipitation.* D. Reidel, Boston, Massachusetts.

Reitz, J.R., F.J. Milford and R.W. Christy, 1979: *Foundations of Electromagnetic Theory.* Third Edition. Addison-Wesley, Reading, Massachusetts.

Rogers, R.R., D. Baumgardner, S.A. Ethier, D.A. Carter and W.L. Ecklund, 1993: Comparison of raindrop size distributions measured by radar wind profiler and by airplane. *J. Appl. Meteor.*, **32**, 694-699.

Sauvageot, H., 1992: *Radar Meteorology.* Artech House, Inc., Norwood, Massachussetts.

Syrett, W.J., B.A. Albrecht and E.E. Clothiaux, 1995: Vertical cloud structure in a midlatitude cyclone from a 94-GHz radar. Monthly Weather Review, Accepted.

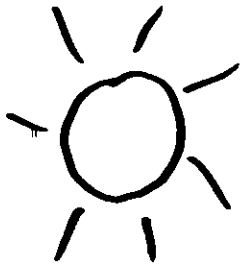

SCIENCE GOALS:

CLOUD MICROPHYSICS

CLOUD MORPHOLOGY

RADIATION STUDIES

CLOUD LOCATION STATISTICS, INCLUDING OVERLAP

SUNSHINE

UNDERWORLD

PRIMARY GOAL:

DETECT ALL HYDROMETEORS IN A VERTICAL COLUMN

SECONDARY GOAL:

GIVEN A DETECTION, THEN ATTEMPT TO PRODUCE ACCURATE

CLOUD BASE HEIGHTS

CLOUD TOP HEIGHTS

RADAR REFLECTIVITIES

RADAR DOPPLER VELOCITIES

RADAR DOPPLER WIDTHS

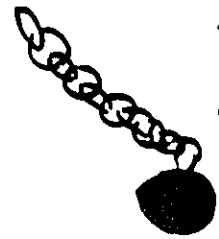

RADAR-BASED CLOUD DETECTION

FIG. 1

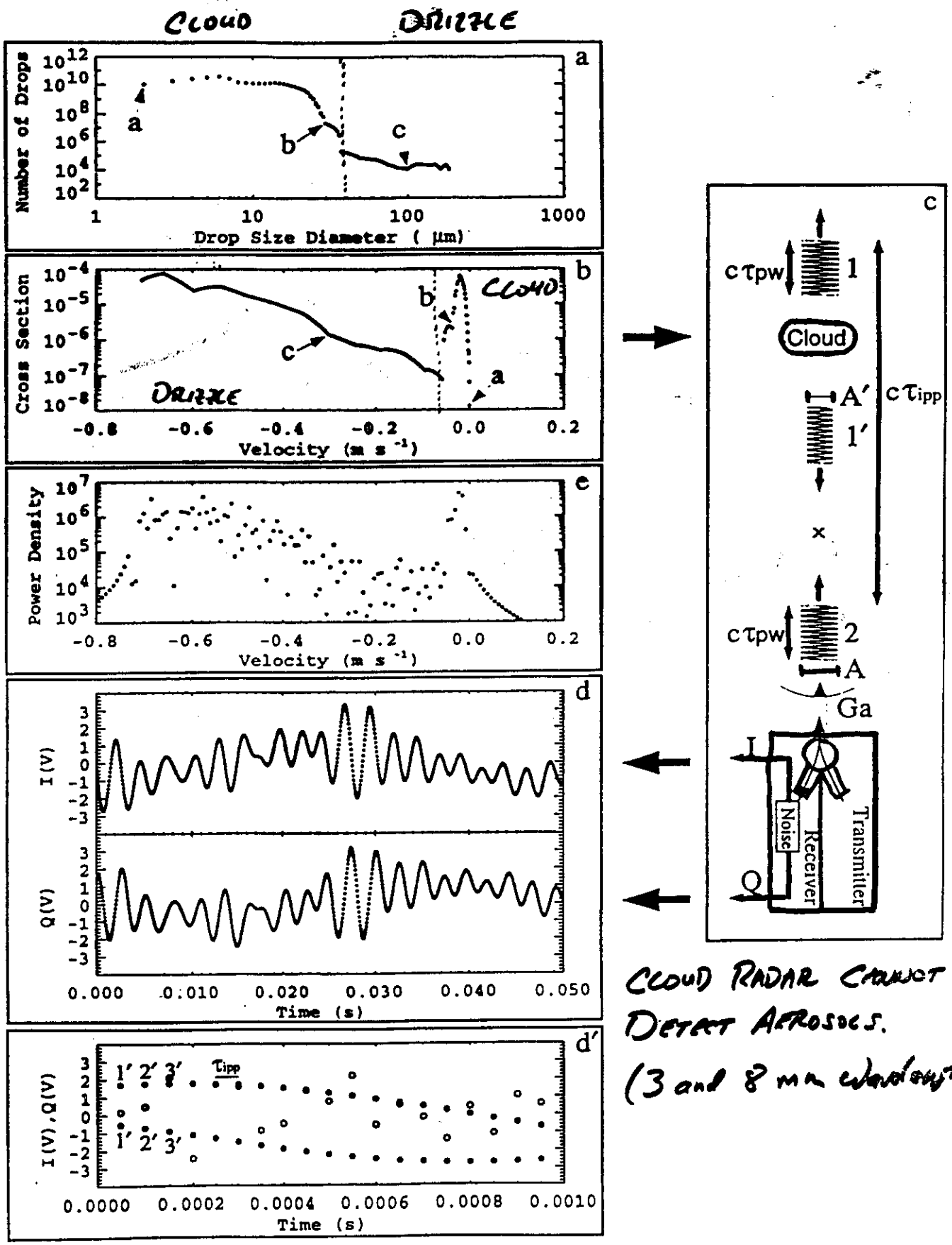

CLOUD RADAR CANNOT DETECT AEROSOLS.

(3 and 8 mm wavelength)

The goal is to detect clouds of all sorts. Therefore, the radar wavelength should be chosen to maximize the backscatter from the cloud resolution volume while minimizing the attenuation of the beam from the radar to the resolution volume and then back to the radar. Now

$$\eta(r) = \int \sigma_b(D)\, N(D,r)\, dD$$

For drops small compared to the wavelength of the radar, we have:

$$\sigma_b = \frac{\pi^5 |K_m|^2 D^6}{\lambda^4} \quad (\lambda > D)$$

Operational frequencies and wavelengths of various meteorological radars are:

50 MHz	6 m	(Wind Profiler)
405 MHz	74 cm	(Wind Profiler)
915 MHz	33 cm	(Wind/Precipitation Profiler)
3.0 GHz	10 cm	(Precipitation Radar)
35.0 GHz	8 mm	(Cloud Radar)
94.0 GHz	3 mm	(Cloud Radar)

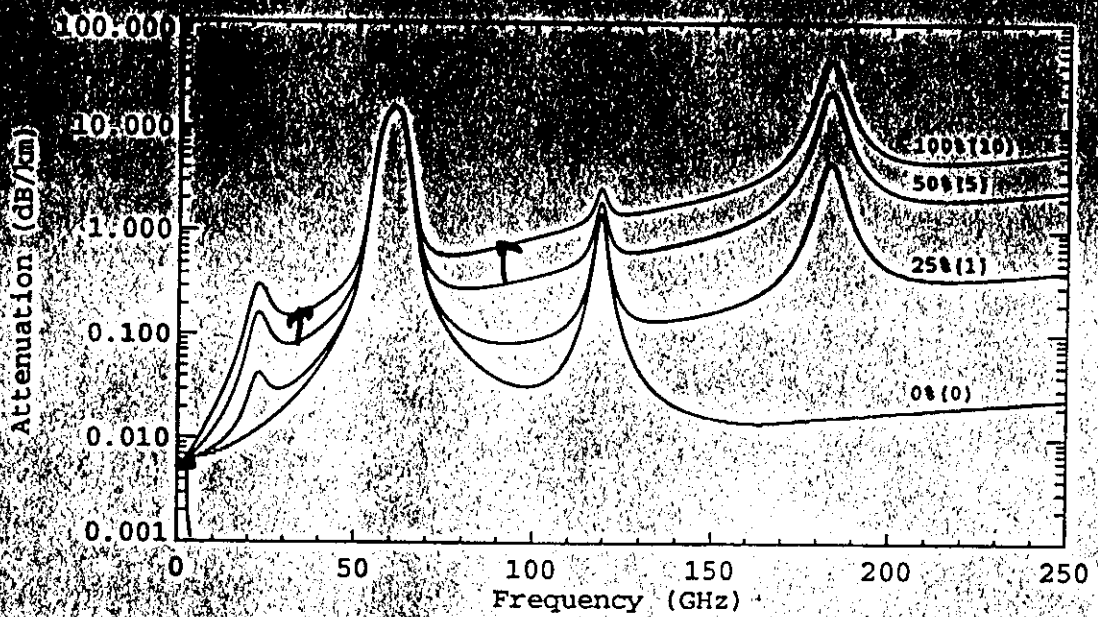
100.000
10.000
1.000
0.100
0.010
0.001
Attenuation (dB/km)
100%(10)
50%(5)
25%(1)
0%(0)
0
50
100
150
200
250
Frequency (GHz)

B F10

Recall that

$$\eta(r) = \int \sigma_b(D)\, N(D,r)\, dD$$

and

$$\sigma_b = \frac{\pi^5 |K_m|^2 D^6}{\lambda^4} \quad (\lambda > D),$$

Therefore,

$$\eta(r) = \frac{\pi^5 |K_m|^2}{\lambda^4} \frac{\int D^6 N(D,r)\, dD}{Z \text{ (Reflectivity Factor)}}$$

In units of dBZ we have $Z(\text{dBZ}) = 10 \log_{10}(Z)$.

B 5/5

F1

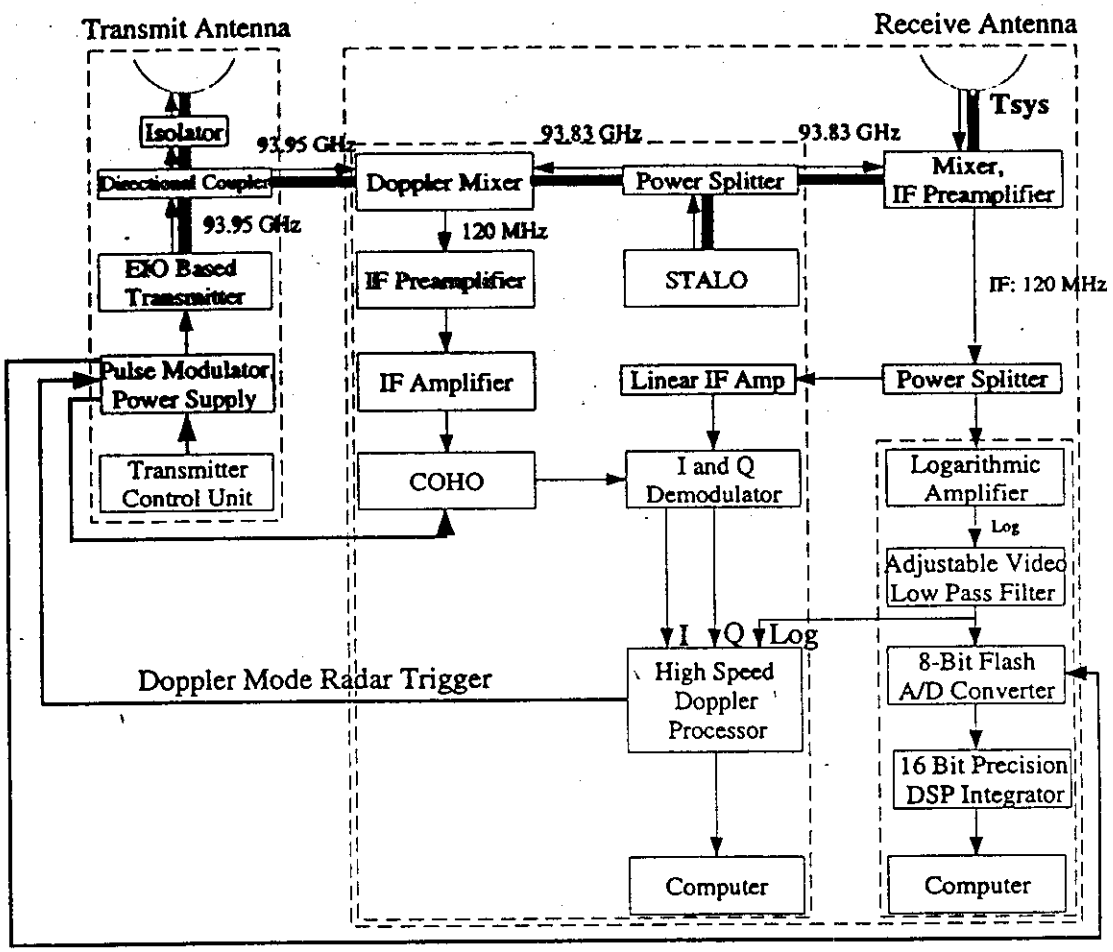
Transmit Antenna
Receive Antenna
Isolator
93.95 GHz
93.83 GHz
93.83 GHz
Tsys
Directional Coupler
Doppler Mixer
Power Splitter
Mixer, IF Preamplifier
93.95 GHz
120 MHz
EIO Based Transmitter
IF Preamplifier
STALO
IF: 120 MHz
Pulse Modulator Power Supply
IF Amplifier
Linear IF Amp
Power Splitter
Transmitter Control Unit
COHO
I and Q Demodulator
Logarithmic Amplifier
Log
Adjustable Video Low Pass Filter
I
Q
Log
Doppler Mode Radar Trigger
High Speed Doppler Processor
8-Bit Flash A/D Converter
16 Bit Precision DSP Integrator
Computer
Computer

F2

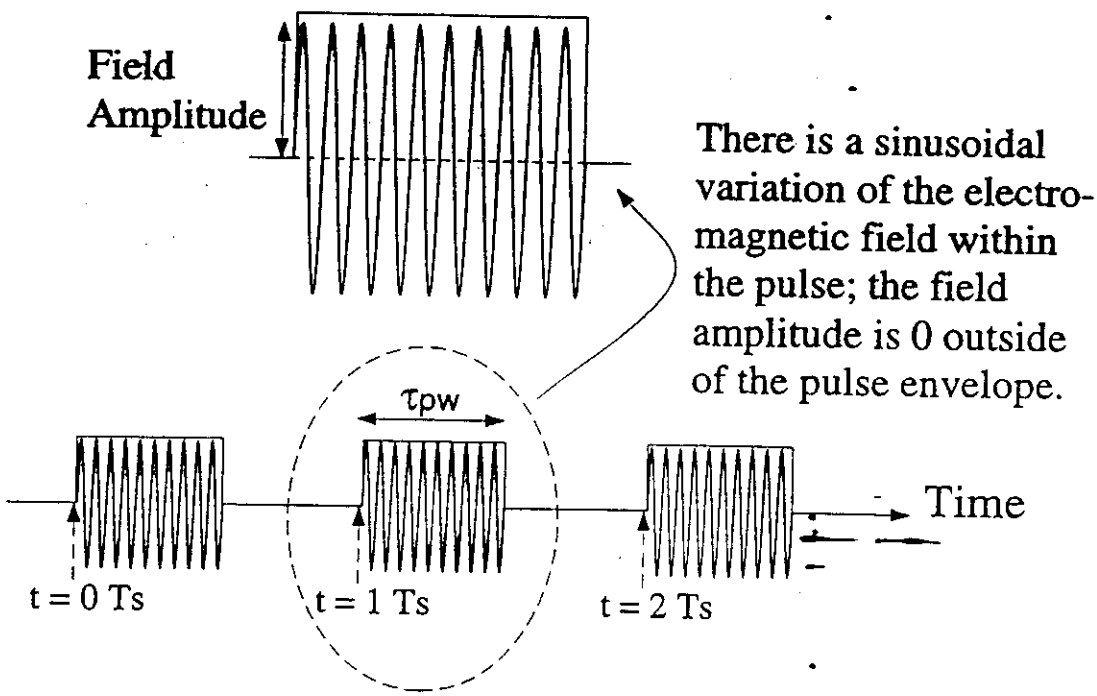
Field
Amplitude
There is a sinusoidal variation of the electro-magnetic field within the pulse; the field amplitude is 0 outside of the pulse envelope.
τpw
Time
t = 0 Ts
t = 1 Ts
t = 2 Ts

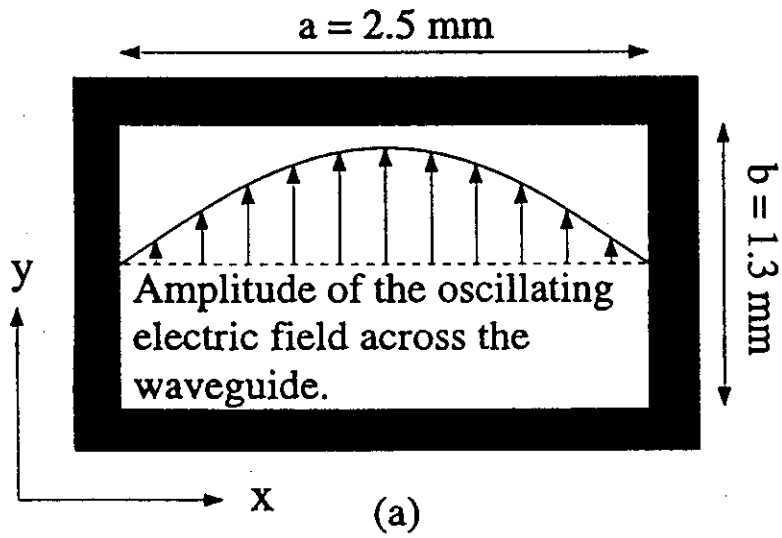
a = 2.5 mm
b = 1.3 mm
Amplitude of the oscillating electric field across the waveguide.
y
x

(a)

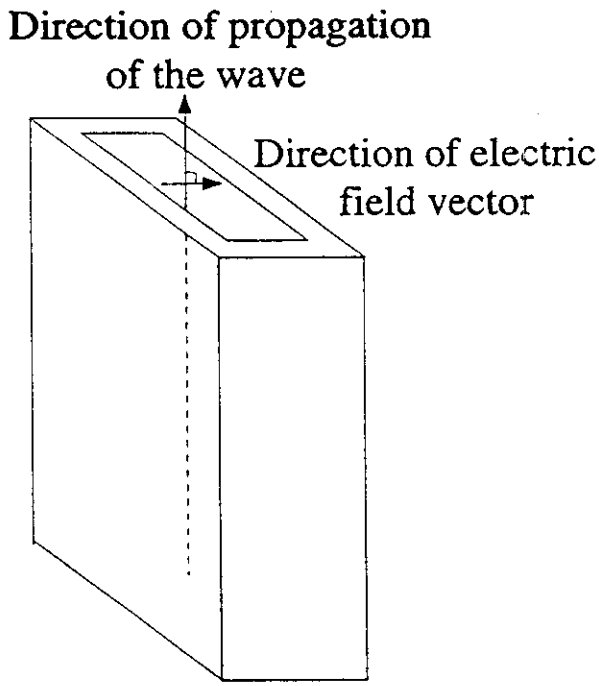
Direction of propagation of the wave
Direction of electric field vector

(b)

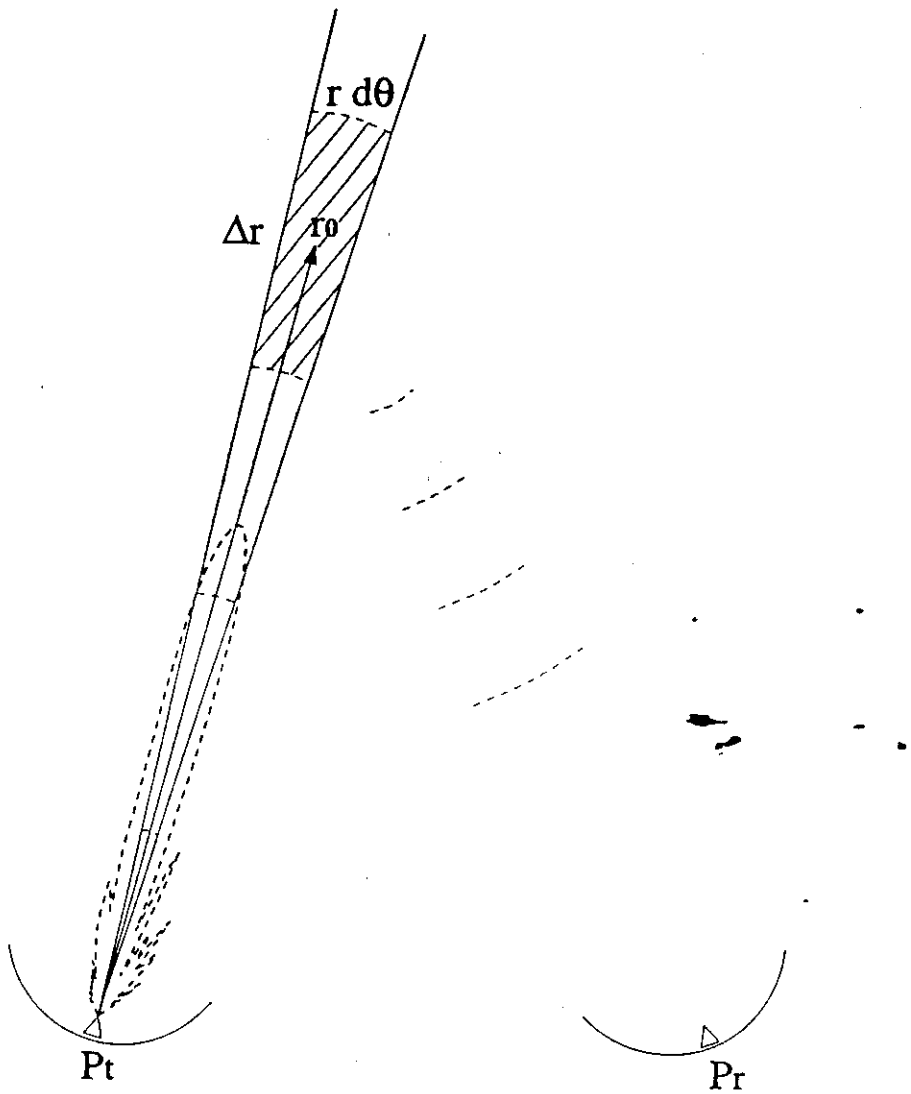

F5

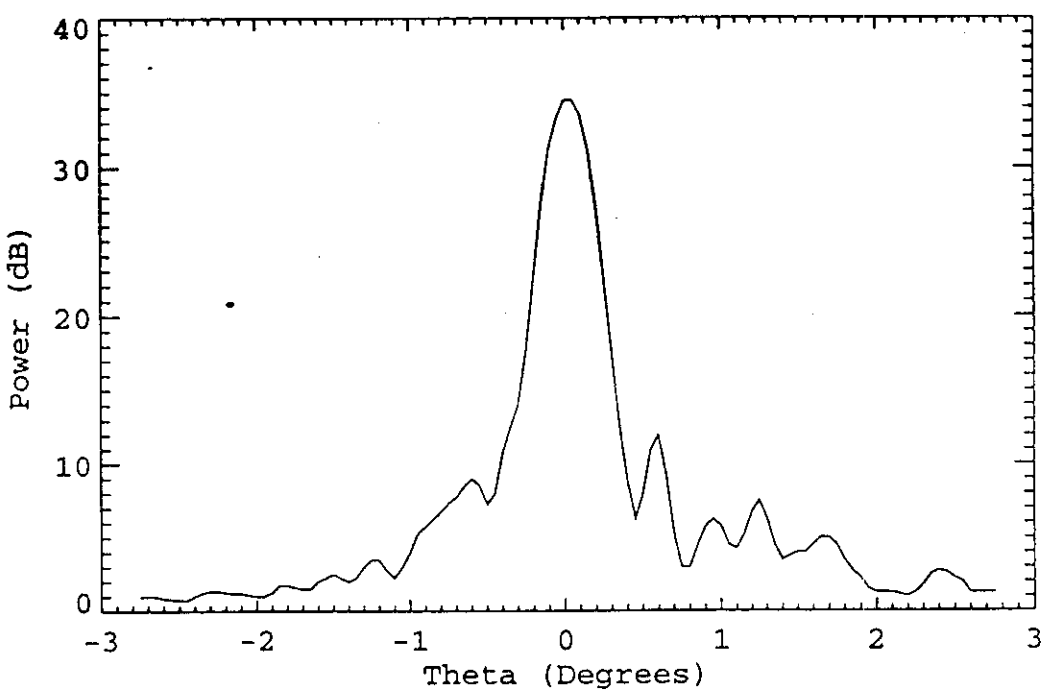

F6

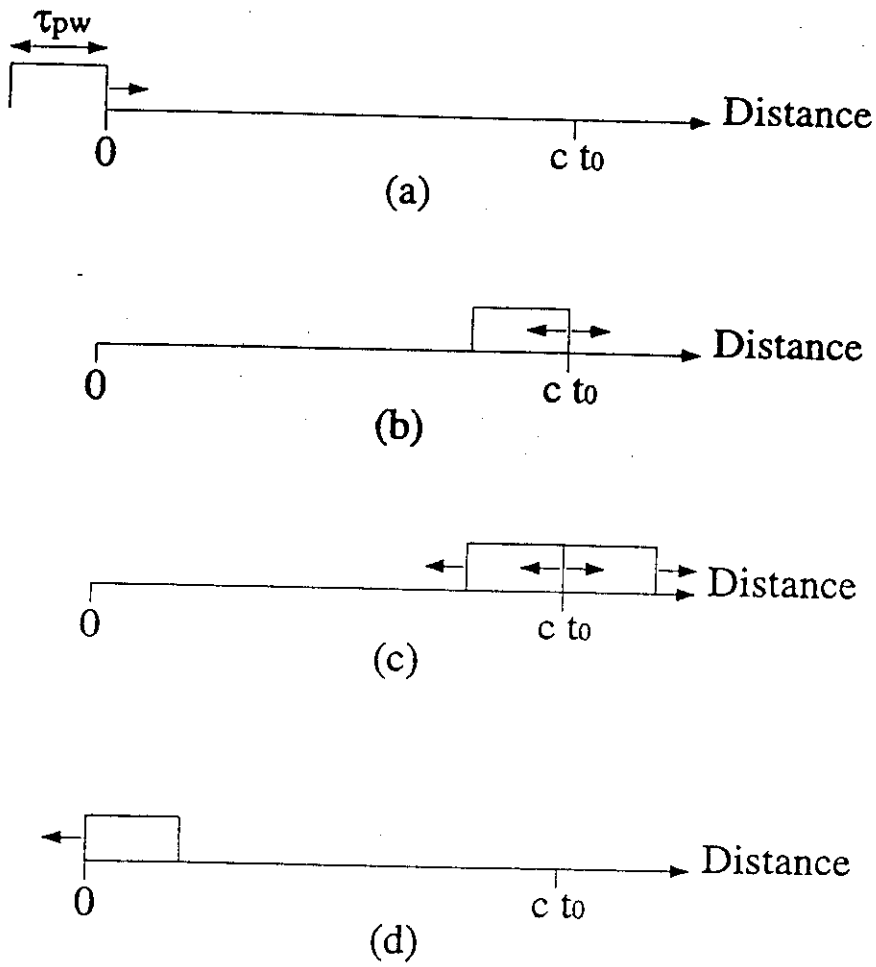
τpw
Distance
0
c to
(a)
Distance
0
c to
(b)
Distance
0
c to
(c)
Distance
0
c to
(d)

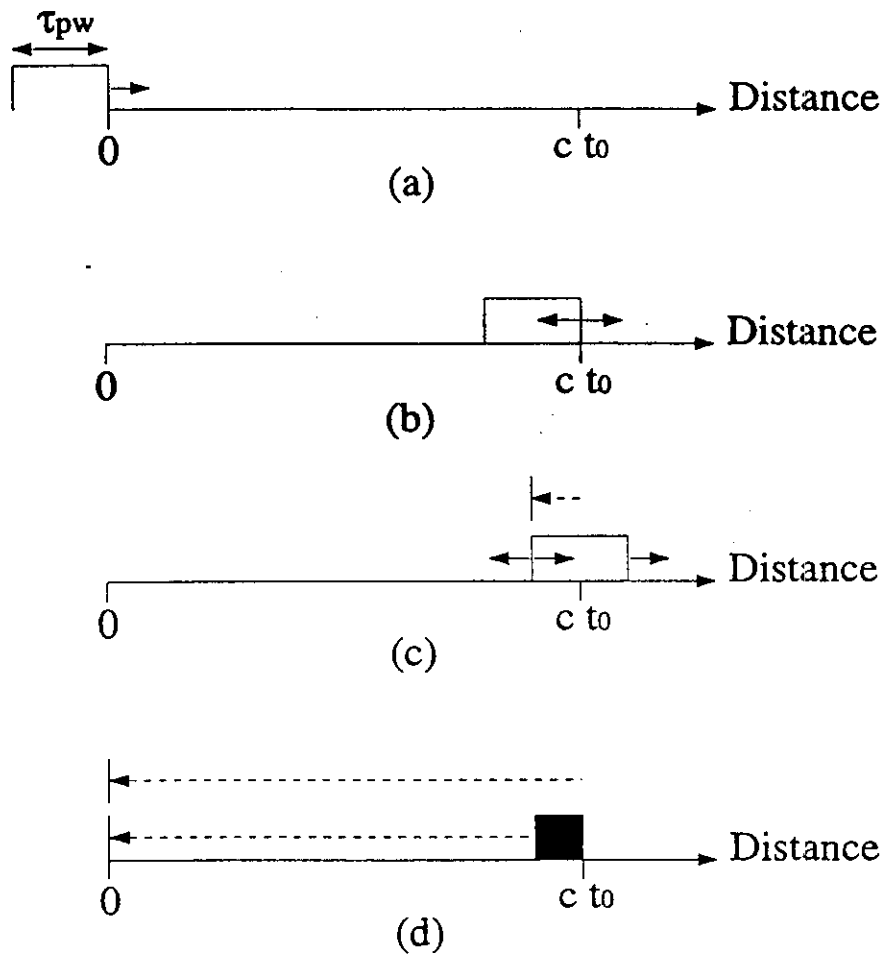
τpw
Distance
0
c to
(a)
Distance
0
c to
(b)
Distance
0
c to
(c)
Distance
0
c to
(d)

F8

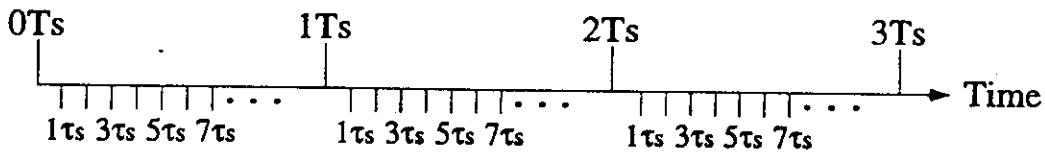
0Ts
1Ts
2Ts
3Ts
Time
1τs 3τs 5τs 7τs
1τs 3τs 5τs 7τs
1τs 3τs 5τs 7τs

F9

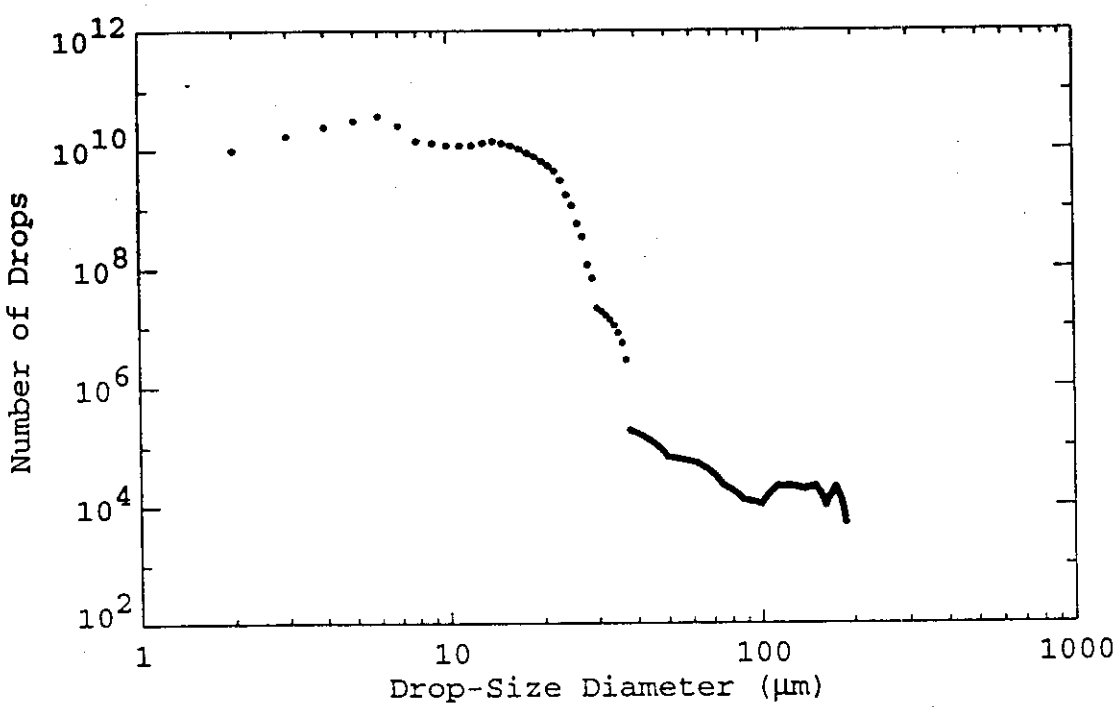
10^{12}
10^{10}
10^{8}
10^{6}
10^{4}
10^{2}
Number of Drops
1
10
100
1000
Drop-Size Diameter (μm)

F10

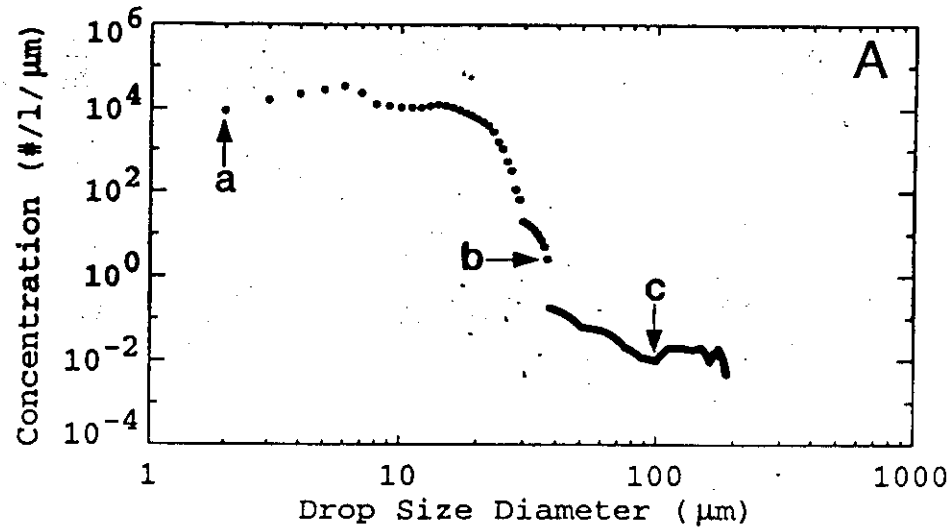
A
Concentration (#/l/µm)
10^6
10^4
10^2
10^0
10^{-2}
10^{-4}
a
b
c
1
10
100
1000
Drop Size Diameter (µm)

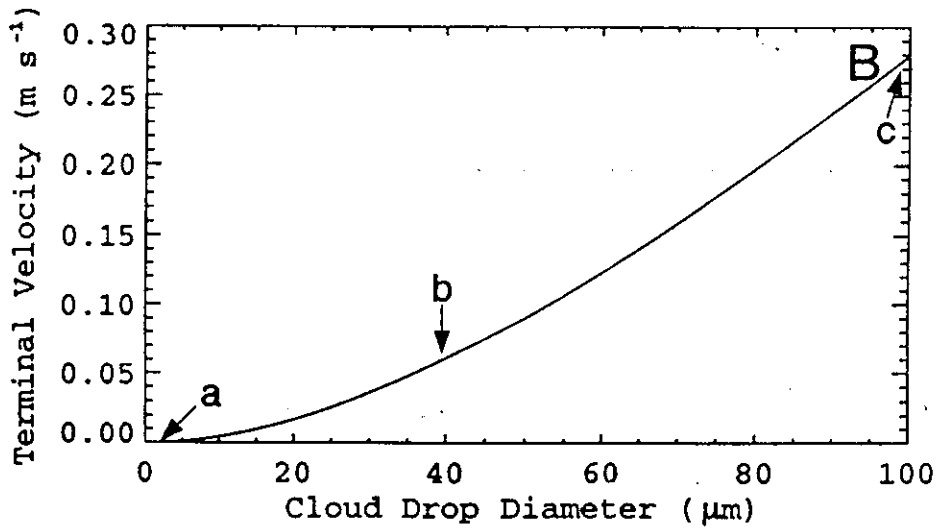
B
Terminal Velocity (m s^{-1})
0.30
0.25
0.20
0.15
0.10
0.05
0.00
a
b
c
0
20
40
60
80
100
Cloud Drop Diameter (µm)

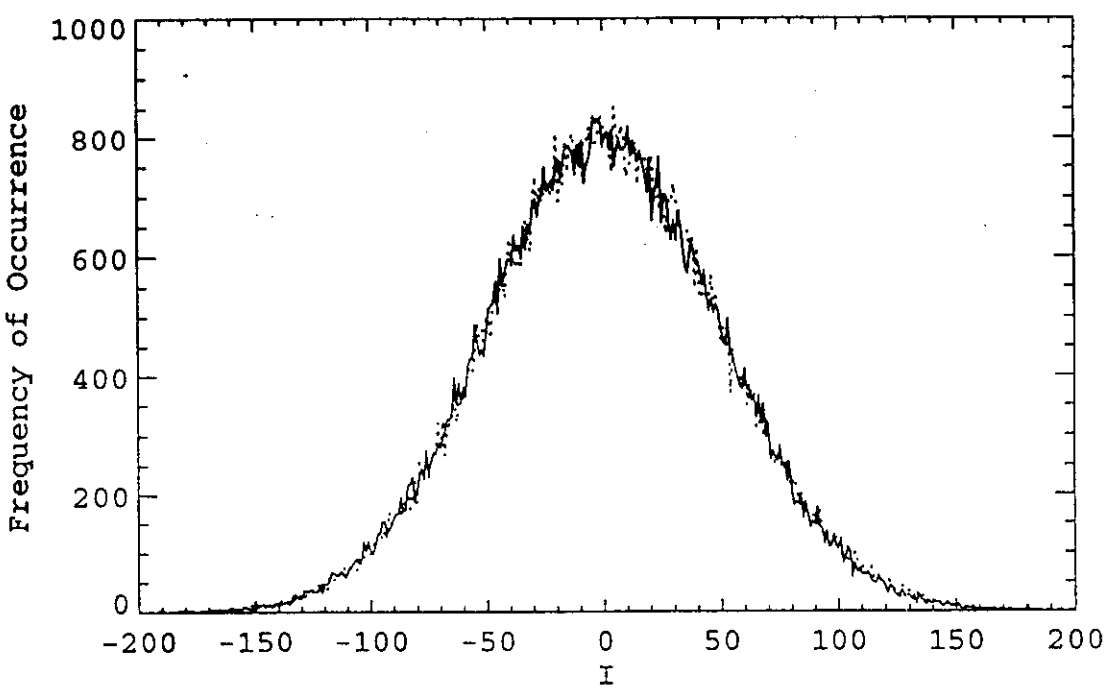
Frequency of Occurrence
1000
800
600
400
200
0
-200
-150
-100
-50
0
50
100
150
200
I

FIG

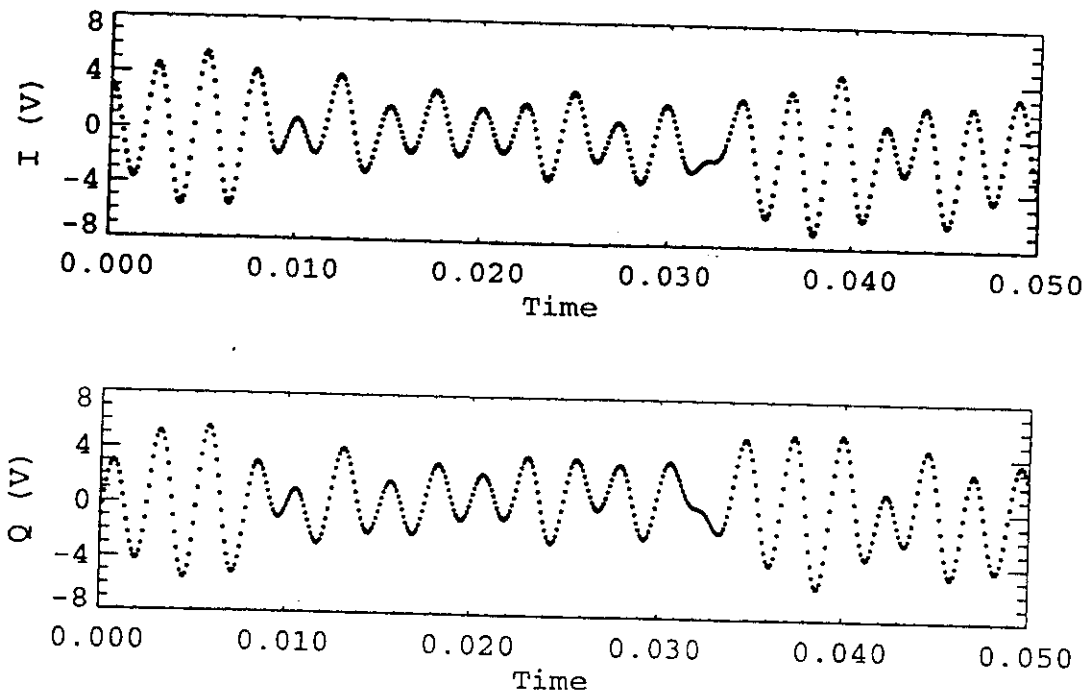
8
4
0
-4
-8
I (V)
0.000
0.010
0.020
0.030
0.040
0.050
Time
8
4
0
-4
-8
Q (V)
0.000
0.010
0.020
0.030
0.040
0.050
Time

F12

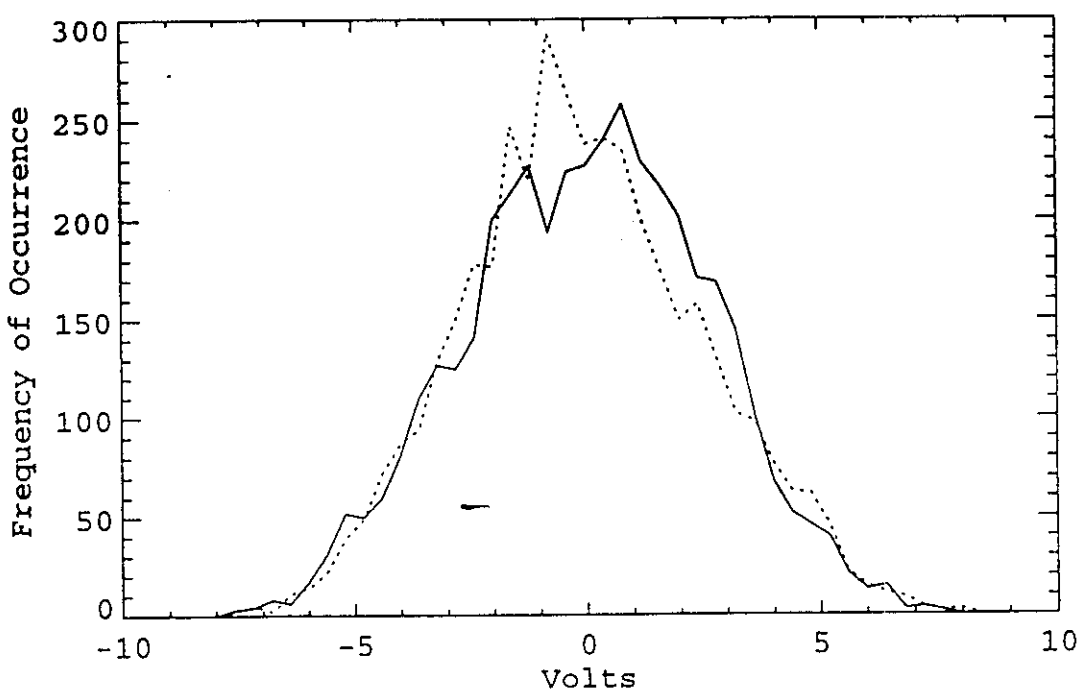
Frequency of Occurrence
300
250
200
150
100
50
0
-10
-5
0
5
10
Volts

F13

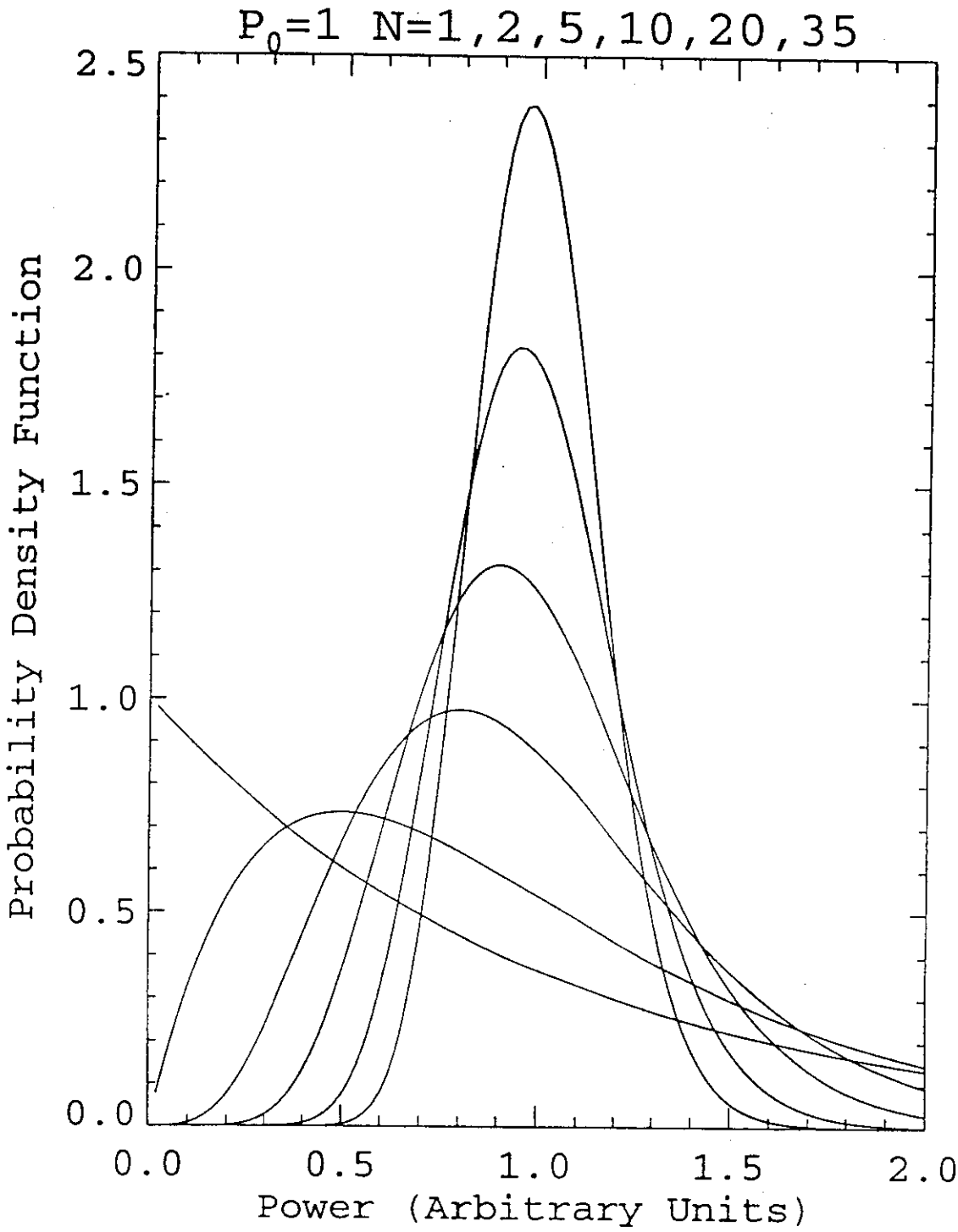
P_0=1 N=1,2,5,10,20,35
Probability Density Function
2.5
2.0
1.5
1.0
0.5
0.0
0.0
0.5
1.0
1.5
2.0
Power (Arbitrary Units)

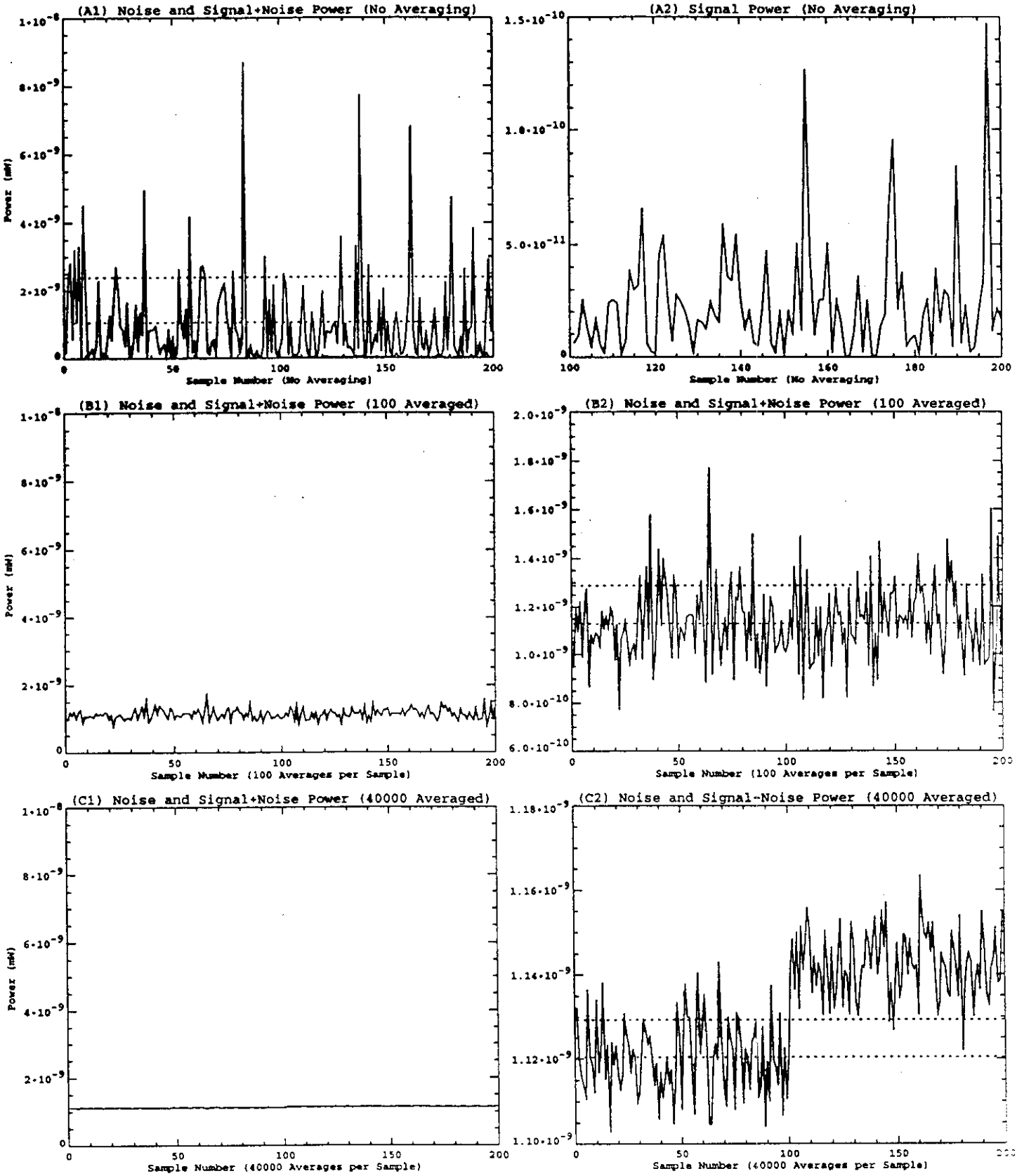
(A1) Noise and Signal+Noise Power (No Averaging)
Power (mW)
Sample Number (No Averaging)
(A2) Signal Power (No Averaging)
Sample Number (No Averaging)
(B1) Noise and Signal+Noise Power (100 Averaged)
Power (mW)
Sample Number (100 Averages per Sample)
(B2) Noise and Signal+Noise Power (100 Averaged)
Sample Number (100 Averages per Sample)
(C1) Noise and Signal+Noise Power (40000 Averaged)
Power (mW)
Sample Number (40000 Averages per Sample)
(C2) Noise and Signal-Noise Power (40000 Averaged)
Sample Number (40000 Averages per Sample)

F16

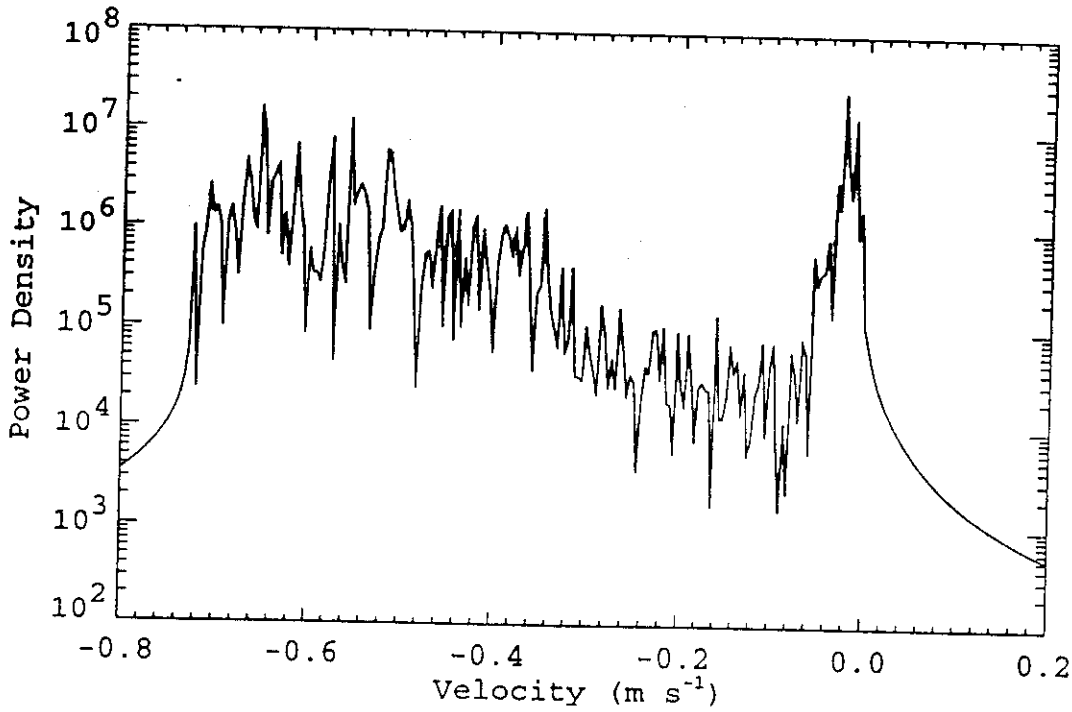
Power Density
10^8
10^7
10^6
10^5
10^4
10^3
10^2
-0.8
-0.6
-0.4
-0.2
0.0
0.2
Velocity (m s^{-1})

F17

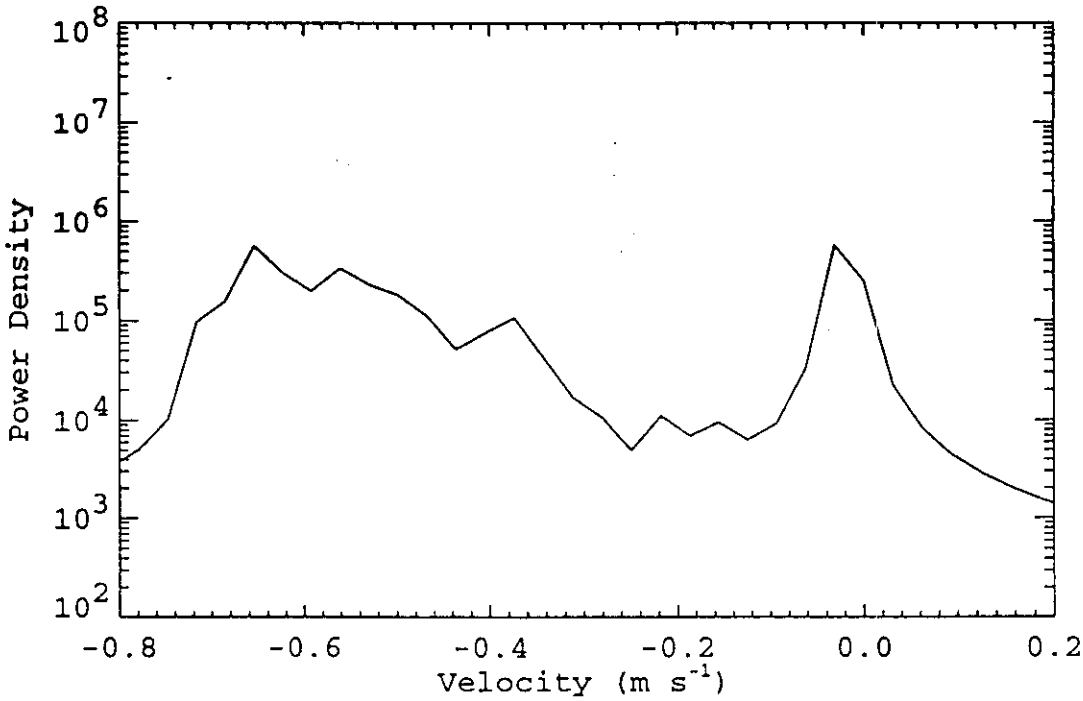
Power Density
10^8
10^7
10^6
10^5
10^4
10^3
10^2
-0.8
-0.6
-0.4
-0.2
0.0
0.2
Velocity (m s^{-1})

F18

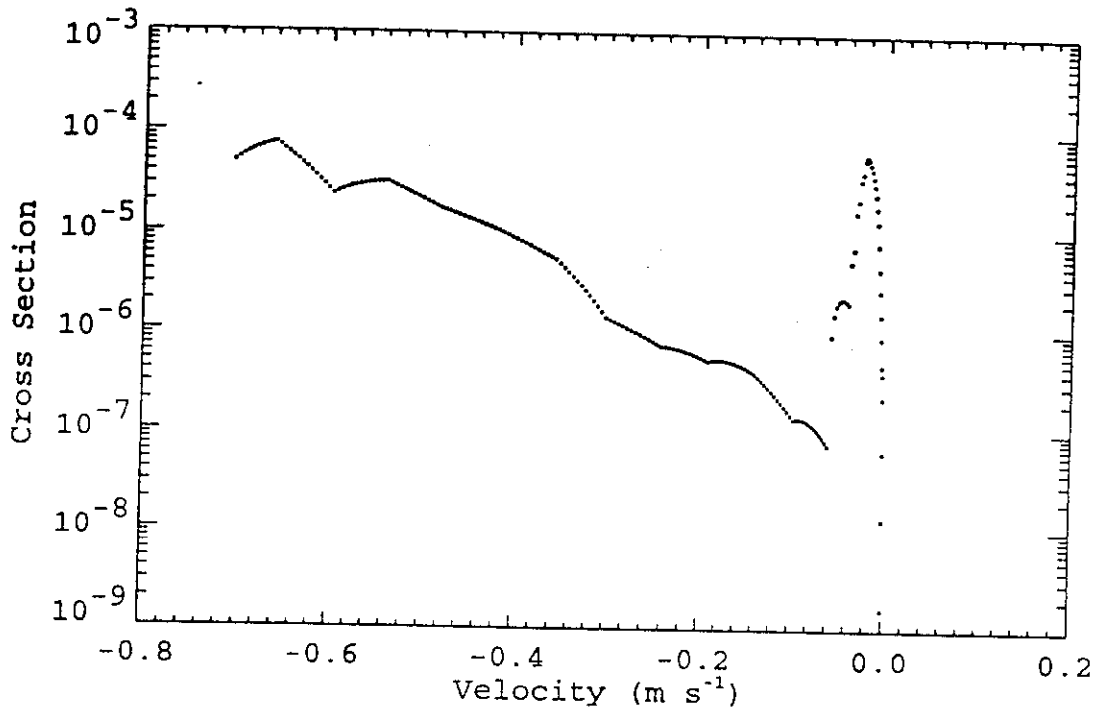
Cross Section
10^{-3}
10^{-4}
10^{-5}
10^{-6}
10^{-7}
10^{-8}
10^{-9}
-0.8
-0.6
-0.4
-0.2
0.0
0.2
Velocity (m s^{-1})

F19

F4

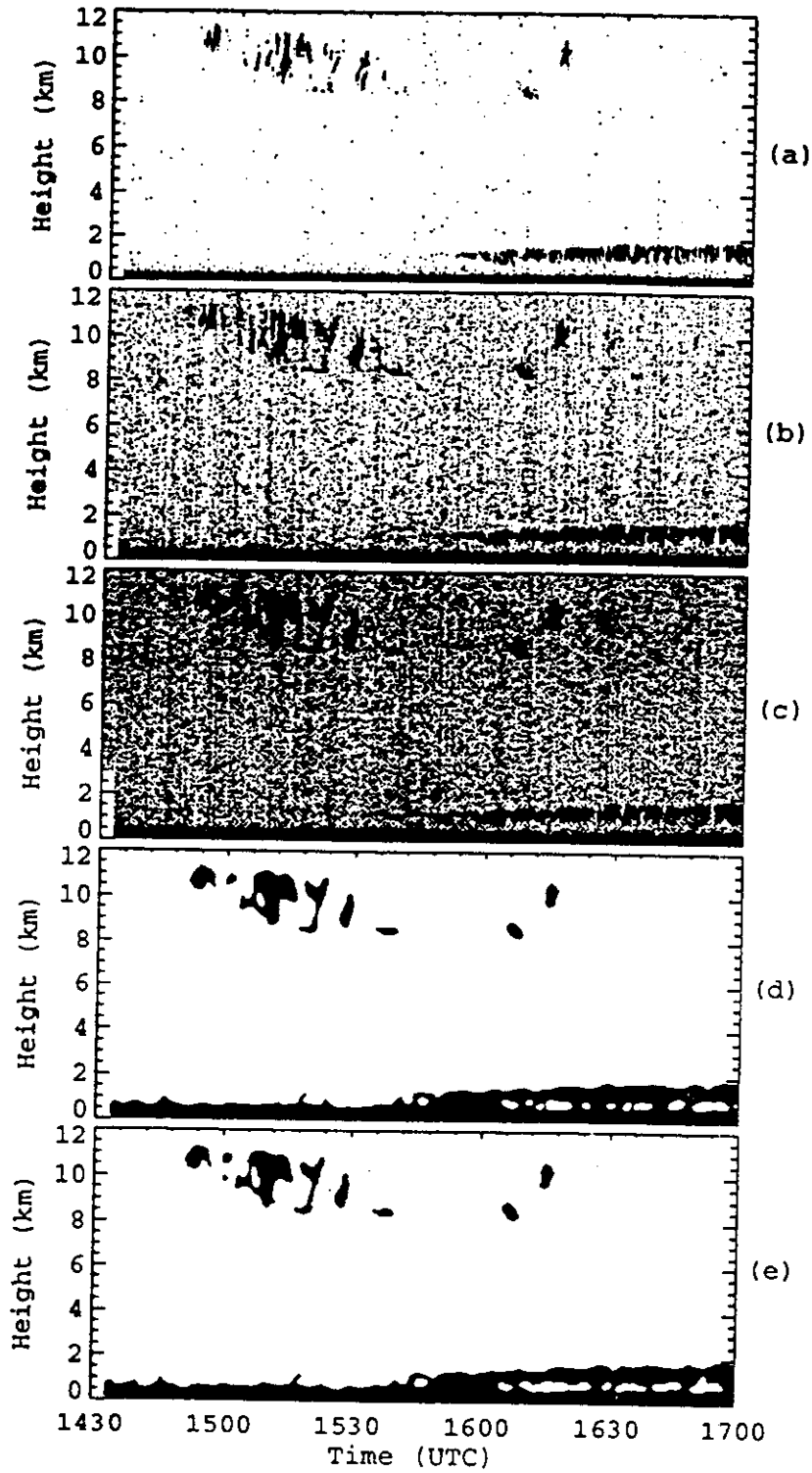
Height (km)
12
10
8
6
4
2
0
(a)
(b)
(c)
(d)
(e)
1430
1500
1530
1600
1630
1700
Time (UTC)

B F13

Table 1.

Radar Parameter Relationships

$R_{min} = R_{deadtime} + N_{bits}\Delta R$

$R_{max} = R_{deadtime} + (N_{vol} - 1)R_{space}$

$R_u = (c\tau_{ipp})/2$

$\Delta R = (c\tau_{pw})/2$

$V_u = \lambda/(4\tau_{ipp}N_{coh})$

$\Delta V_u = (2V_u)/N_{fft}$

$T_s \propto N_{vol}, N_{fft}, N_{spec}$, 1/Processor Speed

Radar Sensitivity $\propto \tau_{pw}, N_{bits}$

Noise Fluctuations $\propto 1/N_{coh}, 1/\sqrt{N_{spec}}$

ENHANCE SENSITIVITY:

SEND OUT BIG PULSES (T_{PW} LARGE)

DO LOTS OF PULSE CODING (N_{BITS} LARGE)

REDUCE NOISE:

DO LOTS OF COHERENT AVERAGING (N_{COH} LARGE)

DO LOTS OF INCOHERENT AVERAGING (N_{SPEC} LARGE)

EACH CHOICE ABOVE COMES WITH

TRADE OFFS!

Table 3.

Mode	SGP				TWP				NSA			
	4	3	2	1	4	3	2	1	4	3	2	1
Number Range Volumes (N_{vol})	167	167	167	110	226	226	226	134	221	149	149	135
Range Volume Spacing (R_{space}, m)	90	90	90	45	90	90	90	45	45	90	90	45
Pulse Width (τ_{pw}, ns)	600	600	600	300	600	600	600	300	300	600	600	300
Interpulse Period (τ_{ipp}, μs)	106	106	126	68	142	142	160	90	90	96	115	68
Number Coded Bits (N_{bits})	0	0	32	8	0	0	32	8	0	0	32	8
Number Coherent Averages (N_{coh})	1	6	6	10	1	5	4	8	2	7	6	10
Number Spectra Averaged (N_{spec})	29	60	21	64	20	44	16	50	20	70	23	50
Number FFT Points (N_{fft})	128	64	64	64	128	64	64	64	128	64	64	64
Minimum Range (R_{min}, m)	105	105	2985	465	105	105	2985	465	105	105	2985	465
Maximum Range (R_{max}, m)	15045	15045	15045	5010	20355	20355	20355	6090	10005	13425	13425	6135
Unambiguous Range (R_u, m)	15900	15900	18900	10200	21300	21300	24000	13500	13500	14400	17250	10200
Range Volume Resolution (ΔR, m)	90	90	90	45	90	90	90	45	45	90	90	45
Unambiguous Velocity (V_u, m s^{-1})	20.28	3.38	2.84	3.16	15.14	3.03	3.36	2.99	11.94	3.20	3.12	3.16
Velocity Resolution (ΔV_u, m s^{-1})	0.32	0.11	0.09	0.10	0.24	0.09	0.11	0.09	0.19	0.10	0.10	0.10
Time Resolution (T_s, s)	9.0	8.5	8.7	9.0	9.0	8.6	9.0	8.5	9.0	9.0	9.0	9.0
Minimum Detected Signal (dBm)	-132	-135	-133	-135	-131	-134	-131	-134	-131	-136	-133	-134
Estimated Sensitivity (5 km, dBZe)	-38	-42	-54	-47	-32	-35	-48	-41	-32	-40	-51	-44

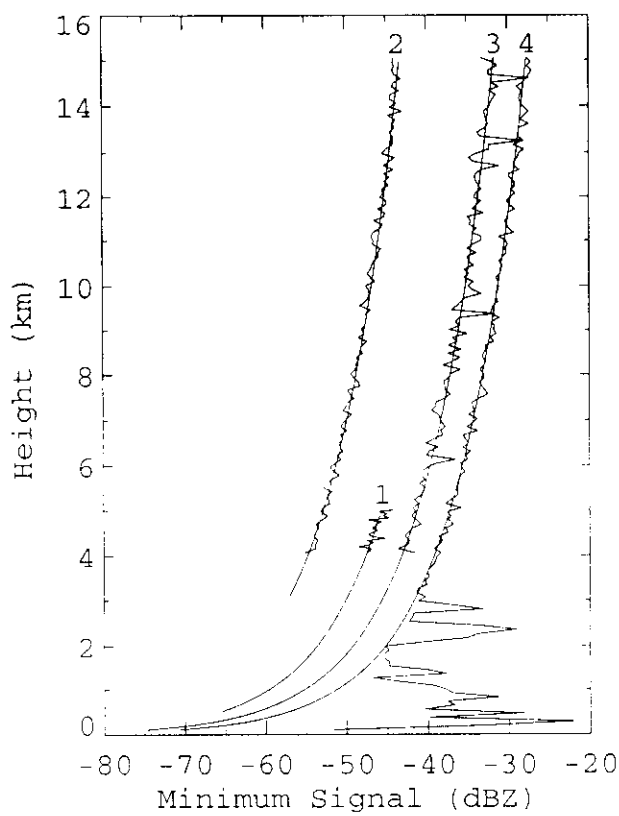
16
14
12
10
8
6
4
2
0
Height (km)
1
2
3
4
-80
-70
-60
-50
-40
-30
-20
Minimum Signal (dBZ)

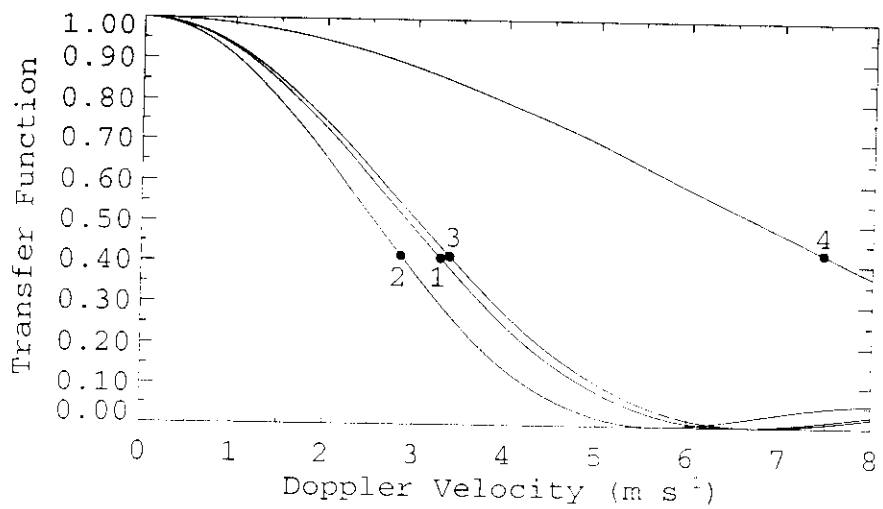
Transfer Function
1.00
0.90
0.80
0.70
0.60
0.50
0.40
0.30
0.20
0.10
0.00
0
1
2
3
4
5
6
7
8
Doppler Velocity (m s⁻¹)
1
2
3
4